Inlet Swirl Distortion Effects on the Generation and Propagation of Fan Rotor Shock Noise

by

Jeff Defoe

Submitted to the Department of Aeronautics and Astronautics
in partial fulfillment of the requirements for the degree of

Doctor of Philosophy

at the

MASSACHUSETTS INSTITUTE OF TECHNOLOGY

September 2011

Author .....
Department of Aeronautics and Astronautics
August 10, 2011

Certified by .....
Zoltán S. Spakovszky
Associate Professor of Aeronautics and Astronautics
Thesis Supervisor

Certified by .....
Edward M. Greitzer
Professor of Aeronautics and Astronautics
Thesis Committee

Certified by .....
David L. Darmofal
Professor of Aeronautics and Astronautics
Thesis Committee

Accepted by .....
Eytan H. Modiano
Professor of Aeronautics and Astronautics
Chair, Graduate Program Committee

Inlet Swirl Distortion Effects on the Generation and Propagation of Fan Rotor Shock Noise

by

Jeff Defoe

Submitted to the Department of Aeronautics and Astronautics
on August 10, 2011, in partial fulfillment of the
requirements for the degree of
Doctor of Philosophy

Abstract

A body-force-based fan model for the prediction of multiple-pure-tone noise generation is developed in this thesis. The model eliminates the need for a full-wheel, three-dimensional unsteady RANS simulation of the fan blade row, allowing Euler calculations to be used to capture the phenomena of interest. The Euler calculations reduce numerical wave dissipation and enable the simultaneous computation of source noise generation and propagation through the engine inlet to the far-field in non-uniform flow. The generated shock Mach numbers are in good agreement with experimental results, with the peak values predicted within 6%. An assessment of the far-field acoustics against experimental data showed agreement of 8 dB on average for the blade-passing tone.

In a first-of-its-kind comparison, noise generation and propagation are computed for a fan installed in a conventional inlet and in a boundary-layer-ingesting serpentine inlet for a free-stream Mach number of 0.1. The key effect of boundary layer ingestion is the creation of streamwise vorticity which is ingested into the inlet, resulting in co- and counter-rotating streamwise vortices in the inlet. The fan sound power level increases by 38 dB due to this distortion, while the vortex whose circulation is in the same direction as the fan rotation enhances the sound power attenuation within the inlet duct such that the far-field overall sound pressure levels are increased by only 7 dB on average. The far-field spectra are altered in the following manner due to inlet distortion: (1) tones at up to 3 times the blade-passing frequency are amplified; and (2) tones above one-half of the blade-passing frequency are attenuated and appear to be cut-off.

To quantify the effects of serpentine inlet duct geometry on the generation and propagation of multiple-pure-tone noise, a parametric study of inlets is conducted. The conclusions are that (1) the ingestion of streamwise vorticity alters multiple-pure-tone noise more than changes in inlet area ratio or offset ratio do; and (2) changes in the far-field spectra relative to the conventional inlet results are only weakly affected by the duct geometry changes investigated and are instead predominantly caused by flow non-uniformities. A response-surface correlation for the effects of inlet geometry on far-field noise is also developed.

Thesis Supervisor: Zoltán S. Spakovszky
Title: Associate Professor of Aeronautics and Astronautics

Acknowledgements

There are many to whom I owe a debt of gratitude, and without each of these people my success at MIT would not have been possible. The following individuals and organizations are particularly deserving of acknowledgement.

I would like to thank all members of my thesis committee for both their time and invaluable feedback. First I would like to thank my thesis supervisor, Professor Zoltán Spakovszky, for the opportunity to become a member of the MIT community and for helping me mature academically with his healthy criticism and unwavering expectations of excellence. Professor Greitzer provided helpful perspective on the research and his feedback was always appreciated. Professor Darmofal was a source of clear advice and his contributions to enhancing the clarity of my thesis were invaluable.

The personnel of the Gas Turbine Laboratory defined my experience at MIT. Their camaraderie and input were great motivators for tackling the challenges of this work. I am especially grateful to Sho Sato, Dorian Colas, Andreas Peters, Jon Everitt, and many others.

The contributions of Alex Narkaj to this work must be mentioned. He provided invaluable assistance in the development of the body-force-based fan noise model described in this work by performing the Fine-Turbo computations used to determine the details of the model for the specific fan studied.

This work was funded by the NASA Langley Research Center (Dr. R. Thomas as contract monitor). I am also indebted to the advice and feedback provided by Dr. John Adamczyk and Professor Nick Cumpsty throughout this work.

To my family, I would like to express the deepest gratitude for shaping me into the person I am today with great love and guidance.

Most important of all, I need to thank my wife Stephanie for two important reasons. First, it was her encouragement and willingness to have a "life adventure" with me which led to my applying to MIT. Just as importantly, she contributed to this accomplishment each and every day with her unconditional love. Steph, I truly could not have done this without you. Thank you for being my teammate in life.

Contents

List of Figures

List of Tables

Nomenclature

Symbols

a speed of sound

A area, surface

AR duct area ratio, $\frac{A_{AIP}}{A_{throat}}$

b Burgers vortex radius

e total internal energy

B number of blades in blade row

c blade chord

D diameter

E disturbance internal energy

f frequency

F body force per unit mass

h staggered spacing in blade row

H stagnation enthalpy

I sound intensity

k wavenumber

K body force coefficient

j imaginary number, $\sqrt{-1}$

J Bessel function of the first kind

l linear momentum per unit mass

L axial length of serpentine inlet

m circumferential order/mode

M Mach number

n radial order/mode

n^* Fourier series components representing sawtooth wave

N unit sawtooth function

OR duct offset ratio, $\frac{\delta}{D_{AIP}}$

p static pressure

P viscous stress tensor

q heat flux

r radial coordinate

R radial part of transverse eigenfunction of annular duct

Re Reynolds number

s entropy

S body force perturbation shaping function

t time

T static temperature

u velocity

w relative velocity

W disturbance energy flux

x axial coordinate

Y coefficient of numerical dissipation correction function

Z exponent of numerical dissipation correction function

α local blade camber angle

β reduced frequency

γ ratio of specific heats

γ_{yu}^2 squared coherence of transfer function

Γ circulation

δ duct vertical offset

Δy spacing between counter-rotating vortex pair

ϵ error in fit of Bessel functions to radial pressure field

ζ solution of two-dimensional convected wave equation

η index of Fourier series

Ψ transverse eigenfunction of annular duct

θ circumferential coordinate

Θ azimuthal part of transverse eigenfunction of annular duct

Θ_{em} emission angle

κ solution of equation 6.3

λ wavelength

Λ transverse eigenfunction for two-dimensional convected wave equation

ν body force scaling parameter

ν_{turb} turbulent kinematic viscosity

ξ incidence angle

Ξ source term in equation 2.4

π static pressure ratio across shock

ϖ_p sound power

ρ density

σ solidity

τ period

υ length scale for circulation of vortices at duct inlet with BLI

Υ wave propagation distance

Φ cross/auto-spectra

χ blade stagger angle

ω angular frequency

Ω fan rotational speed

Subscripts

b blade row

i,j vector/matrix components (tensor notation)

t stagnation quantity

∞ free-stream condition

Superscripts

$'$ fluctuating portion of quantity (difference between instantaneous value and time-average)

M mass-averaged quantity

Abbreviations

BLI boundary layer ingestion/ingesting

AIP aerodynamic interface plane

DC(60) distortion coefficient (worst 60 degrees)

RANS Reynolds-averaged Navier-Stokes

MPT multiple-pure-tone

PPW points per wavelength

FW-H Ffowcs-Williams and Hawkings

Chapter 1

Introduction

1.1 Introduction

The use of boundary layer ingestion has been identified [1–7] as one potential means to reduce fuel consumption on next-generation aircraft such as the Silent Aircraft Initiative's SAX-40, shown in Figure 1-1. This can improve propulsive efficiency by reducing the kinetic energy surplus in the fan exhaust. Many propulsion systems designed for boundary layer ingestion are embedded into the airframe and employ serpentine inlet ducts. Currently there is limited quantitative characterization of how boundary layer ingestion and serpentine inlets affect fan noise. At take-off flight speeds, an important fan noise source is multiple-pure-tone (MPT)—also known as "buzz-saw"—noise. Multiple-pure-tone noise is of concern in the community near airports [8–12] as it can be the dominant engine noise source in the forward arc during take-off and cut-back [8].

For fans with regions of incoming supersonic relative flow, shocks are generated at the blade leading edges if the blade passages are unstarted. Small changes in blade stagger angle (up to $\pm 0.2^{\circ}$ [10]) result in rotor-locked shocks with varying strengths and propagation directions as illustrated in Figure 1-2. Such a system of shocks will coalesce into a pressure field with once-per-revolution periodicity as it propagates upstream in the inlet duct. MPT noise is characterized by this series of tones at the shaft frequency and its higher harmonics. Even with identical blading,

circumferentially non-uniform inflow will result in the generation of MPT noise as a result of variations in shock strengths associated with the flow non-uniformity at the fan. In an embedded inlet, interactions between this acoustic field and the flow can occur.

This research quantifies the effects of non-uniform flow on the generation and propagation of MPT noise. Understanding how the use of embedded inlets affects MPT noise is necessary to predict the noise which will reach the cabin and community in advanced aircraft configurations with embedded propulsion systems and boundary layer ingestion (BLI).

Figure 1-1: The Silent Aircraft Initiative SAX-40 featuring boundary layer ingestion and embedded propulsion systems.

1.2 Scope of Thesis

The problem under consideration is the identification and quantification of the mechanisms affecting the generation and propagation of MPT noise in inlets with non-uniform flow, such as those in embedded propulsion systems. The interaction of the airframe boundary layer with the inlet lip results in the generation of streamwise vorticity which is ingested into the inlet. In cases where the incoming relative flow is supersonic, the non-uniform flow in the inlet duct results in time-varying shock strengths in the relative reference frame. There is thus no frame of reference in which the flow is steady.

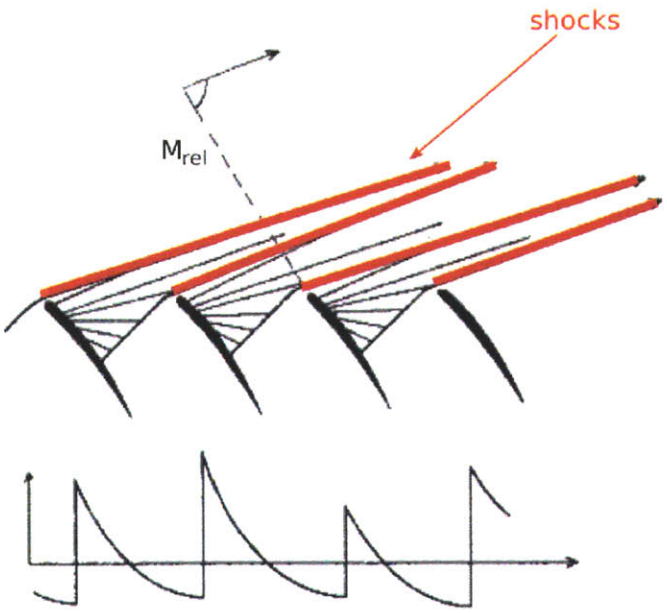

Figure 1-2: Schematic illustration of the generation of non-uniform shocks leading to multiple-pure-tone noise (from Hawkings [9]).

Within the inlet duct, the relative Mach number can be defined as

$$M_{rel} = \sqrt{M_x^2 + (M_B - M_\theta)^2 + M_r^2} \tag{1.1}$$

where M_B is the blade Mach number. Co-swirling flow (defined as $M_\theta > 0$) decreases M_{rel} while counter-swirling flow ($M_\theta < 0$) increases it. In addition, variations in axial Mach number and the introduction of a radial velocity component will affect M_{rel}. It is thus possible that the relative flow in the inlet will be supersonic for some circumferential locations (counter-swirling flow/increased axial Mach) but not for others (co-swirling flow/decreased axial Mach). The effects of these types of flow distortion on MPT noise are investigated.

This thesis seeks to answer three distinct research questions. First, is it possible to use a body force field to generate the non-uniform shocks which result in MPT noise, and what form must such a force description take? A viable modeling approach must respond to flow non-uniformities, and include the effect of varying blade stagger angles. Second, can the MPT noise thus generated be successfully propagated to the

far-field? Numerical dissipation must be minimized and accounted for in the far-field noise levels, and spurious wave reflections from flow boundaries must be avoided. Lastly, upon what factors and with what scaling does the generation and propagation of MPT noise in the presence of non-uniform flow depend? A parametric study must be employed to quantify the effects of flow non-uniformities on MPT noise. This involves interrogating the mechanisms by which the flow field affects the noise and establishing propagation criteria from first principles.

To address these research questions, a numerical approach is devised. The fan blade row is replaced with a force field which produces the same overall pressure rise and flow turning. This well-established [13, 14] technique is commonly referred to as using a *body force representation* of the blade row.

The key new idea is the addition of a rotating disturbance force field to model rotor shock noise. The force field is ultimately comprised of three superposed components: (1) the time-mean force field used to obtain the overall rotor performance, (2) a rotor-locked disturbance field, periodic over a blade pitch, to generate the system of shocks and expansion fans , and (3) a rotating disturbance field with once-per-revolution periodicity to generate variations in the shock system and thus MPT noise. The body force model is then used within an CFD calculation to simultaneously solve for the flow field, source noise generation, and acoustic propagation.

The capabilities of the approach described here are first assessed for a conventional axisymmetric inlet, for which extensive aerodynamic and acoustic experimental data is available [15–18]. To ascertain the effects of adding a serpentine duct to the inlet, a computation is carried out using an existing inlet geometry to quantify the resulting acoustic changes relative to the conventional inlet case. Then a parametric study of serpentine duct geometries is undertaken to gain insight into the relationship between boundary layer ingestion, inlet distortion, and the resultant changes in MPT noise. Finally, a response-surface correlation is developed and preliminary design guidelines are presented based on the interpretation of the results in the parametric study.

1.3 Challenges

Several major challenges needed to be overcome to enable the prediction of MPT noise generation and propagation in non-uniform flow.

1.3.1 Acoustics

The main challenge is implementing a body force field which acts as a noise source. The force field must accurately generate the system of expansion fans and shocks associated with a transonic rotor.

One important aspect is accounting for expected non-linear wave behavior consistent with the noise source being a rotor-locked shock/expansion fan system. In the presence of random blade stagger angle variations and/or non-uniform flow, the shocks generated by a transonic rotor will vary in strength temporally and/or circumferentially. The propagation of such a non-uniform shock system will result in the interactions of shocks with one another and with the flow field. The modeling approach used must therefore be capable of propagating non-linear waves.

Another challenge is determining which waves propagate acoustic energy in non-uniform flow. For cylindrical or annular ducts, the classical decomposition of the acoustic pressure field into circumferential and radial modes using Fourier series and Bessel functions, respectively, is appropriate only for uniform flow. In a non-uniform flow, the Helmholtz equation which governs the spatial acoustic field no longer has solutions which are comprised of these basis functions. Non-uniform flow requires a more general approach to the computation of acoustic power to enable accurate determination of cut-on/cut-off criteria.

1.3.2 Numerics

Due to the lack of symmetry in both the flow and acoustic fields, full-annulus computations are required. However, standard CFD approaches like unsteady RANS are not well-suited to acoustic propagation due to the necessity of using a computational interface between rotating and non-rotating parts of the domain. The mesh should

be fine enough to accurately capture the viscous effects within the blade row but also should be as uniform as possible to achieve accurate numerical acoustic propagation. To capture the wave propagation in a viscous computation, the cell sizes must be small to lower numerical dissipation. This raises the computational cost beyond what is currently practical. Even if the cost were not an issue, numerical dissipation can be problematic since it dissipates sound waves much faster than the physical bulk viscosity.

Even with a uniform grid in an inviscid solver, numerical dissipation is always present in the finite-volume codes typically used for CFD as it is added out of the need to numerically stabilize the scheme. Serpentine inlet duct lengths can be on the order of 10 times the acoustic wavelength for the blade-passing frequency. Over these long propagation distances, corrections must be applied to the far-field noise to account for the numerical dissipation in the unsteady solution. In addition, criteria for the spatial and temporal resolution of the highest-frequency waves of interest must be ascertained in order to determine the grid and time step sizes needed in the simulations.

Another numerical challenge associated with resolving acoustic waves is avoiding spurious reflections from flow inlets and outlets. The domain boundaries should admit the passage of waves without reflection, and special treatment of the boundary conditions is necessary.

1.4 Major Findings and Contributions

The findings of the thesis are brought together here. There are four main contributions summarized next and followed by a more detailed discussion.

1. The prediction of MPT noise generation and propagation in an Euler calculation has been enabled through the use of a body-force-based fan model which acts as the noise source, generating a rotor-locked system of expansion fans and shocks.

2. Swirl distortion[1] increases fan sound power by up to 38 dB compared to undis-

[1] In this thesis, the term "swirl distortion" is used to represent the effects of the streamwise vortices

torted inflow for the inlets, fan and free-stream flow speed studied. However, enhanced in-duct attenuation caused by reductions in relative Mach number due to co-swirling streamwise vorticity results in far-field overall sound pressure levels being increased by at most 18 dB. In the far-field, low-frequency tones are amplified while tones above one-half of the BPF are attenuated and appear to be cut-off. The mechanism responsible for the attenuation of the high-frequency (short-wavelength) tones is the creation of a region of subsonic relative flow in the inlet due to the co-swirling vortex.

3. Treating a non-uniform flow as uniform for the purpose of computing the sound power can result in over-prediction in flows with swirl distortion. The illustrative example presented has an over-prediction of 11 dB. To accurately determine sound power in non-uniform flow, integrating the local sound intensity is required.

4. The far-field cut-off frequency depends on the ingested streamwise vorticity and the external non-uniform flow. Results of a parametric study of serpentine inlets indicated that the changes in MPT noise due to swirl distortion are more important than changes resulting from the use of different inlet geometries for the cases investigated, which included only ducts for which the duct flow remained attached.

1.4.1 A New Capability in Fan Noise Modeling

Current approaches to fan noise prediction are generally capable of dealing with axisymmetric inlets and uniform inflow. In that situation, a steady computation in the fan frame of reference can be used. In non-uniform flow, there is no frame of reference in which the flow is steady, so a 3D, full-wheel, unsteady simulation is required. A non-linear solution is required since the shocks generated at the fan leading edge result in interaction between the acoustics and mean flow. Euler calculations capture the

in the inlet system rotating in the same (co-swirl) and opposite (counter-swirl) directions of the fan rotor.

acoustic propagation and allow the use of coarser grids than a RANS calculation, but the blade row cannot be accurately simulated without accounting for viscous effects.

A solution is to use a body force representation of the blade row. The enabling idea is to use a perturbation body force field to generate the rotor-locked shock system, allowing first-of-their-kind simultaneous calculations of the generation and propagation of MPT noise. The body force perturbation model is capable of capturing the effects of blade-to-blade stagger angle variations and inlet distortion on the expansion fan/shock system. Computed results using this approach are in agreement with experimental data for a conventional inlet for the shock system flow field and the far-field acoustics.

1.4.2 MPT Noise in Undistorted and Distorted Inflow

An assessment of changes in acoustic behavior due to fan installation in a serpentine, boundary-layer ingesting inlet was conducted. It was found that, relative to the conventional inlet, the SAX-40 serpentine inlet resulted in an increase in the sound power level at the fan by 38 dB due to the distorted inflow. Average far-field sound pressure levels increased by only 7 dB (3 dBA), so in-duct attenuation is much larger for the serpentine inlet. This suggests that it may be possible to shape the inlet duct to reduce noise such that the far-field noise does not increase due to the use of a boundary-layer-ingesting propulsion system.

The increased source power is suggested to be due to co- and counter-swirling vortices impacting the fan, which results in increased incidence angles and shock strengths. The non-uniform flow also enhances the acoustic energy carried by shaft-order waves cut-on at the fan. The increased in-duct attenuation is due to the co-swirling vortex which lowers the relative Mach number below sonic, causing locally evanescent wave behavior.

With boundary layer ingestion the far-field spectra are altered. There is amplification of tones below 1/4 BPF and attenuation of tones above 1/2 BPF such that these tones appear to be cut-off. The attenuation of short wavelengths is related to the size of the region of subsonic relative flow created by the co-swirling vortex. Wavelengths

on the order of the size of this region are more strongly attenuated than wavelengths of order of the duct circumference.

1.4.3 Assessment of the Impact of Non-Uniform Flow on Sound Power Propagation

For the swirl distortion in the SAX-40 inlet, the error introduced by assuming a uniform flow for the purpose of computing sound power was assessed. An approach which involves computing the sound power by integrating the local sound intensity is used as a baseline for evaluating the errors introduced by the uniform-flow assumption. The sound intensity integration approach does not involve any simplifying assumptions. For the test case investigated, it was found that employing the uniform-flow assumption can result in over-prediction of the sound power at the duct inlet plane by up to 11 dB compared to the results obtained by integrating the local sound intensity. The conclusion is that the sound-intensity-based approach should be used for determining sound power in non-uniform flow situations.

1.4.4 Effects of Boundary Layer Ingestion and Serpentine Inlet Geometry on MPT Noise

To determine how serpentine inlet geometry affects distortion transfer as well as MPT noise generation and propagation, a parametric study was conducted in which the duct upstream-to-downstream area ratio (1.01-1.05) and offset ratio (0.25-0.75) were varied while keeping the ingested boundary layer, fan corrected flow, body-force-based fan model, and free-stream flow ($M_\infty = 0.1$) constant.

The internal flows for the ducts studied are primarily differentiated by the presence of vortex lift-off which occurs for a duct with area ratio 1.01 and offset ratio 0.75. For this duct, the ingested streamwise vortices do not follow the duct geometry but instead lift-off the duct bottom and impact the fan near mid-span. A combination of enhanced axial Mach number at the inlet plane (0.69 compared to 0.61-0.67 for the other ducts) and larger normal pressure gradients within the duct bends (proportional

to duct offset ratio) results in vortex core streamtubes lifting off the duct bottom. This reduces in-duct sound power attenuation by 9 dB due to the effect of the counter-swirling vortex near mid-span. The vortex increases the relative Mach number and reduces the decay rate of cut-off waves, but this does not translate to the far-field noise levels because the additional acoustic energy is at frequencies above 1/2 of the blade-passing frequency, which are cut-off in the far-field.

This apparent far-field cut-off frequency is not dependent on the serpentine inlet geometry over the range of cases studied here but is instead set by the swirl distortion resulting from the ingestion of streamwise vorticity. The overall sound pressure levels do vary with duct geometry, increasing with both duct area ratio and offset ratio. The important trend is an increase in overall level of 3.8 dB between ducts with area ratios of 1.01 and 1.05 due to the change in inlet plane area altering the external flow upstream of the duct. Changes in overall level with duct offset ratio are less than 1 dB. In addition, it was determined that the far-field directivity is not directly a function of the duct parameters; however, it is altered as a result of in-duct vortex lift-off. Noise is reduced at emission angles less than 33° by up to 2.6 dB and is increased at higher emission angles by up to 1 dB. The mechanism responsible for this change is not yet clear.

The noise source generation (overall sound power at the fan) does not change with the duct geometry over the parameter ranges considered. It is instead set by the level of swirl distortion in the inlet. The similarity of the sound power spectra at the inlet plane for all ducts suggests that the apparent cut-off of tones above 1/2 BPF in the far-field is attributed to the external non-uniform flow outside the inlet. For a given fan corrected mass flow, the external flow varies only due to changes in the duct area ratio. This suggests that swirl distortion's effect on the acoustics is related to the amount of ingested streamwise circulation and the inlet pressure coefficient.

The parametric study showed that, within the parameter space explored, duct geometry has a secondary effect on the change in MPT noise in boundary-layer-ingesting inlets relative to conventional inlet results. The flow in all the inlets studied did not separate. It is predominantly swirl distortion which governs the increase in

source noise and the changes in propagation behavior in serpentine inlets at low flight speeds.

1.5 Organization of Thesis

The remainder of the thesis is organized as follows: Chapter 2 contains a review of relevant literature. Chapter 3 presents the development of a body-force-based fan model for both the time-average blade row behavior and the rotor-locked shock system which is the source of MPT noise. Chapter 4 shows that the flow field and noise produced by the model are in agreement with known experimental results. Chapter 5 compares the acoustic results obtained using the model for a case containing a serpentine inlet and boundary layer ingestion to the conventional inlet case assessed in Chapter 4. This serves as an initial investigation into the effects of non-uniform flow on source noise generation and propagation. In Chapter 6, the error involved in neglecting flow non-uniformities in the determination of sound power is assessed and an approach is presented which allows the sound power and its spectrum to be computed for arbitrarily non-uniform flows. Chapter 7 describes a parametric study of serpentine inlet designs and the results obtained for the flow fields and acoustic propagation. Chapter 8 discusses the outcomes of the parametric study, including both the development of a simplified response-surface correlation for the changes in far-field noise due to the presence of a serpentine inlet. This chapter also presents guidelines for reducing noise in embedded propulsion systems. Finally, Chapter 9 presents a summary of the work, conclusions, and recommendations for future work.

Chapter 2

Literature Review

2.1 Fan Noise Prediction

Previous work in fan noise prediction has focused mainly on conventional, axisymmetric inlets with circumferentially uniform inflow.

Morfey and Fisher [19] derived an analytical model for shock propagation from a fan in a constant-area, straight, circular duct. The derivation assumed that the shock propagation is one-dimensional, resulting in a direct relationship between the shock amplitude and the propagation time from the source. It was also assumed that the noise source from a transonic rotor can be represented by a sawtooth wave with initial magnitude set to correspond to the pressure rise across a normal shock at the tip relative Mach number. They considered only ducts with uniform mean flow. Farther than one blade pitch upstream of the source, this model gives a shock decay rate inversely proportional to the propagation distance. Comparisons with experimental data supplied by Rolls-Royce and General Electric, as well as more detailed calculations, revealed that the assumption of a uniform shock system at the fan and neglecting three-dimensional effects in the mean flow are the main sources of error with this model.

As inlet ducts are seldom uniform in cross-sectional area, Mathews and Nagel [20] expanded upon Morfey and Fisher's work by allowing the duct to have slowly-varying area (implying negligible three-dimensional influences on the mean flow) such that the

one-dimensional gas dynamic equations are used to determine the axial Mach number as a function of axial location. To accommodate this change, the assumption is made that the duct can be divided into concentric streamtubes and that the acoustic waves remain within their starting streamtubes. This model allows for prediction of the propagated noise and decay rate for any axisymmetric inlet. A key result is that reducing inlet throat area to increase the axial Mach number enhances the shock decay rate.

Han et al. [21] computed a 3D, single-passage solution for a transonic rotor to use as the noise source for a one-dimensional, nonlinear propagation code. The propagation problem is solved in the frequency domain using a complex Fourier series transformation of the one-dimensional Burger's equation. For an axisymmetric inlet with no inflow distortion this provides a propagation model that does not make any assumptions about the source waveform.

Prasad and Feng [22] numerically predicted the propagation of upstream-traveling waves in a conventional axisymmetric inlet. A single passage was considered, therefore assuming identical blades. The axisymmetric geometry allowed a steady computation to be carried out in the fan reference frame, greatly reducing computational cost as no separate propagation code was required. 3D flow effects were assessed by examining two inlets with different throat areas. The authors discovered that the increased local flow acceleration near the nacelle on the reduced-throat area inlet resulted in additional shock decay compared to predictions made using the Mathews and Nagel model. This approach could be used with a full-wheel computation in order to simulate MPT noise for axisymmetric geometries with circumferentially uniform inflow.

Gliebe et al. [10] used a decoupled approach to model MPT noise generation and propagation separately. Their goal was to develop an approach to predict noise emissions from a specific distribution of blade stagger angle variations. The noise source was determined from a half-wheel computation of the fan blade row in a rotating frame of reference. The blades were given small variations in stagger angle in order to produce MPT noise. The resultant pressure field was used as the input to

a frequency-domain propagation code. The effects of changes in stagger angle, blade thickness, camber, and pitch were considered. Stagger angle variations had the most significant effects on the propagated noise, and re-ordering the blades showed promise as a means to reduce MPT noise.

Coupland et al. [8] performed a high-fidelity simulation on an axisymmetric inlet with varying blade stagger angles to generate MPT noise, and propagated the noise through the inlet and to the exterior surface of the aircraft cabin in order to assess the cabin interior MPT noise. The computed in-cabin sound pressure levels were found to be within 5-10 dB of experimentally measured levels at frequencies above 20 times the fan shaft frequency. The fan was modeled using an approach similar to the one employed in Prasad & Feng, but a full-wheel simulation was used to enable computation of MPT noise. The propagation from the engine inlet to the fuselage was accomplished using separate aeroacoustic propagation codes. Despite the high computational cost of this approach, it was used to demonstrate the feasibility of solving all aspects of the MPT noise problem, including noise source generation, propagation within the inlet, and propagation through the external flow, using numerical tools.

The approach adopted by Coupland et al. shows the promise of using computational methods to predict MPT noise, but its high computational cost when the inlet has non-uniform flow presents an opportunity to develop a new approach in order to render tractable the study of the effects of inlet distortion on MPT noise generation and propagation.

2.2 Airframe-Engine Integration, Boundary Layer Ingestion and Flow in Serpentine Inlets

Boundary layer ingestion can improve propulsive efficiency by reducing the kinetic energy surplus in the engine exhaust. The use of integrated propulsion systems can maximize the amount of boundary layer ingested into an aircraft's propulsion system. However, aircraft with BLI and integrated propulsion systems pose many aerodynamic

design challenges. These include quantification of the aerodynamic benefits of BLI, determination of the aircraft performance impact of boundary layer ingestion, and understanding the role serpentine inlets play in distortion transfer.

The work of Sargeant [6] investigated the use of BLI in advanced aircraft designs as part of the Silent Aircraft Initiative. Key outcomes were that (1) at cruise, including the propulsion system has little effect on the lift generated compared to the "clean" (i.e. no engines) airframe; and (2) at takeoff, the upstream influence of the inlets alters the flow field on the airframe suction surface and this must be kept in mind when designing the airframe. In summary, from the airframe designer's perspective, using boundary-layer-ingesting engines does not pose any great challenges if the BLI design choice is known a priori.

The detailed study of flow through serpentine inlets with BLI was studied in Plas et al. [23] and Madani and Hynes [24]. Plas et al. conducted a parametric study of serpentine duct designs to determine the effects of duct geometry (offset ratio and area ratio) on the flow distortion at the downstream end of the duct as characterized by the pressure recovery and $DC(60)$ distortion coefficient. All the computations were conducted at the cruise condition. The results can be used to place bounds on what parameter space describing serpentine ducts results in acceptable levels of distortion at the fan. Madani and Hynes followed up on this work by considering the effect of the duct contour on the downstream distortion. Starting from the best case with minimum fan face distortion in [23], the duct contour was optimized for low fan face flow distortion. The optimized duct showed some improvement but the change in distortion was small compared to the change due to varying the duct offset and area ratios in [23]. The conclusion is that duct geometry parameters such as the offset and area ratios have a stronger effect than the details of the duct contour in determining the distortion transfer characteristics of a serpentine inlet duct.

Classical definitions of thrust and drag are ambiguous when a propulsor is present which re-energizes the wake of the aerodynamic body. A novel approach to the analysis of aerodynamic flows was therefore developed by Drela [7]. This approach bases the aerodynamic analysis around the concept of power balance, eliminating

the need to separately define thrust and drag. Using this approach, for a general two-dimensional airfoil (which can also serve as a model of a blended-wing-body aircraft such as the SAX-40), Drela demonstrated that a wake-ingesting propulsor would require up to 13% less power than a non-ingesting propulsor. This justifies the pursuit of BLI propulsion systems for fuel burn benefits.

The benefits of boundary layer ingestion for propulsive efficiency improvements presented in the work of Drela, and the distortion transfer characteristics of serpentine inlet ducts has been explored by Plas et al. and Madani and Hynes. However, these studies focused on the cruise condition. Information is not available at low flight speeds ($M_\infty \leq 0.25$) where MPT noise is of concern. At low speeds, the duct pressure recovery is as high as 0.99 and therefore stagnation-pressure-based distortion metrics such as the $DC(60)$ may not capture features which would be dominant, such as streamwise vorticity.

2.3 Acoustic Propagation in Non-Uniform Flow

In non-uniform flow, determining the acoustic energy propagating through a control surface is challenging. Several authors have developed general expressions for the acoustic energy in a non-uniform flow. One well-known work is that of Morfey [25], in which an acoustic energy equation valid in non-uniform flow was derived. The analysis was based on linear acoustics. Acoustic energy is a second-order quantity, i.e. it can be expressed as products of fluctuating quantities. Morfey used the linearized equations of motion to determine an the acoustic energy equation, which has the form

$$\frac{\partial E}{\partial t} + \frac{\partial W_i}{\partial x_i} = \Xi \tag{2.1}$$

in which E is the acoustic energy, W_i is the acoustic energy flux, and Ξ is a source term. In a statistically steady flow, the first term of Equation 2.1 is zero. The acoustic

energy flux is

$$W_i = \left(p' u_i^{*'}\right) + \frac{u_{0i}}{\rho_0 c_0^2}\left(p'\right)^2 + \frac{u_{0i}u_{0j}}{c_0^2}\left(p' u_j^{*'}\right) + \rho_0 u_{0j}\left(u_i^{*'} u_j^{*'}\right) \tag{2.2}$$

and the time average of W_i is the generalized acoustic intensity I_i. This represents the propagating acoustic energy, valid in any general flow. This description is useful as the influence of non-zero and/or non-uniform mean flow can be directly extracted. However, implementing this approach as a post-processing tool is challenging because it requires the separation of the fluctuating velocity field into irrotational and vortical components,

$$u_i^{*'} = u_i' - u_{\omega i}' \tag{2.3}$$

where $u_{\omega i}'$ is the vortical velocity fluctuation. To separate the irrotational and vortical components of a vector field post-priori, a Hodge-Helmholtz decomposition must be performed [26]. Performing this process numerically can lead to decreased accuracy due to the requirement of approximating the gradient of the vector field.

Myers [27] developed an approach which requires neither linearizing the equations of motion nor decomposing the fluctuating velocity field. An "exact energy corollary" was derived rather than an acoustic energy equation since for the nonlinear approach, the corollary's energy and flux terms do not correspond to any thermodynamic quantities such as internal energy or energy flux in the flow. This is because, for the nonlinear approach, the fluctuating quantities are not described by a set of governing equations as they are in the linearized case. The energy corollary takes the same form as the acoustic energy equation from Morfey

$$\frac{\partial E}{\partial t} + \frac{\partial W_i}{\partial x_i} = \Xi, \tag{2.4}$$

but the definitions of the terms are different. Instead of being an equation for acoustic energy in the strict sense (as is the case for Morfey's equation), this equation describes the behavior of generalized disturbances to the flow. Here the generalized disturbance

energy is

$$E = \rho\left[H - H_0 - T_0\left(s - s_0\right)\right] - l_o \cdot \left(u - u_0\right) - \left(p - p_0\right) \tag{2.5}$$

and the generalized disturbance energy flux is

$$\begin{aligned} W_i \;=\; & \left(l_i - l_{0i}\right)\left[H - H_0 - T_0\left(s - s_0\right)\right] + l_{0i}\left(T - T_0\right)\left(s - s_0\right) \\ & - \left(l_j - l_{0j}\right)\left(\frac{P_{ij}}{\rho} - \frac{P_{0ij}}{\rho_0}\right) + \left(T - T_0\right)\left(\frac{q_i}{T} - \frac{q_{0i}}{T_0}\right) \end{aligned} \tag{2.6}$$

where Ξ is again a source term and $l_i = \rho u_i$ is the linear momentum. The subscript 0 represents the time-averaged value of a quantity. H is the total enthalpy and p, T, s, ρ and u_i are the pressure, temperature, entropy, density, and velocity, respectively. P_{ij} is the viscous stress tensor and q_i is the heat flux vector. This approach can be employed to determine the disturbance energy intensity field in non-uniform flow from knowledge of the unsteady flow field.

Brambley and Peake [28, 29] investigated the propagation of linear acoustic waves through circular and annular ducts with radii of curvature comparable to the duct diameter and where the duct length to diameter ratio is large; the geometry examined in the paper had a length-to-diameter ratio of 7.1. The approach assumed potential flow. The duct curvature results in a breakdown of the symmetry of upstream- and downstream-propagating modes. In addition, the propagation of plane waves through curved inlets resulted in the concentration of the pressure disturbances in the outer portion of the duct. The key result obtained is that cut-on/cut-off criteria were not significantly altered from the straight-duct values for the potential duct flow considered.

Brambley and Peake's work demonstrates the importance of the duct geometry and non-uniform flow in determining the precise manner in which pressure waves propagate. However, in order to investigate the propagation of fan noise through boundary-layer ingesting inlets, in which the duct flow is rotational, a new approach must be developed. To accurately assess acoustic energy in inlets with rotational flows, Myers' generalized disturbance energy flux can be computed from the unsteady flow field.

2.4 Body Force Representations of Turbomachinery Blade Rows

Using body forces to represent the overall characteristics of a blade row was first introduced by Marble [13]. In this approach, the blade row is replaced with a volumetric force field which acts in the swept volume of the blade row and produces the same circumferentially-averaged effects on the fluid as does the blade row.

One technique that can be used to obtain the body forces corresponding to a given rotor was described by Gong [14]. Gong also examined the use of the body force model in non-uniform inflows and found that distortion transfer through the blade row was adequately captured.

Gong's approach is based on a 2-dimensional blade row model which assumed negligible radial streamline shifts. Source terms are added to the momentum and energy equations within the swept volume of the rotor to model the effect of the blade row on the fluid. The source term in the energy equation is a function of the circumferential force, rotor speed, and radius:

$$\vec{F} \cdot \vec{w} = F_\theta \Omega r \tag{2.7}$$

where $\vec{F}$ is the body force per unit mass and $\vec{w}$ is the blade-row relative velocity vector; Ω is the rotational speed of the blade row and r is the radial coordinate. The details of the derivation of the force expressions can be found in [14] and will not be repeated here, but the final expression for each force component is presented along with the main assumptions and limitations which apply to them.

The force acting on the fluid at a given location is divided into portions locally normal to and parallel to the flow a frame of reference moving with the blade row, $\vec{F_n}$ and $\vec{F_p}$. An additional term is also included to model the effects of the cross-passage pressure gradient in a staggered channel. This term takes the form

$$F_{n,\nabla p} = \frac{1}{\rho} \frac{\partial p}{\partial x} \sin \alpha \tag{2.8}$$

where α is the local blade camber angle. This force component acts in the normal direction. The remaining component of the normal force is

$$F_n = \frac{K_n(\alpha, x, r)}{h}(w_x \cos\alpha + w_\theta \sin\alpha)(w_\theta \cos\alpha - w_x \sin\alpha) \tag{2.9}$$

where h is the staggered spacing between the blades, and is given by

$$h = \frac{2\pi r\sqrt{\sigma}\cos\alpha}{B} \tag{2.10}$$

σ and B are the solidity and the number of fan blades, respectively. The square-root dependence on solidity assumes Carter's rule. Since the normal force model is based on a 2-dimensional idealized blade model, there is no radial normal force. Thus in component form:

$$F_{n,x} = F_n\frac{w_\theta}{w} \tag{2.11}$$

$$F_{n,\theta} = -F_n\frac{w_x}{w} \tag{2.12}$$

The force parallel to the flow is due to viscous effects within the blade row and is given by

$$F_p = -\frac{K_p(\alpha, x, r)}{h}w^2 \tag{2.13}$$

and has components

$$F_{p,x} = F_p\frac{w_x}{w} \tag{2.14}$$

$$F_{p,r} = F_p\frac{w_r}{w} \tag{2.15}$$

$$F_{p,\theta} = F_p\frac{w_\theta}{w} \tag{2.16}$$

The two empirical expressions K_n and K_p, are related to pressure and viscous effects respectively. They are introduced to capture the specific performance characteristics of the rotor blade row of interest. In Gong's work the empirical expressions were determined based on correlations at blade mid-span and tip for a given rotor

geometry using loss and deviation data from Lieblein [30]. In addition to K_n and K_p, the rotor geometry must be known since the spatial distributions of α and σ and the number of rotor blades B are also required for this body force model.

The overall body force per unit volume is obtained as a sum of these components:

$$F_x = F_{n,\nabla p} \cos\alpha + F_{n,x} + F_{p,x} \tag{2.17}$$

$$F_r = F_{p,r} \tag{2.18}$$

$$F_\theta = F_{n,\nabla p} \sin\alpha + F_{n,\theta} + F_{p,\theta} \tag{2.19}$$

and since the computational solver works in Cartesian coordinates, a transformation matrix is applied to obtain the forces that are used in the computation:

$$\begin{bmatrix} F_x \\ F_y \\ F_z \end{bmatrix} = \begin{bmatrix} 1 & 0 & 0 \\ 0 & \cos\theta & -\sin\theta \\ 0 & \sin\theta & \cos\theta \end{bmatrix} \begin{bmatrix} F_x \\ F_r \\ F_\theta \end{bmatrix} \tag{2.20}$$

To obtain the force per unit volume, which is required to implement the body force approach in a control volume CFD code, the force per unit mass is multiplied by the local fluid density ρ.

Gong's model is adapted, with some modification, for use in the present work to produce the time-mean body force field.

Chapter 3

Body-Force-Based Fan Model For Acoustic Computations

In this chapter, the modeling approach employed in this research is described in detail. The objective is to develop a body-force-based approach which generates the rotor-locked shock system and provides the pressure rise and flow turning associated with the blade row. The approach must also be capable of generating MPT noise and be suitable for incorporation in an acoustic computation framework. In particular, the determination of far-field noise and its correction for inherent solver dissipation, the modeling of boundary layer ingestion in inviscid computations, and the handling of wave reflections at flow boundaries are discussed in detail.

The viscous effects within the blade row are captured in the body force field. Since the intended use of the current model is for source noise generation, neglecting the hub and nacelle boundary layers is a reasonable assumption as long as the boundary layers within the inlet remain attached, which is the case for the low-speed external flows and the inlet geometries considered in this work. The body force model is therefore used within a three-dimensional full-wheel Euler calculation that includes the rotor, inlet, and far-field domain schematically illustrated in Figure 3-1. Including the internal and external flows in the CFD domain allows for the aerodynamics, acoustic source generation, and sound propagation to be computed simultaneously, capturing the coupling between them. The CFD software FLUENT [31] is used since

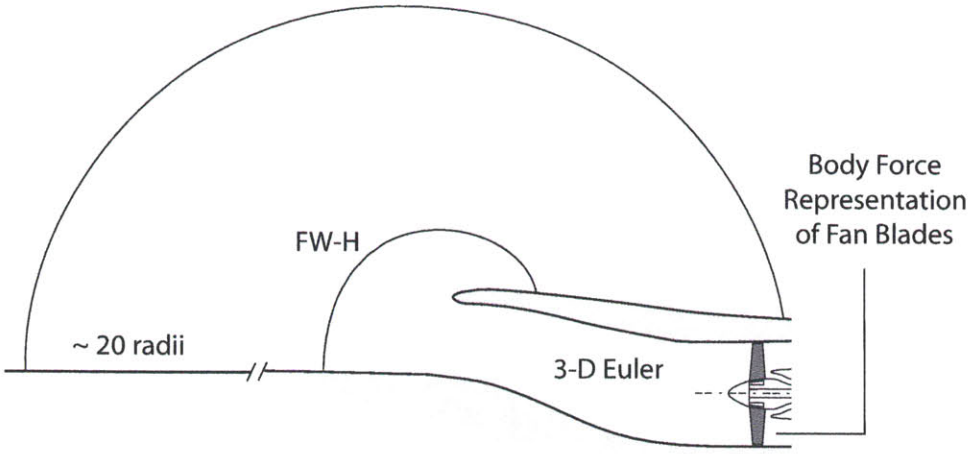

Figure 3-1: Schematic illustration of computational domain.

additional source terms can be implemented in the governing equations. Solving the fully nonlinear Euler equations allows waves of any magnitude as well as shock interactions to be captured. Since a single computational domain is used, the transition from in-duct to free-field propagation requires no special treatment. Reflections from solid surfaces are accurately modeled though no acoustic liner effects are included; hard walls are assumed for all inlet ducts studied.

The new idea in body force modeling, using rotating disturbances to generate MPT noise, is implemented as a superposition of three components: (1) the time-mean, locally axisymmetric force field, (2) a rotor-locked disturbance field, periodic over a blade pitch and (3) a rotating disturbance field with once-per-revolution periodicity.

The manner in which the components of the body force model are obtained and used is illustrated in Figure 3-2. For the rotor of interest, a single-passage 3D RANS calculation is used to obtain the steady body force and the (identical-blades) shock reconstruction disturbance field. A full-annulus 2D cascade RANS calculation with varying blade stagger angles is used to obtain the rotating disturbance with leads to MPT noise. The resultant fan model is used in an unsteady Euler calculation in which the noise source is generated and the acoustics are propagated through the inlet and to the far-field. Both the in-duct acoustics and the far-field spectra are captured for analysis. Once a body force model is developed for a rotor, it can be re-used with

alternate inlet geometries (i.e. serpentine inlets) without any modification.

First, the development of the time-mean body force model for the fan of interest is described. The blade pitch-periodic rotating disturbance model, used to generate the rotor-locked shock system, is then discussed. The production of MPT noise using a body force perturbation model is also presented. The approach used to obtain the far-field noise is then given. The far-field noise must be corrected for the inherent solver dissipation and the scheme employed to determine this correction is described. The requirements for modeling boundary layer ingestion in Euler computations are detailed, and finally the formulation of the acoustic buffer zones used to prevent spurious reflections from flow boundaries is presented.

3.1 Time-Mean Body Force Model

The time-mean force field is determined based on the *axisymmetric* flow field through the blade row. The body force field replaces the blade row, and the force expressions depend on blade geometry and the local flow variables. Since the force is a function of the local flow, in the presence of non-uniform and/or unsteady inflow the force field can vary circumferentially and/or in time. This is illustrated schematically in Figure 3-3. This allows the blade row to respond to inlet flow distortion.

The time-mean body force description follows the analytical expressions by Gong [14], as described in subsection 2.4. In the present work, single-passage RANS computations of the rotor of interest at various operating points are used to determine the empirical constants K_n and K_p. This process is described in the following subsection.

3.1.1 Analytical Description of Rotor Blade Row

The fan rotor chosen for study was the NASA/GE R4 model-scale research fan for which extensive aerodynamic and acoustic experimental results are available [15–18]. This 0.56 m diameter fan with $B = 22$ blades was tested in an aeroacoustic wind tunnel at a free-stream Mach number of 0.1 in a rotor-alone configuration as well as with 3 different stator designs. The experimental setup is shown in Figure 3-4.

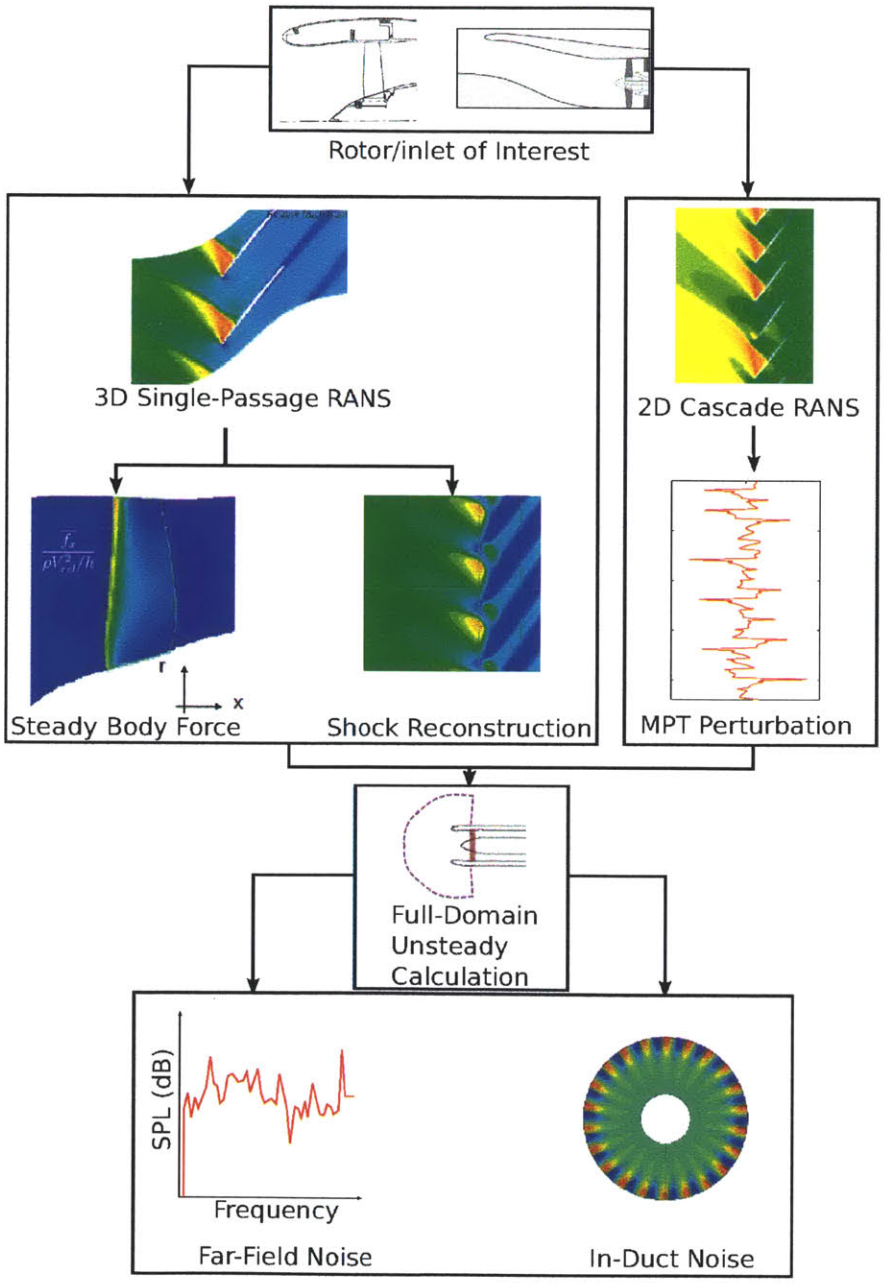

Figure 3-2: MPT Noise Prediction Framework.

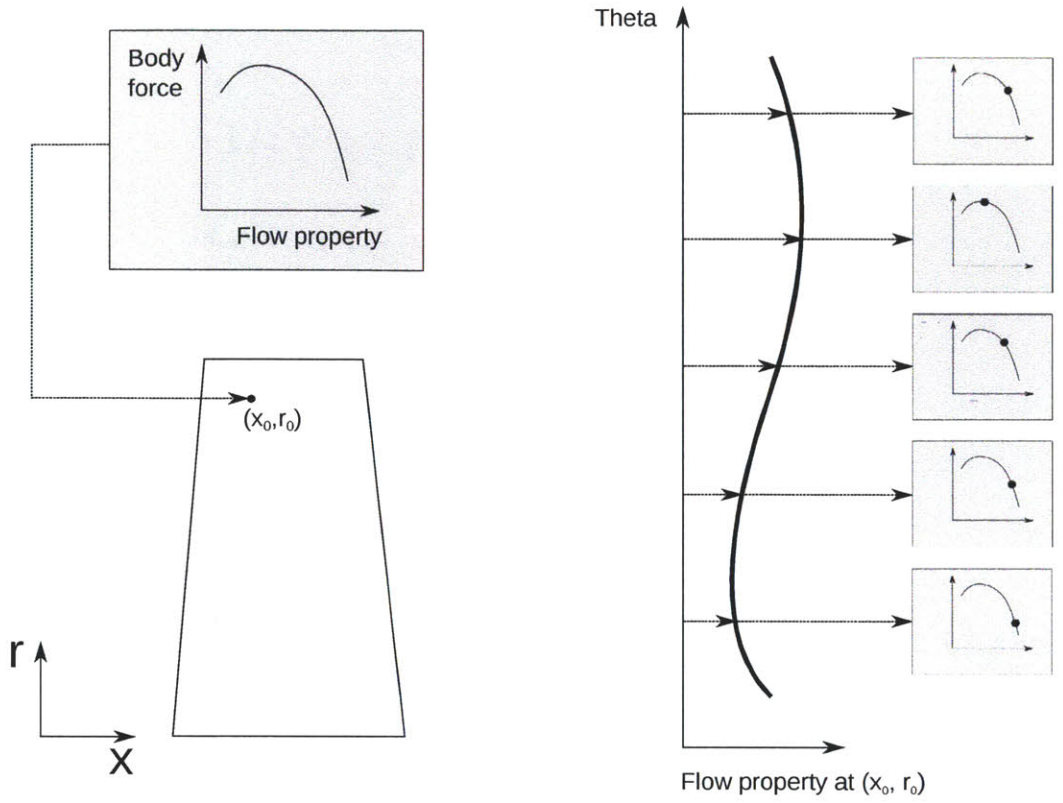

Figure 3-3: Dependence of body force field on local flow conditions (from Kerner [32]).

In order to implement the body force model, analytical expressions for the blade camber distribution α and solidity σ are needed. Based on the R4 rotor geometry [15], the following best-fit surfaces for these parameters were obtained:

$$\begin{aligned}\alpha &= a_0 + a_1\left(\frac{r-r_h}{r_t-r_h}\right) + a_2\left(\frac{x-x_{le}}{c}\right) \\ &\quad + a_3\left(\frac{x-x_{le}}{c}\right)\left(\frac{r-r_h}{r_t-r_h}\right) + a_4\left(\frac{r-r_h}{r_t-r_h}\right)^2 + a_5\left(\frac{x-x_{le}}{c}\right)^2 \end{aligned} \tag{3.1}$$

$$\sigma = s_0 + s_1\left(\frac{r-r_h}{r_t-r_h}\right) + s_2\left(\frac{r-r_h}{r_t-r_h}\right)^2 \tag{3.2}$$

where the coefficients a_i and s_i are given in Tables 3.1 and 3.2. $r_h = 0.0838$ m is the hub radius, $r_t = 0.2791$ m is the tip radius, $x_{le} = 0.1325$ m is the absolute axial coordinate of the blade row leading edge and $c = 0.07$ m is the mean axial blade chord. Figure 3-5 illustrates the definitions of the key parameters. The numerical

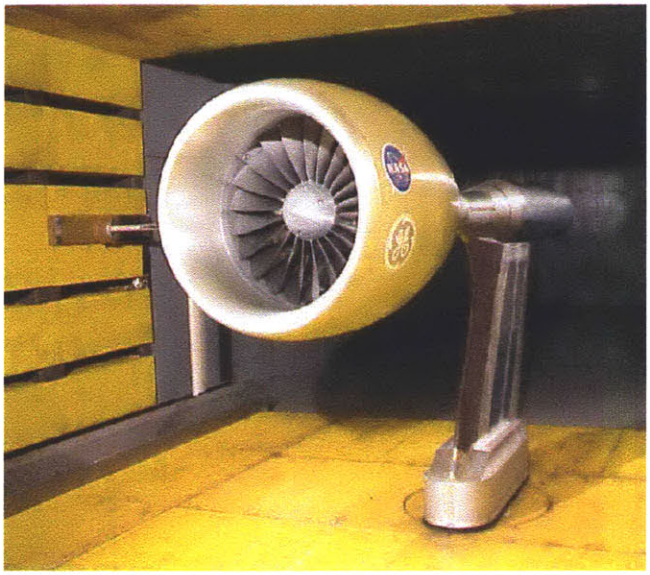

Figure 3-4: NASA SDT inlet and fan in aeroacoustic wind tunnel (from Hughes et al. [15]).

Table 3.1: Coefficients for blade camber distribution for the R4 rotor.

a_0	0.3047	a_3	0.7505
a_1	1.112	a_4	-0.4653
a_2	-0.6715	a_5	0.0020

values are based on the origin of coordinates being located at the spinner nose.

3.1.2 Determination of Empirical Constants

To obtain empirical expressions for K_n and K_p, single-passage, rotor-alone RANS CFD computations were performed using the turbomachinery code Fine-Turbo. The computations were carried out on a single-passage grid in the blade reference frame and included only the internal flow as shown in Figure 3-6. Turbulence closure was achieved through use of the Spalart-Allmaras one-equation model. The simulations

Table 3.2: Coefficients for solidity distribution for the R4 rotor.

s_0	2.85363
s_1	-3.90268
s_2	1.95421

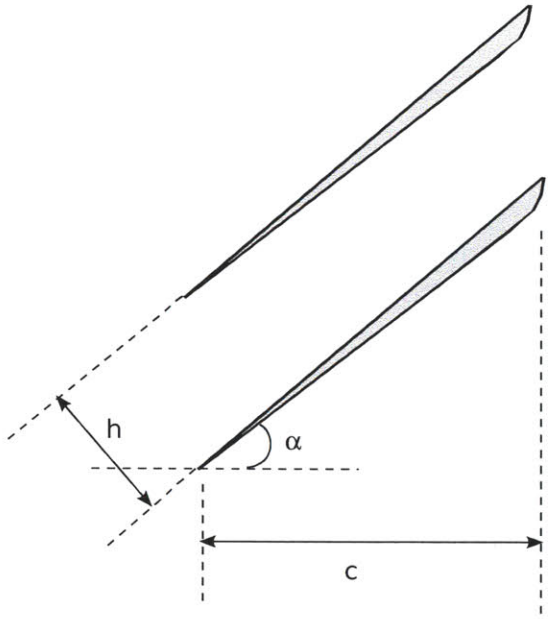

Figure 3-5: Rotor blade sketch illustrating definitions of the camber angle α, axial chord c, and staggered gap h.

were run along the 87.5% corrected speed line, which corresponds to the cut-back rotor speed for this fan. This rotor speed was chosen since this is the condition at which MPT noise is expected to be most prominent as the incidence angles are large leading to strong shocks.

A grid convergence study was undertaken in which solutions on grids of approximately 72,000, 240,000 and 658,000 cells were computed. Grid independence of the overall results is clear as the fan characteristic from the coarsest grid is in good agreement (within 1%) of the results from the finest grid, as shown in Figure 3-7. Figure 3-8 also shows that good agreement is obtained for the spanwise flow profiles. The circumferential grid, depicted in Figure 3-9 is less well-converged, with up to 4% variations in relative Mach number between the coarsest and finest grids. The three figures also indicate that the computed flow fields are in fair agreement with the experimental data.

To obtain K_n and K_p, the flow field is circumferentially (pitchwise) mass-averaged over the blade passage, resulting in a two-dimensional (axial and radial coordinates) field for pressure, relative velocity and temperature. The loading on the blades is also

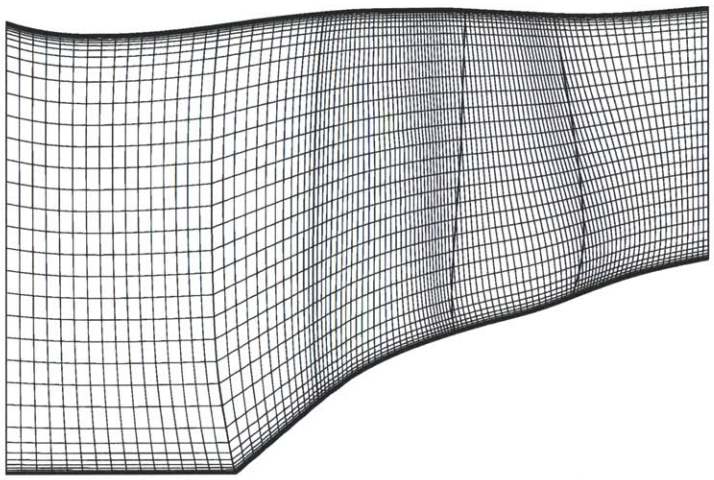

Figure 3-6: Medium-density single-passage computational grid for Fine-Turbo single-passage RANS CFD, comprised of 108 axial, 60 radial, and 24 circumferential cells outside the rotor block and with the rotor block (hidden) consisting of 80 axial, 60 radial and 28 circumferential cells.

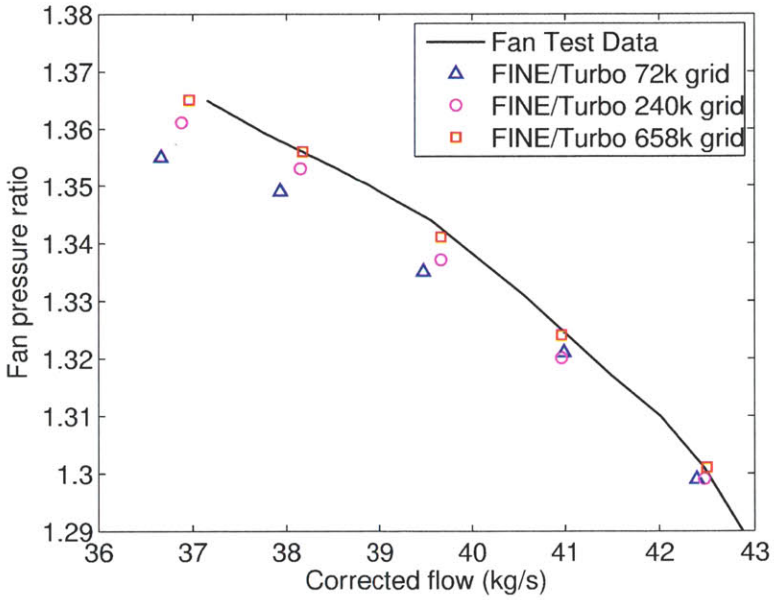

Figure 3-7: Grid study for single-passage RANS CFD: 87.5% corrected speed overall performance.

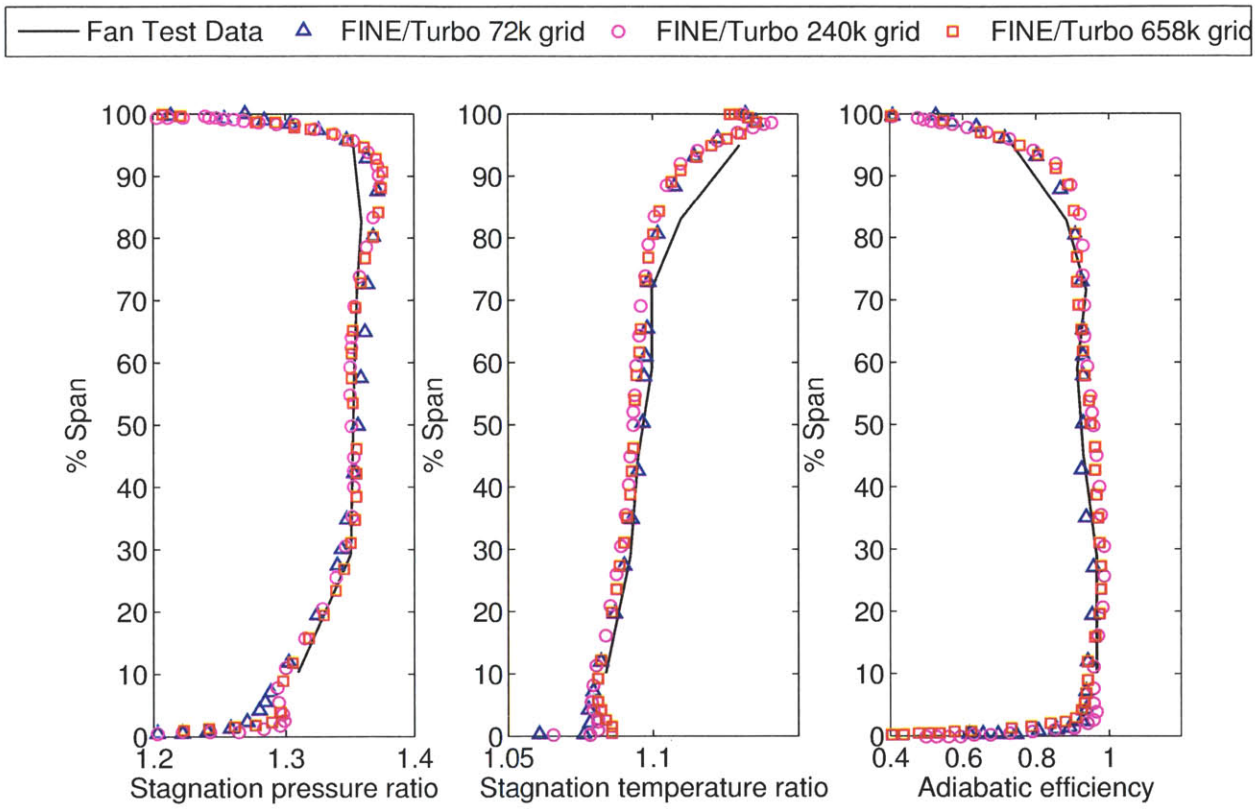

Figure 3-8: Grid study for single-passage RANS CFD: Profiles of stagnation pressure, stagnation temperature and adiabatic efficiency at the rotor trailing edge vs. span.

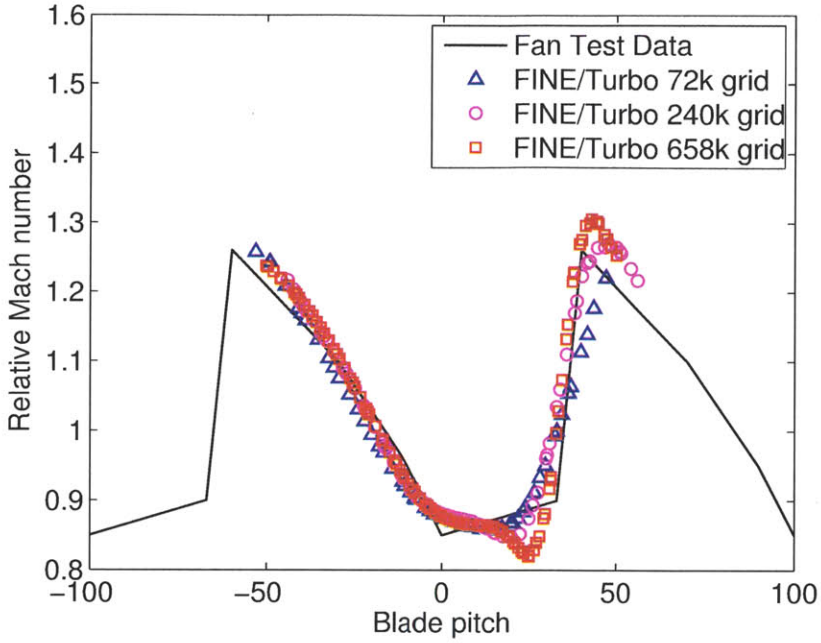

Figure 3-9: Grid study for single-passage RANS CFD: Relative Mach number distribution at 92% span, 1/4 chord upstream of fan leading edge.

needed to obtain the normal force and is computed by taking the differential pressure across the blade (in the direction normal to the local camber angle α) as a function of axial and radial coordinates and dividing by the local blade pitch (arc length of a passage at a given radius). This loading includes the pressure gradient term $f_{n,\nabla p}$ and therefore, based on the known circumferentially-averaged pressure field, this term is subtracted from the total normal force. A similar process is used for the shear stress in order to obtain the viscous force. This results in fields of force per unit volume normal and tangent to the blade camber surface; dividing by the local mass-averaged density results in the force per unit mass.

The mass-averaged flow and body force fields at the operating points considered are then used to solve Equations 2.9 and 2.13 in a least-squares sense for K_n and K_p. Following Gong [14], only flow field data from the mid-span and tip radii are included in the least-squares fitting process. As will be shown in Chapter 4, the error in fan pressure ratio is less than 1% and the exit flow angle distribution is in agreement with the single-passage computation results within 5° except for the innermost 20%

span, where it increases to as much as 20° due to the effect of the hub boundary layer on the relative Mach number. However, most of the work is done in the outer span, so that the performance obtained using data only from the tip and mid-span is adequate. Some trial-and-error is necessary in the fitting process to determine what functional forms for K_n and K_p provide a balance between accurate reproduction of the force field and simplicity of implementation. For the R4 rotor, the expressions used are

$$K_n = (4.2 - 3.3\alpha)\left(4.172\left(\frac{r - r_h}{r_t - r_h}\right)^2 - 3.118\left(\frac{r - r_h}{r_t - r_h}\right) + 2.145\right) \tag{3.3}$$

and

$$K_p = 0.05 \tag{3.4}$$

3.1.3 Governing Equations for the Body Force Approach

Though the forces are formulated in the blade frame of reference, the body force based calculation takes place in the absolute frame. Using the body force approach, computational effort is dramatically reduced and the griding requirements are simplified since the blade geometry is not included in the CFD grid. This allows the seamless coupling of inlet flow distortion transfer, acoustic source generation and duct propagation calculation in non-uniform flow.

The body force model in Gong [14] used a modified form of the Euler equations within the swept volume of the rotor, since the body forces are defined based on a circumferentially-averaged flow field. The formulation only allows the transmission of information in the circumferential direction through the body forces, since there are no circumferential fluxes in the governing equations; instead an additional term is added which scales circumferential gradients with the rotor speed Ω. This term appears as a result of the process used to obtain this specialized form of the Euler equations. First, the governing equations are transformed to the rotor reference frame. The flow is made axisymmetric in this reference frame by removing all circumferential gradients. Finally, the equations are transformed back to the absolute frame. Appendix A

contains a derivation of this specialized form of the Euler equations.

Consider Equations 3.5 and 3.6, which are the full and specialized forms of the Euler axial momentum equation respectively. In axisymmetric flow the underlined terms in both equations are zero and the equations are equivalent. However, in non-axisymmetric flow the circumferential flux terms are not necessarily equal. The modified equation only allows circumferential flux through the rotation of the blade row. For example, a stator, with $\Omega = 0$, cannot have a circumferential flux due to the presence of the blades; any circumferential turning of the flow is instead handled through the body forces.

$$\frac{\partial u_x}{\partial t} + u_x \frac{\partial u_x}{\partial x} + \underline{\frac{u_\theta}{r}\frac{\partial u_x}{\partial \theta}} = -\frac{1}{\rho}\frac{\partial p}{\partial x} + \frac{F_x}{\rho} \tag{3.5}$$

$$\frac{\partial u_x}{\partial t} + u_x \frac{\partial u_x}{\partial x} + \underline{\Omega \frac{\partial u_x}{\partial \theta}} = -\frac{1}{\rho}\frac{\partial p}{\partial x} + \frac{F_x}{\rho} \tag{3.6}$$

Implementation of the specialized approach in FLUENT proved challenging since the flux terms in the governing equations cannot be altered, though arbitrary source terms can be added. While it is possible to add flux-cancellation source terms to obtain an approximation to the modified Euler equations, in practice this results in compounding numerical errors which cause the solver to become unstable. Therefore the viability of using the full Euler equations even within the rotor swept volume is investigated. From the equations above and the scaling analysis contained in Appendix A, it can be seen that the ratio of the full Euler circumferential flux term to the rotor-frame transformation term (underlined terms in Equations 3.5 and 3.6 respectively) scales with the inverse of the reduced frequency β, where

$$\beta = \frac{2\pi\Omega r_t c}{\lambda u_x} \tag{3.7}$$

In Equation 3.7, r_t is the outer radius of the rotor and c is the mean axial rotor chord. Therefore, for the shaft-order disturbance wavelengths associated with MPT noise ($\lambda = 2\pi r_t$) the reduced frequency for a typical rotor is of order unity

$$\beta = \frac{\Omega c}{u_x} \sim 1 \tag{3.8}$$

indicating that the two terms are of the same order of magnitude (and of the same sign). One term can therefore be exchanged for the other in the governing equations so long as the reduced frequencies of interest are primarily of order unity. The full Cartesian Euler equations with body forces are thus used in the present implementation, even within the rotor swept volume. It is the upstream effects that are critical for noise generation and propagation. Since this change affects the convective terms in the governing equations, any effect on the distortion transfer will primarily be confined to the flow within and downstream of the blade row. However, the inaccuracy introduced by using the full Euler equations increases with β. This is manifested as a spatial filtering which prevents length scales much smaller than a blade pitch from being resolved.

3.2 Rotor-Locked Shock Generation

In order to add the new capability of shock reconstruction to the body force approach, a rotating force field is formulated. The rotating field, periodic in one blade pitch, is comprised of the time-mean axisymmetric component and of a component which depends both on location within the rotor swept volume and on the level of the time-mean body force. This circumferentially-varying component rotates at the angular speed of the fan and integrates to zero to minimize the change in overall performance for the rotor as a result of its inclusion. The shock structure is reconstructed via a periodic rotor-locked perturbation of the time-mean body force field based on the rotor upstream pressure field in a single-passage 3D RANS computation for the fan of interest. Only the formulation of the axial body force is varied, as this is sufficient to generate the shocks; the other force components adjust as they also depend on the local flow. The modified axial body force is given by

$$F_x(r,x,\theta,t) = \overline{F_x}\left(M_{rel}(r,x,\theta), \alpha(r,x)\right) + \delta F_x(r,x,\theta-\Omega t) \tag{3.9}$$

where $\overline{F_x}$ is the time-mean body force field, M_{rel} is the relative Mach number and α is the local blade camber angle. δF_x is the perturbation to the body force, given by

$$\delta F_x = \overline{F_x}\left(M_{rel}, \alpha\right) \cdot \nu \cdot S\left(r, x, \theta - \Omega t\right) \tag{3.10}$$

In Equation 3.10, S is a dimensionless shaping function whose variations in the r and θ directions are as shown in Figure 3-10. The shaping function resembles the static pressure distribution upstream of the rotor in the θ and r directions from the single-passage 3D RANS computation. The circumferential variation of S was chosen after a sensitivity study revealed that for the R4 rotor, upstream of the blade row, the circumferential pressure distribution and related flow features are not sensitive to the details of the shaping function as long as a triangle-wave shape is used since the amplitude is controlled by the parameter ν. This is conjectured to be due to the spatial filtering of the governing equations used in the body force approach, as well as the fact that any force perturbation with a discontinuous slope will cause non-uniform flow turning which will generate a shock/expansion fan system for supersonic relative inflow. As mentioned above, S is constructed such that

$$\int_{\theta}^{\theta+2\pi/B} S\left(r, x, \psi - \Omega t\right) d\psi = 0 \tag{3.11}$$

where B is the number of blades in the rotor. With this the overall performance characteristics of the rotor are unchanged.

The axial variation of S is a step function with value 1 in the first 15% of the axial chord and 0 elsewhere since the focus is on shock generation which occurs in the leading edge region of the blade row. Restricting the variation to the front part of the blades helps to reduce the inaccuracies introduced by using the full Euler equations as opposed to Gong's modified equations. The 15% chord extent was determined to be the best compromise between accuracy of the shock reconstruction and the inaccuracy of the flow downstream as a result of the use of the full Euler equations in the blade row.

The parameter ν, constant over the whole rotor, defines the scaling of the body

force changes with the dimensionless shaping function. In order to determine the value of ν, a parametric study was conducted. The value of ν was iterated until the variations in the upstream shock strength were in agreement with the 3D RANS results. A value of $\nu = 46$ achieves good agreement for the rotor used when the maximum absolute value of the shaping function S is 1, as will be seen in Chapter 4.

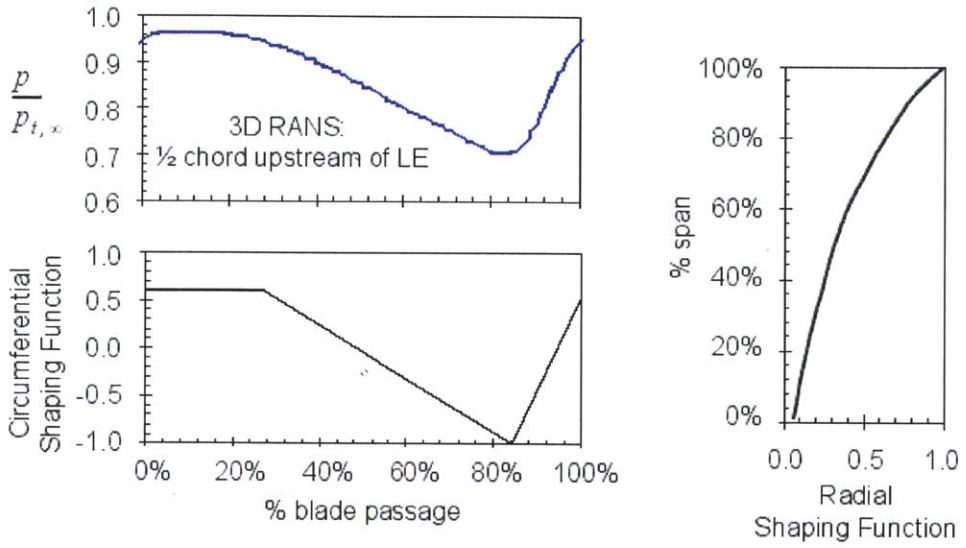

Figure 3-10: Shaping function S dependence on θ and r, showing relationship to upstream RANS pressure field.

3.3 MPT Noise Generation

Since MPT noise in uniform inflow is caused only by blade-to-blade variations in stagger angle, the passage-width periodic force perturbation developed in the previous section must be modified on a passage-by-passage basis. This is accomplished by introducing another perturbation to the body force field. The MPT-noise-producing perturbation is based on a random distribution of stagger angle changes, resulting in the variations in shock strength and propagation direction necessary to produce the once-per-revolution periodic pressure field associated with MPT noise. The critical step in the generation of MPT noise via body forces is the definition of the scaling for

the body force field passage-to-passage variation with blade stagger angle changes. The scaling was determined via 2D cascade calculations with perturbed blade stagger angles. This viscous calculation was conducted for the full annulus at 85% span using the Spalart-Allmaras turbulence closure model. The stagger angle of each of the 22 rotor blades for the NASA/GE R4 fan was perturbed randomly between $-0.2°$ and $+0.2°$, resulting in non-uniform shock generation as depicted in Figure 3-11. This range of stagger angle variations is consistent with results reported in the literature [10]. The axial Mach number corresponds to the cut-back operating point corrected flow.

To introduce variations from one passage to another in the rotor in the body force model, the perturbation is redefined:

$$\delta F_x = \overline{F_x}\left(M_{rel}, \alpha\right) \cdot S^*\left(r, x, \theta - \Omega t\right) \tag{3.12}$$

where the scaling which produces an accurate match between the flow fields in the 2D cascade and the 3D body force computations is $S^* = \left(1 + \Delta\chi(b)\right) \nu S$. $\Delta\chi(b)$ is a scalar, constant within each of the B blade passages ($1 \leq b \leq B$), which is randomly varied from passage to passage; as implemented, it is a uniformly-distributed random variable representing the change in blade stagger angle in radians:

$$-0.2° \frac{\pi}{180°} \leq \Delta\chi(b) \leq 0.2° \frac{\pi}{180°} \tag{3.13}$$

The choice of using a uniform distribution for the random variable helps to achieve a greater degree of variation in the stagger angles obtained than would result from using a normal distribution, enhancing the range of shock strengths obtained. The above formulation results in the difference in pressure changes (normalized by the inlet stagnation pressure) between the strongest and weakest shock being the same in the 2D, viscous, full-wheel cascade computation and in the 3D body force method. In addition, the complete waveforms in both cases have similar standard deviations. These overall characteristics are more important than the details of the waveform since in reality the blade stagger angle distribution is different for each manufactured

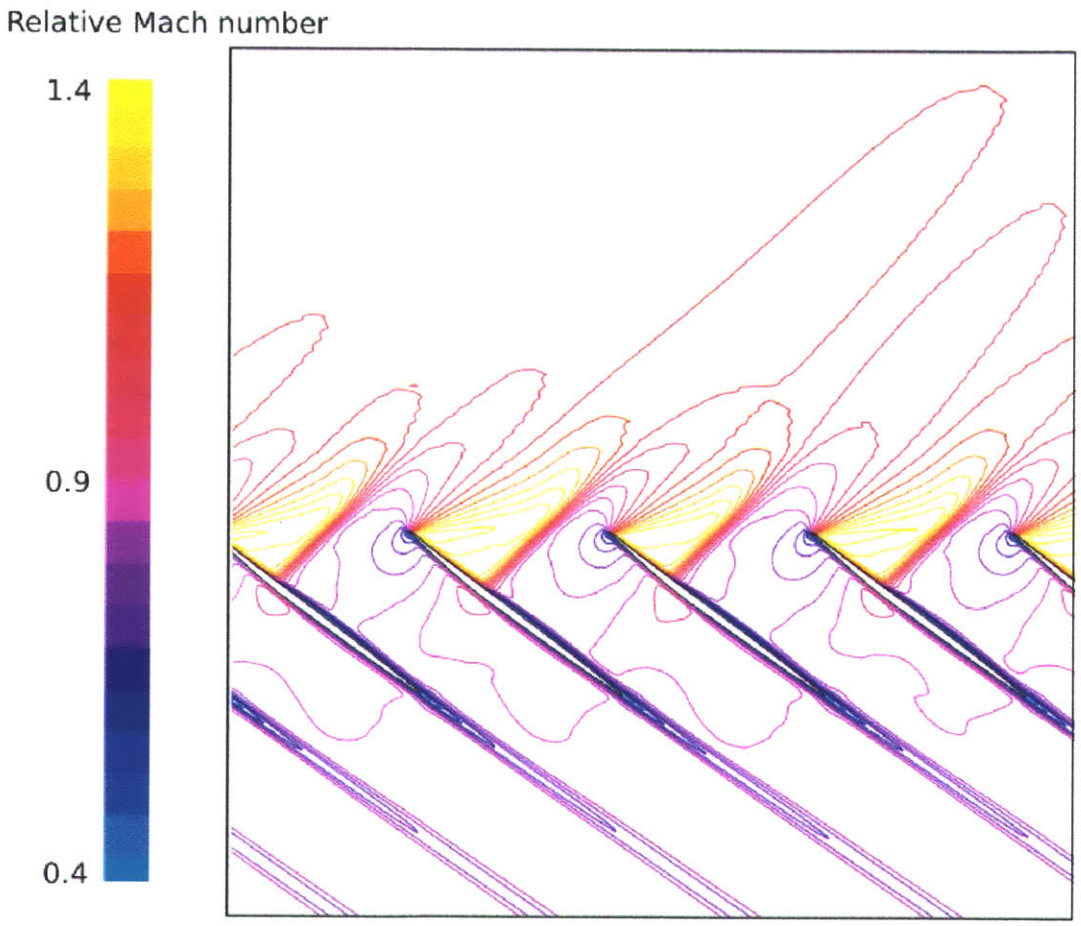

Figure 3-11: Shock generation in a 2D cascade with blades with non-uniform stagger angles.

rotor. The normalized pressure distributions at 85% span, one-half chord upstream of the rotor leading edge for the cascade and body force computations are shown in Figure 3-12. Good agreement is obtained for the range of shock strengths, defined by the difference between the highest and lowest deviations from the mean pressure.

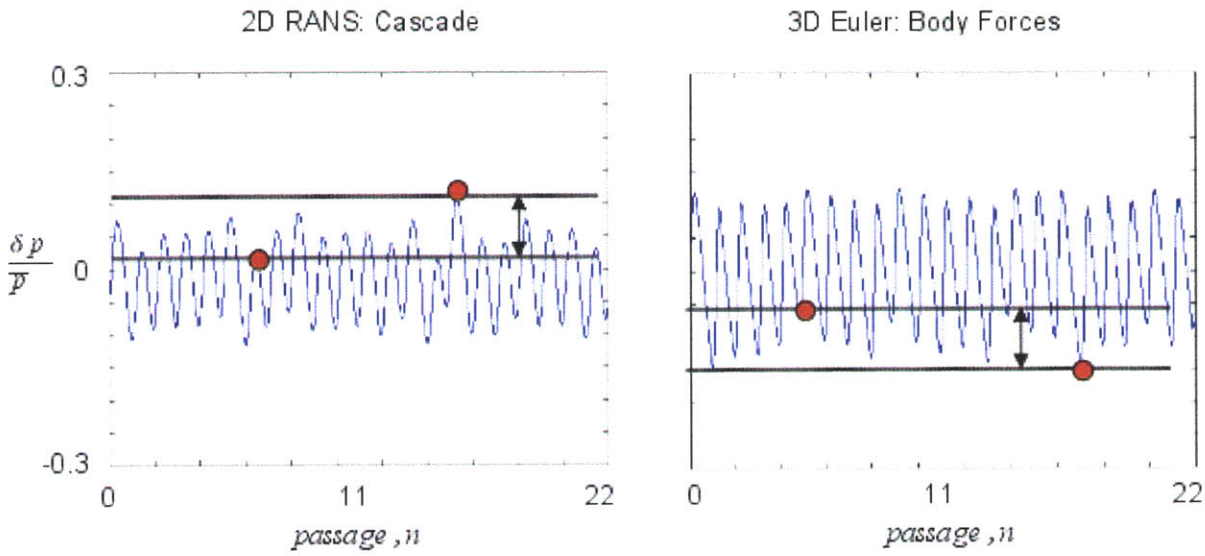

Figure 3-12: Static pressure 1/2 chord upstream of the rotor leading edge at 85% span (blue). The red dots indicate the minimum/maximum deviations from the mean pressure. The black lines indicate the resultant maximum variation in shock strength.

3.4 Far-Field Noise Modeling

The Ffowcs-Williams and Hawkings [33,34] (FW-H) integral method is used to determine the sound pressure levels at far-field receiver locations. To reduce computational cost, it is desirable to minimize the volume enclosed by the FW-H integration surface. This is because the fine grid required for resolving acoustic waves is needed only within that enclosed volume. To ensure accuracy of the far-field predictions, however, the surface is placed 1.5 fan diameters from the inlet, since the FW-H method does

not account for the effect of flow non-uniformities on acoustic propagation. This is far enough from the inlet that the average pressure coefficient (normalized by the free-stream dynamic pressure) on this surface is approximately -0.05, which is only 0.3% of the mass-averaged pressure coefficient at the inlet.

3.5 Correction for Inherent Solver Dissipation

Viscous effects in the fan blade row are captured through the body forces which are implemented as source terms in an inviscid calculation. The 3D Euler equations are solved to compute the unsteady flow throughout the domain. There is a signal-to-noise ratio (SNR) of 10 dB or more at the Ffowcs-Williams and Hawkings integration surface (and thus at the far-field microphone locations) for the tonal noise. The SNR is limited by the numerical dissipation which occurs in the Euler solver to ensure numerical stability. This dissipation rate is solver-specific and can be quantified on a per-cell basis as a function of the wave resolution in points per wavelength (PPW). Given the cell sizes and an estimate of the wave propagation distance from the source (rotor) to the FW-H integration surface the far-field noise levels can therefore be corrected for this numerical attenuation.

The inherent dissipation present in the inviscid, 2nd-order, density-based FLUENT solver is characterized to account for the non-physical wave decay in the far-field noise levels. A method based on the work of Huttl et al. [35] is used to characterize the numerical attenuation of the solver. A numerical experiment is conducted with plane waves of various wavelengths imposed as time-varying static pressure at one of the boundaries of a rectangular domain. A best fit to the resulting wave decay is shown in Figure 3-13 and is described by

$$Dec = Y \cdot PPW^{Z} \quad \frac{\text{dB}}{\text{cell}} \tag{3.14}$$

where PPW is the spatial wave resolution; for the solver used, $Y = 110$ and $Z = -2.7$.

To obtain the effective cell size, an assumption must be made about the direction in which a wave passes through each cell. The RMS length of all possible lines through

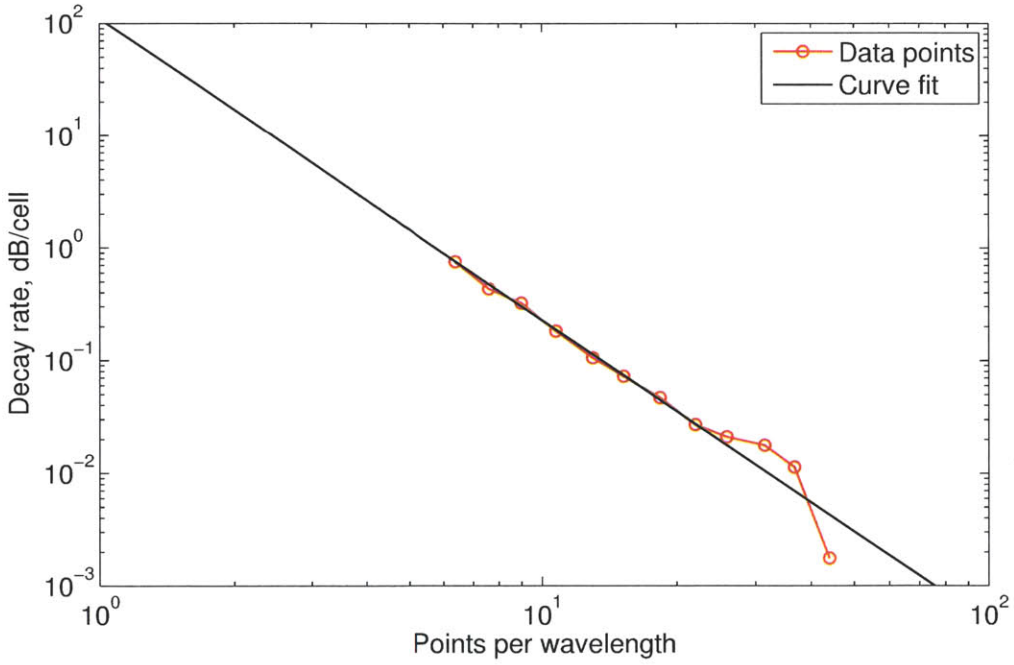

Figure 3-13: Euler solver wave decay as a function of points per wavelength based on numerical experiments similar to an impedance tube test. Curve fit is $Dec = Y \cdot PPW^Z$ with $Y = 110$ and $Z = -2.7$.

a cubic cell is chosen to determine the effective cell size. Assuming that all grid cells are cubes with sides of length Δx, the RMS distance a wave travels through a cell $\Delta\lambda_{RMS}$ is given by:

$$\frac{\Delta\lambda_{RMS}}{\Delta x} = \left[\left(\int_0^{\pi/4} \sec^4\psi d\psi\right)^2\right]^{1/2} = \frac{4}{3} \tag{3.15}$$

where Δx is the cubic cell side length. Equation 3.15 is derived below.

3.5.1 Derivation of RMS Wave Traversal Distance Through a Cubic Cell

Consider a cube with sides of length Δx. A line traversing the cube, originating at one corner, can be specified by angles in orthogonal planes, ψ and ϕ, as indicated in Figure 3-14. Both angles range from 0 to $\pi/4$. These lines have lengths

$$\Delta\lambda = \frac{\Delta x}{\cos\psi\cos\phi} \tag{3.16}$$

so that the RMS line traversal length is

$$\Delta\lambda_{RMS} = \left[\Delta x^{-2}\int_0^{y=\Delta x}\int_0^{z=\Delta x}\Delta\lambda^2 dydz\right]^{1/2} \tag{3.17}$$

But the rectilinear and angular coordinates are related by

$$y = \Delta x\tan\theta \tag{3.18}$$

$$z = \Delta x\tan\phi \tag{3.19}$$

so that

$$dy = \Delta x\sec^2\psi d\psi \tag{3.20}$$

$$dz = \Delta x\sec^2\phi d\phi \tag{3.21}$$

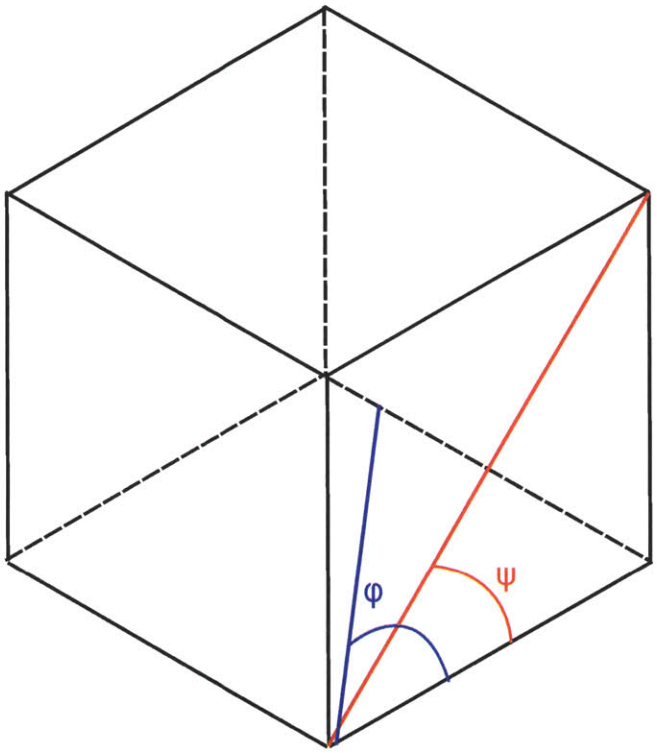

Figure 3-14: Cubic cell with angle definitions.

Equation 3.17 can then be written as

$$\frac{\Delta\lambda_{RMS}}{\Delta x} = \left[\int_0^{\pi/4}\int_0^{\pi/4} \sec^4\psi \sec^4\phi d\psi d\phi\right]^{1/2} \tag{3.22}$$

$$\frac{\Delta\lambda_{RMS}}{\Delta x} = \left[\left(\int_0^{\pi/4} \sec^4\psi d\psi\right)^2\right]^{1/2} \tag{3.23}$$

The integral in Equation 3.23 can then be evaluated analytically to give

$$\begin{aligned}\frac{\Delta\lambda_{RMS}}{\Delta x} &= \left|\left(\frac{1}{3}\tan\psi\left(\sec^2\psi+2\right)\Big|_0^{\pi/4}\right)\right| \\ \frac{\Delta\lambda_{RMS}}{\Delta x} &= \frac{4}{3}\end{aligned} \tag{3.24}$$

which is the result that was given in Equation 3.15.

3.5.2 Application of Solver Dissipation Correction to Far-Field Noise

The goal is to obtain a simple correction spectrum for far-field noise for a given geometry, free-stream flow velocity, and duct velocity. To account for the numerical decay in a particular propagation problem, the number of cells a wave passes through as it propagates from the source to the observer must be estimated. This requires knowledge of the nominal cell size and the distance from source to receiver. The distance from the inlet plane (throat) to all the points on the FW-H surface is assumed to be constant and equal to 1.5 fan diameters. To approximate the distance a wave must travel from the source to the FW-H surface, both the in-duct and external propagation distances must be estimated. It is assumed that waves at all propagating modes and frequencies travel the same distance in order to render the problem tractable. To account for the fact that the waves spiral around the duct, the in-duct propagation distance used is not the streamwise duct length but rather the wave propagation distance in an equivalent-length cylindrical duct with a mass-averaged Mach number corresponding to the fan corrected flow, averaged over all propagating modes and frequencies of interest. While a more accurate estimate of the dissipation could be obtained by estimating propagation time rather than distance, due to the non-uniform mean flow this would be more challenging to determine. Since a simple post-processing tool is sought, the distance metric is used moving forward.

The increase in propagation distance for a wave spiraling around a cylindrical duct relative to the streamwise duct length is simply the ratio of the total to axial wavenumbers:

$$\frac{\Upsilon_{spiral}}{\Upsilon} = \frac{k}{k_x} \tag{3.25}$$

The NASA/GE R4 inlet duct geometry and axial Mach number at the cut-back operating point is used to determine the above ratio for all cut-on modes and frequencies assuming uniform flow in the inlet to take advantage of the resulting analytical solution to the Helmholtz equation governing the unsteady pressure field. Averaging the

resultant set of ratios gives

$$\frac{\overline{\Upsilon_{spiral}}}{\Upsilon} = 1.14 \tag{3.26}$$

The total wave propagation distance is then given by summing the in-duct and external propagation distances:

$$\Upsilon_{wave} = L_{duct}\left(\frac{\overline{\Upsilon_{spiral}}}{\Upsilon}\right) + 1.5D_{fan} \tag{3.27}$$

With these assumptions, the total decay is the product of the decay per cell and the number of cells through which the waves travel, approximated using the total propagation distance Υ_{wave} and a representative cell size Δx, taken to be 1/20 of the fan tip blade pitch. The sensitivity of Υ_{wave} to the ratio $\frac{\overline{\Upsilon_{spiral}}}{\Upsilon}$ is thus the duct length. The conventional inlet used in this work has $\frac{L_{duct}}{D_{fan}} \approx 0.5$ while the serpentine inlets studied have $\frac{L_{duct}}{D_{fan}} \approx 2.5$. The correction for the serpentine inlets is therefore approximately five times more sensitive to the value of $\frac{\overline{\Upsilon_{spiral}}}{\Upsilon}$ than is the correction for the conventional inlet. However, given the goal of creating a simple far-field noise correction, the wave propagation distance Υ_{wave} is applied in the same way to both the conventional and serpentine inlet geometries.

To apply the results to the far-field spectra, is more useful to convert the wave resolution in points per wavelength to frequency based on the far-field sound speed. For the conventional inlet used to assess the approach in Chapter 4, the resultant correction curve is shown in Figure 3-15. This correction curve is applied to the far-field spectral noise results in order to amplify tones, compensating for the numerical dissipation inherent in the solver. Other correction curves obtained using the same procedure were determined and utilized for all other inlet geometries considered in this thesis.

For the computations carried out in this work, the frequency resolution of the far-field noise is one-half of the shaft frequency. Frequencies are amplified based on the assumption that harmonics of the shaft frequency which are elevated in sound level compared to both the next-lowest and next-highest half-shaft frequencies are tones. The shaft-harmonic component must exceed the levels of the neighboring frequency

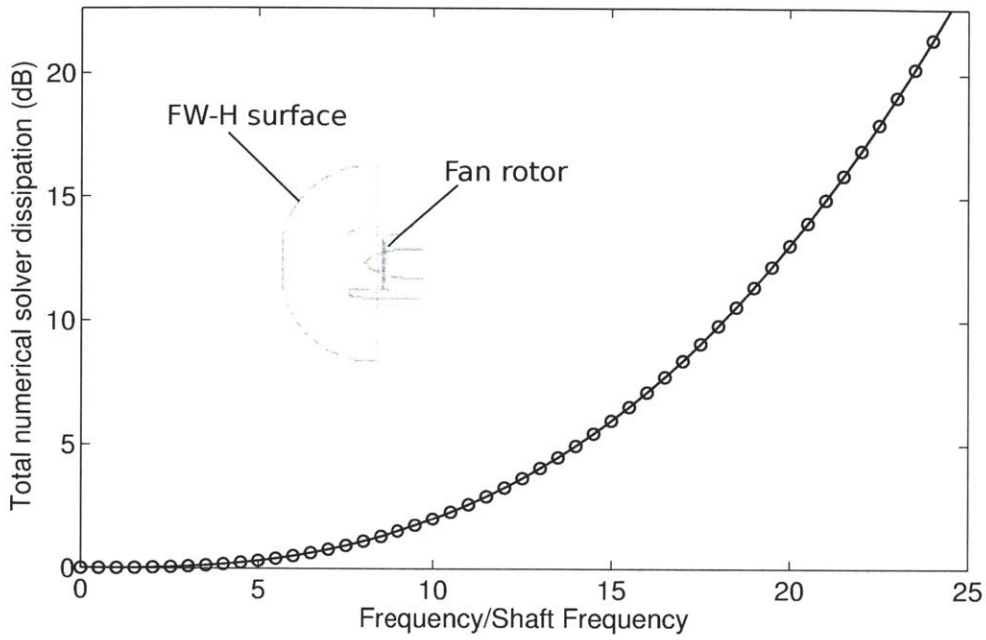

Figure 3-15: Total numerical wave decay from fan face to FW-H surface vs. frequency for the conventional inlet validation case.

components by 3 dB in order to be amplified as a tone. The sensitivity of this tone-selection criterion was varied between 1 and 5 dB. Values exceeding 3 dB did not appreciably alter which frequencies were identified as tones.

3.6 Modeling Boundary Layer Ingestion in Euler Computations

An important aspect of modeling inlet distortion in embedded propulsion systems is capturing boundary layer ingestion. Since an Euler solver is used for the computations in this work, special consideration is required. An appropriate stagnation pressure deficit profile must be introduced at the domain flow inlet to ensure that the boundary layer ingestion is accurately modeled in the inviscid computation.

For the problem of interest, air flows over the airframe before encountering the embedded inlet in the aft portion of the aircraft. In order to determine the details of

the boundary layer stagnation pressure profile at the entrance to the embedded inlet, the computed viscous flow field over the SAX-29 airframe with no engines [36] is used due to the availability of detailed flow simulation data. The obtained dimensionless boundary layer profile is applied at the flow inlet in the computations containing the serpentine inlets with the boundary layer thickness set to the value at the location of the inlet plane. The spanwise variation in boundary layer thickness is also included in the inlet profile. This profile convects from the flow inlet 10 fan diameters upstream towards the duct inlet. This technique captures the non-uniform inflow to the embedded inlet and the ingestion of the airframe boundary layer. For the low-speed external flow conditions considered ($M_\infty = 0.1$), the most important feature of the non-uniform inflow is the ingestion of streamwise vorticity generated as a result of the interaction between the incoming boundary layer and the inlet lip. Streamline curvature effects are expected to be more important than viscous effects within the duct since only ducts with attached flow are considered in order to obtain acceptable fan performance.

3.7 Acoustic Buffer Zones

When computing the propagation of acoustic waves, special treatment is necessary to ensure that the domain inlet and outlet boundaries do not reflect outward-traveling waves back into the computational domain. In this work, acoustic buffer zones based on the work of Freund [37] are implemented. Freund's approach involves extending the computational domain from inlet and outlet boundaries to include buffer zones in which additional terms are added to the governing equations which actively damp the flow variables towards their running averages. Thus when outgoing waves reach the domain boundaries, they have been attenuated sufficiently that the reflections are negligible.

The current approach uses a combination of grid stretching and Freund's explicit damping of acoustic waves within the buffer zones to attenuate waves incident to and reflected from the domain flow boundaries. This combination reduces wave ampli-

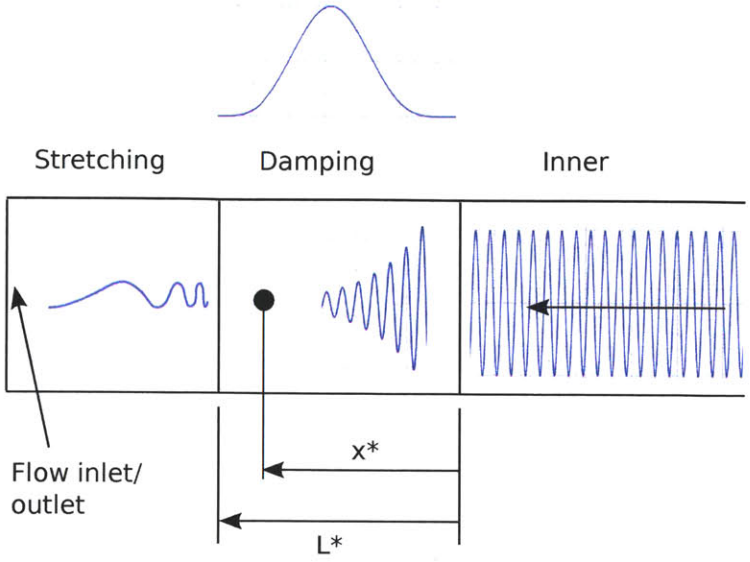

Figure 3-16: Schematic illustration of acoustic buffer zone implementation.

tudes passing through the region by approximately 60 dB. The damping term scales as $\sin^4\left(\frac{x^*}{L^*}\right)$, where x^* is the straight-line distance from a point in the damping region to the nearest point outside the region towards the inner part of the domain (where the acoustic waves originate) and L^* is the minimum straight-line distance through a point from the inner to outer parts of the domain. On the outer side of the damping region is a grid stretching region which further reduces wave amplitudes such that the reflections from the domain flow boundaries do not impact the inner part of the domain. This is schematically illustrated in Figure 3-16. For the internal flow boundary (downstream of the fan in Figure 3-17), both active damping and grid stretching are used. For the external flow boundaries, due to attenuation from spherical spreading, the implementation of grid stretching alone proved to be sufficient to prevent unwanted reflections.

3.8 Concluding Remarks

In this chapter, a new approach was described which can be used to compute the generation and propagation of MPT noise for general inlet geometries without having to include the fan blade geometry in the computational domain. A body-force-based fan

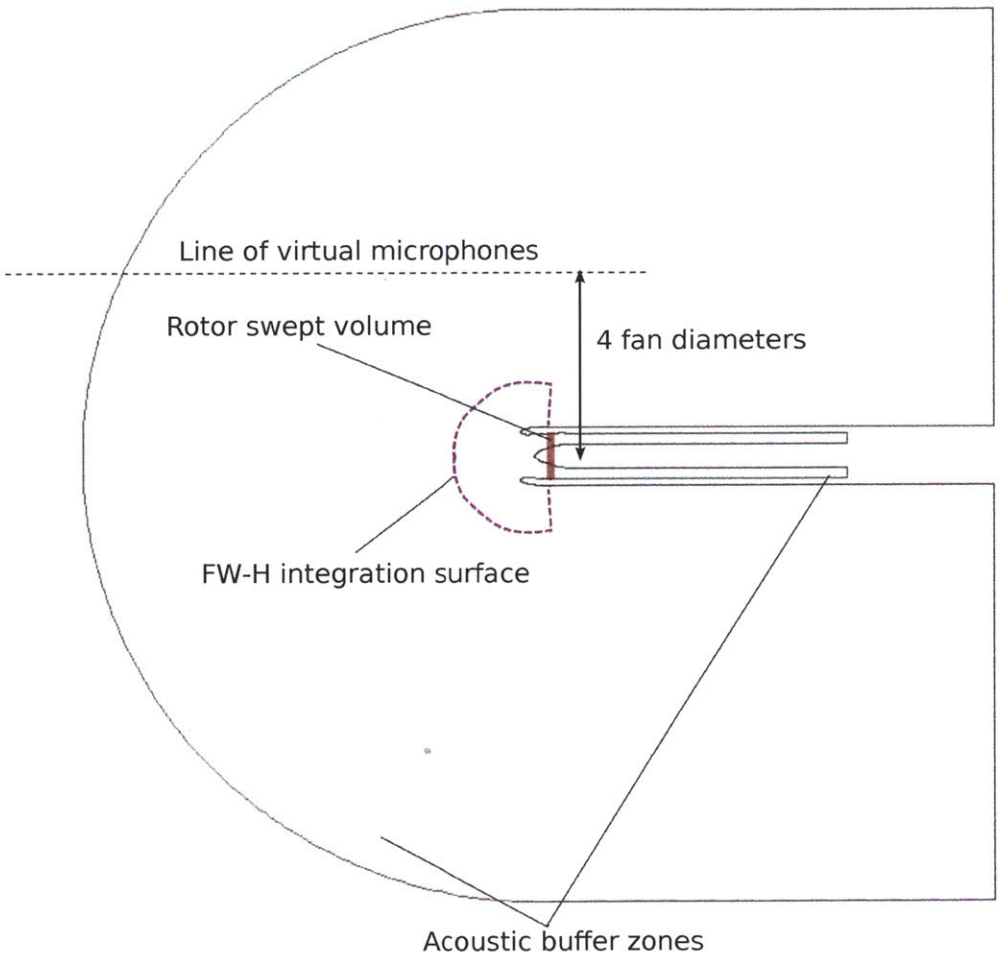

Figure 3-17: Computational domain showing locations of acoustic buffer zones.

model is used to simulate the pressure rise and flow turning effects of the blade row on the fluid. Body force perturbations are added to generate the shock and expansion fan system which is the source of MPT noise. The development of the time-mean force and the shock generation models are based on single-passage 3D RANS computations, while the passage-to-passage force variations which produce MPT noise are determined from a 2D full-wheel cascade computation. The coupled computational approach employs a single domain for the flow field, source noise generation, and noise propagation. Far-field noise is captured using the Ffowcs-Williams and Hawkings integral method. Implementation challenges regarding numerical dissipation and artificial wave reflections are addressed by characterizing the solver dissipation and using acoustic buffer zones, respectively. The following chapter presents the results of a study undertaken to assess this approach.

Chapter 4

Model Assessment

In this chapter, the body-force-based approach to MPT noise generation is implemented for the NASA/GE R4 fan. Experimental data is available for this fan installed in a conventional, axisymmetric inlet from NASA's Source Diagnostic Test [15–18]. The goal of this chapter is to assess the overall rotor performance, the acoustic source generation in terms of shock strength and the far-field noise in order to ensure that the model adequately represents the fan blade row and captures the MPT noise propagation in the inlet duct and in the external flow. The assessment is conducted for frequencies up to and including the blade-passing frequency in order to focus on MPT noise.

The assessment demonstrates that the body-force-based approach can be used to predict overall blade row performance and to generate MPT noise as well as the blade-passing tone. The fan total pressure rise is predicted with less than 3% error at the cut-back operating point and the rotor-locked shock system is predicted with at most 6% error in the relative Mach number distribution. The far-field noise levels are in fair agreement, with an RMS error for the blade-passing tone of 8 dB over emission angles between 25° and 65°. The assessment of changes in MPT noise due to boundary layer ingestion will be on a relative basis, so this level of agreement is acceptable. The accuracy of the generation of the rotor-locked shock system combined with the agreement of the far-field noise levels indicate that the acoustic propagation is correctly modeled in the computation. It is observed that the interaction of the

non-uniform shocks leads to the redistribution of acoustic energy from high-spatial-order (e.g. blade-passing wavelength) to low-spatial-order (e.g. duct circumference) modes.

4.1 Computational Setup

The experimental acoustic data available for comparison to the computational results encompasses far-field spectra at receiver locations spanning emission angles Θ_{em} from 25° to 130° as well as a modal decomposition of the acoustic field at the inlet throat for the blade-passing frequency. The emission angle corrects a geometric angle for the change in acoustic propagation direction due to the presence of a mean flow [17]:

$$\Theta_{em} = \Theta_{geom} - \sin^{-1}\left(M_{\infty} \sin\left(\Theta_{geom}\right)\right) \tag{4.1}$$

where M_{∞} is the free-stream Mach number and Θ_{geom} is the geometric angle, measured from the fan axis from aft looking forward such that 90° corresponds to the same axial position as the fan leading edge. The steady flow field and overall rotor performance, the detailed unsteady pressure field, the acoustic transfer function of the inlet duct, and the far-field spectra from the computation are analyzed and compared with the experimental results where applicable.

The rotor-alone configuration is used for the assessment to eliminate the effects of the stator blade row on the acoustics [15, 17]. The computational domain consists of the fan, upstream and downstream ducts, and upstream external flow region as shown in Figure 3-17. The full-wheel computational grid consists of approximately 17 million hexahedral cells. Cross-sections of the grid upstream of the rotor are depicted in Figure 4-1. The free-stream Mach number is 0.1, consistent with the experimental wind tunnel tests, and the fan operates at 87.5% rotor speed and a model-scale corrected mass flow of 38.0 kg/s at the cut-back operating point.

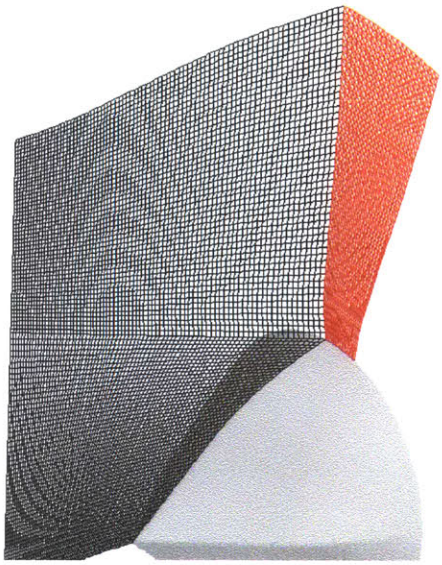

Figure 4-1: Computational grid for validation on conventional inlet.

4.2 Overall Time-Mean Fan Rotor Performance

As discussed in Section 3.1, the time-mean body force model is determined from 3D RANS single-passage computations of the NASA/GE R4 rotor with undistorted inlet flow and checked against experimental measurements. The results are shown in Figures 4-2 and 4-3. At the model-scale corrected flow for the cut-back operating point (38.0 kg/s), the body force approach yields a pressure ratio of 1.36, which is in good agreement with the experimental steady rotor performance. In Figure 4-3, the circumferentially-averaged shock surface is visible near the rotor blade tip for both the pitchwise-averaged 3D RANS and body force results. The differences in relative exit flow angle observed near the rotor hub in Figure 4-4 can be attributed to the use of flow field and force data from only the mid-span and tip radii for the determination of the body force coefficients K_n and K_p as well as to the lack of a boundary layer on the center-body in the Euler-based body force computation. The inner radius discrepancy has a small (less than 1%) overall impact on the fan pressure ratio since most of the work input in the rotor, as well as the shock generation, occurs near the outer radius.

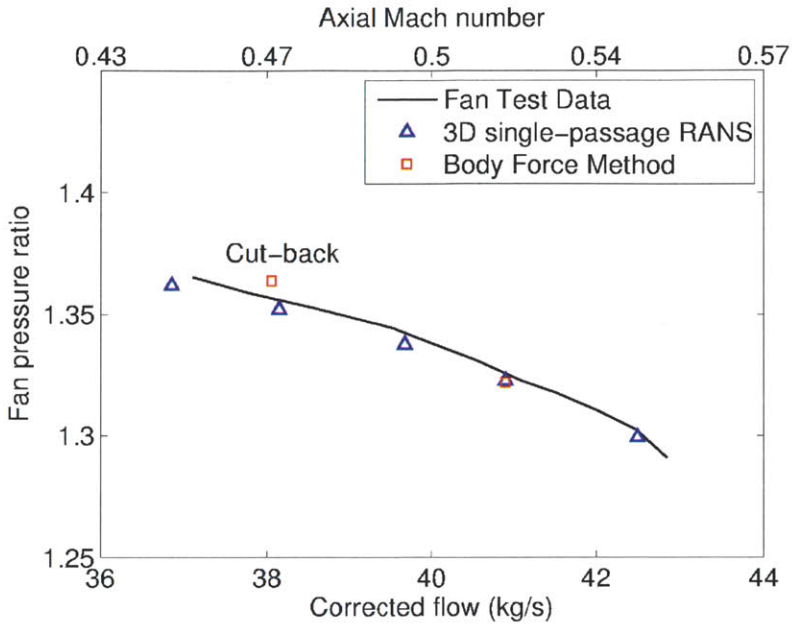

Figure 4-2: Pressure ratio vs. corrected flow at 87.5% corrected design speed for the NASA/GE R4 rotor.

4.3 Off-Design Performance

The operating point (based on corrected mass flow) considered in this thesis is the cut-back condition. Non-uniform flow alters the local inflow conditions to the blade row,

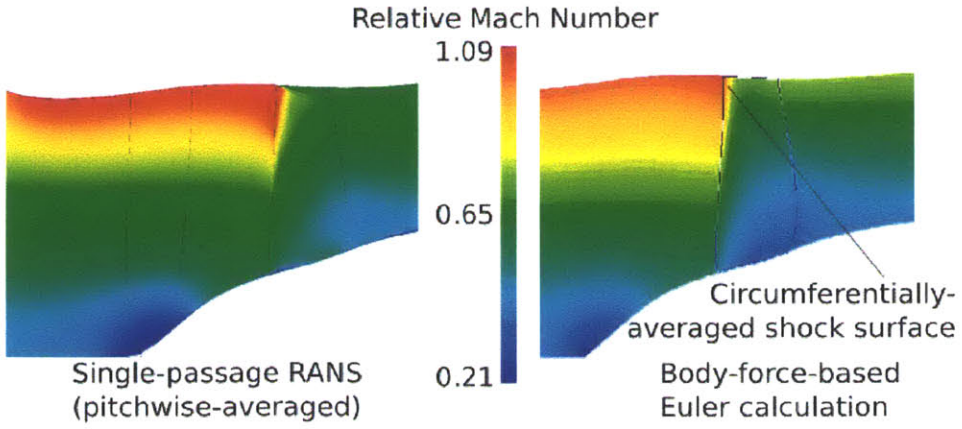

Figure 4-3: Comparison of meridional plane relative Mach number fields for NASA/GE R4 fan rotor at cut-back condition.

which produces local variations in the axial Mach number and stagnation pressure ratio. These variations are assessed to demonstrate the capability of the body force model to treat off-design performance. Figure 4-5 depicts the locus of operating points at the tip radius for the most-distorted inflow condition encountered in this thesis (blue), with the cut-back condition shown in red. The full range of axial Mach numbers in the locus lies within the set of RANS operating points upon which the body force description was based. Therefore the body force model is expected to provide an adequate estimate of the fan performance even for the most significant flow distortions considered in this thesis.

4.4 Acoustic Source Generation

Experimental measurements of the flow field just upstream of the rotor [16] are used to assess the capability of the model to accurately generate the rotor-locked shock structure. It was not clear a priori that generating shocks via a rotating body force field could adequately represent the key noise generation mechanisms. Figure 4-6 demonstrates that the required rotor-locked field of expansion fans and shock waves is indeed generated by the body force model, including the blade-to-blade stagger

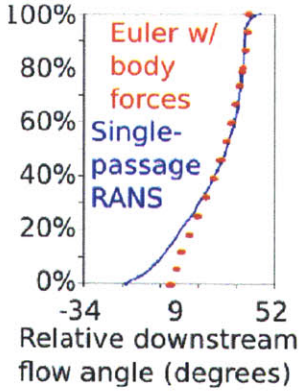

Figure 4-4: Downstream flow angle comparison between RANS (blue) and Euler with body forces (red) for NASA/GE R4 fan rotor at cut-back condition.

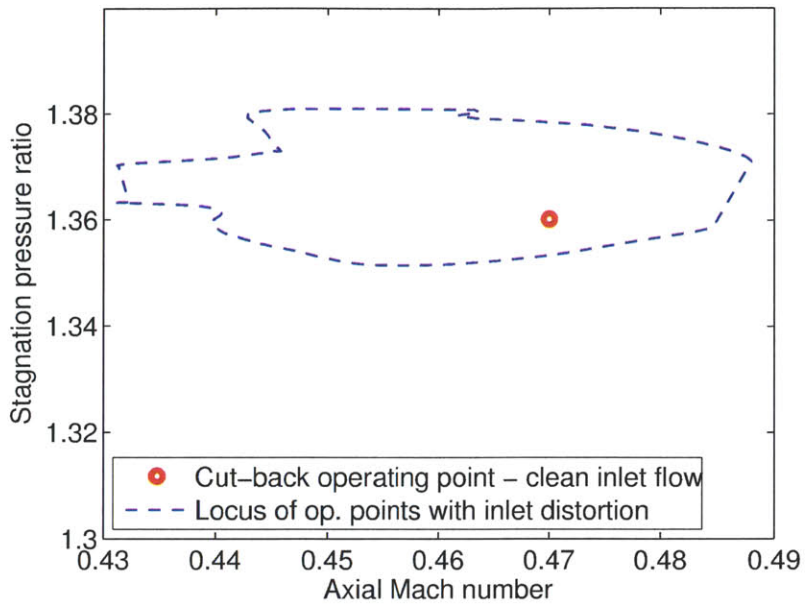

Figure 4-5: Locus of operating points around the circumference near the blade tip for inlet flow distortion.

angle perturbation. The figure depicts the experimental and computed relative Mach number at 92% span, 1/4 chord upstream of the rotor leading edge. Both results represent average passage distributions with the effects of non-uniform blade stagger removed, since the exact blade stagger angle variations in the experimental rotor are unknown. The agreement in amplitude is expected due to the a priori determination of the scaling factor ν for uniform inflow conditions. The computed saw-tooth pattern has a 6% under-prediction of the peak relative Mach number and slightly shallower slopes in relative Mach across the expansion fan as a consequence. Since the R4 rotor has 22 blades, the time step size in the unsteady body force computations is set to 1/1320 of the rotor revolution period based on time-step studies [38] which determined that 60 time-steps per period for the highest frequency of interest (the blade-passing frequency) are required for acoustic propagation. The 60 time-steps per period criterion is also cited in the literature [39] as the appropriate value to use for 2nd-order time-accurate codes such as the one used in this work.

Recall from Section 3.2 that the details of the input perturbation waveform are less important than its sawtooth-like character, because perturbing the relative supersonic

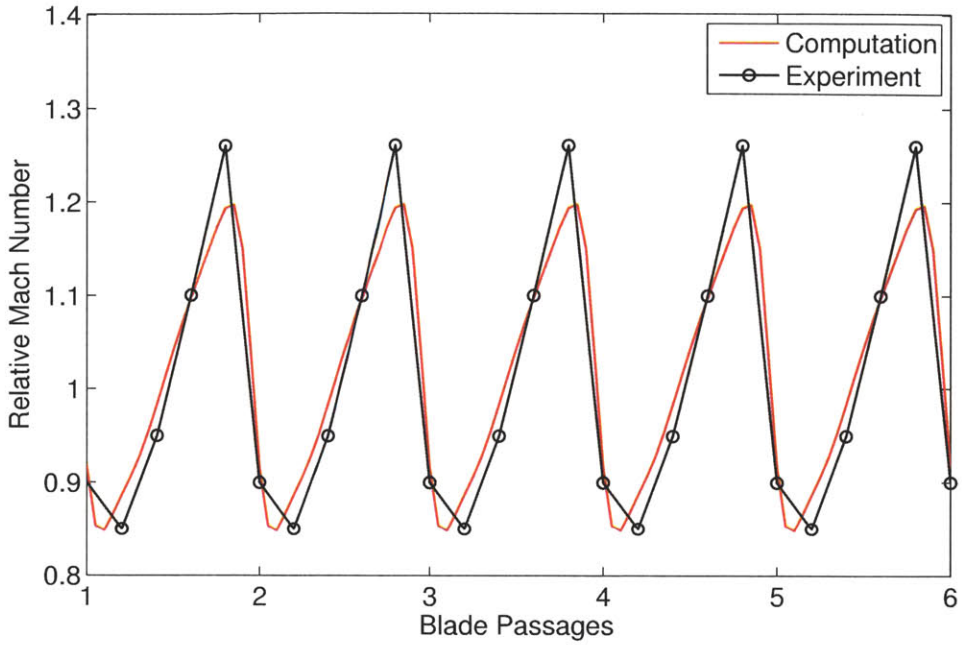

Figure 4-6: Average passage relative Mach number distributions. Mean relative Mach number: 1.02.

flow in any way requires the generation of shocks and expansion fans in order to turn the flow. The lower, rounded peaks are due to the grid resolution used in the computation (25 circumferential grid points per passage[1]), which is insufficient to resolve the higher spatial harmonics which give rise to the sharp peaks in the experimentally measured flow field. Since the acoustic analysis herein focuses only on frequencies up to and including the blade-passing frequency, the inability of the grid (using the chosen resolution) to resolve the very short length scales is acceptable. The reduced shock Mach number leads to an under-estimation of the shockwave dissipation by approximately 45%. However, since the shocks merge with expansion fans as they propagate, this effect is confined to the region just upstream of the rotor and therefore the global effect of the under-estimation of the shock dissipation is expected to be small.

To assess the impact of the blade-to-blade stagger angle variations on the relative

[1]Grid studies found that 25 points per wavelength is the minimum required wave resolution for successful acoustic propagation; this is in agreement with the literature [40, 41] for 2nd-order finite volume codes.

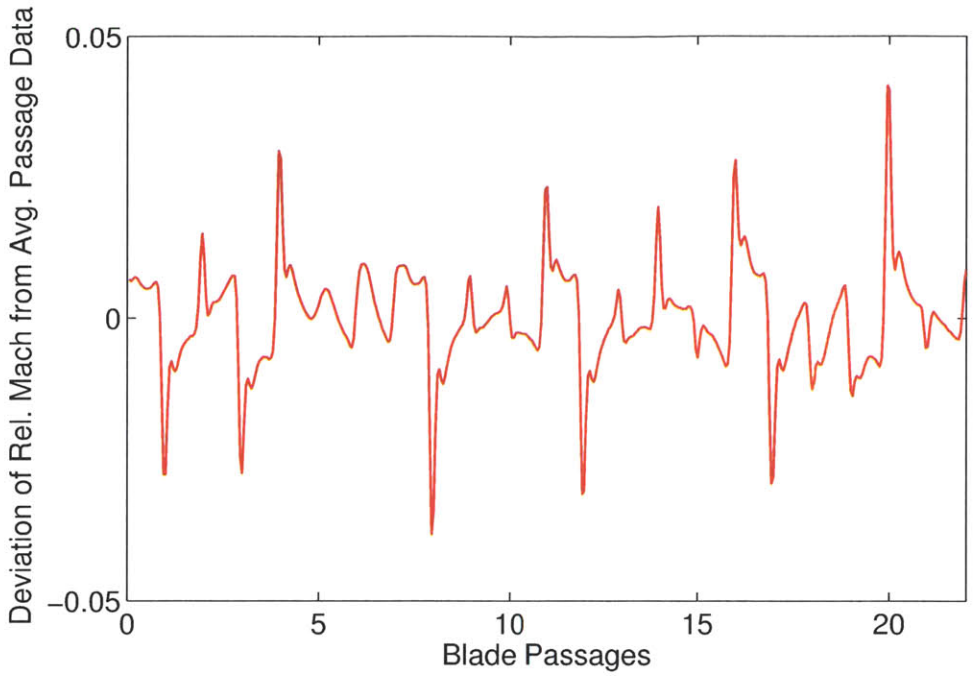

Figure 4-7: Deviation in relative Mach number distribution over blade passages compared to average passage data (full wheel body force calculation).

Mach number field, the deviations from the average passage data are computed. This is shown in Figure 4-7, revealing the non-uniformities which lead to MPT noise. Using this non-uniform shock structure, unsteady computations are carried out for a total of 14 rotor revolutions to assess the in-duct mode propagation and far-field noise signature. Acoustic data is recorded only for the final 2 revolutions after ensuring that all transients are settled. The time required for acoustic waves to propagate from the fan leading edge to the Ffowcs-Williams and Hawkings integration surface is approximately 1.2 rotor revolutions, so the time duration of the unsteady computation is sufficient that the unsteady flow field is indeed periodic in time.

4.5 Far-Field Propagation

The new methodology is also assessed in its ability to predict the far-field noise levels up to and including the blade-passing frequency, providing an overall indication of the accuracy of the approach. The ability of the numerical solver to successfully propagate

the acoustics to the far-field is critical to the utility of the body force approach as a noise prediction tool. The steady-flow streamlines in Figure 4-8 have only small curvature at the FW-H surface, indicating that the integration surface is adequately located in the forward arc, capturing important flow non-uniformities inside the region enclosed by the FW-H surface. To quantify, recall from Section 3.4 that the average pressure coefficient on the FW-H surface is less than 1% of the inlet plane pressure coefficient. In the experiments with the conventional inlet, a barrier wall was used to prevent fan exhaust noise from contaminating the far-field measurements [18]. For the computation, the fan exhaust is ducted out of the domain without mixing with the external flow to accomplish the same effect.

Figure 4-9 shows spectra at various receiver locations, specified by emission angle Θ_{em}, for both the computation and the experimental data. The receiver locations lie on a line parallel to the fan axis at a distance of 4 fan diameters, as depicted in Figure 3-17. This is consistent with the experimental setup. The specific frequencies at which MPTs occur are not expected to match between the computed and measured results since the fan blade stagger angle distributions in the experiments are not known. The overall agreement, particularly at the blade-passing frequency for $\Theta_{em} \leq 65°$, suggests that the scheme accounting for numerical attenuation is correctly compensating for the inherent solver decay. At the blade-passing frequency, the RMS error is 8 dB over $25° \leq \Theta_{em} \leq 65°$, indicating fair agreement. The elevated noise floor levels in the experimental data below 5 times the shaft frequency are characteristic of the anechoic performance limitations of an aeroacoustic wind tunnel.

At emission angles greater than 70° some discrepancies are observed with RMS errors up to 29 dB at the BPF. This is suggested to be due to the fact that the downstream FW-H integration surface is located too close to the inlet lip. In addition, creeping rays might not be accurately captured due to the lack of a boundary layer on the nacelle, reducing noise levels in the computation for observers on the aft arc. Another potential source of error in the comparison might be due to differences in the flow field between the computation and experiment. In the experiments, the installation of the nacelle in the wind tunnel (see Figure 3-4) resulted in the walls

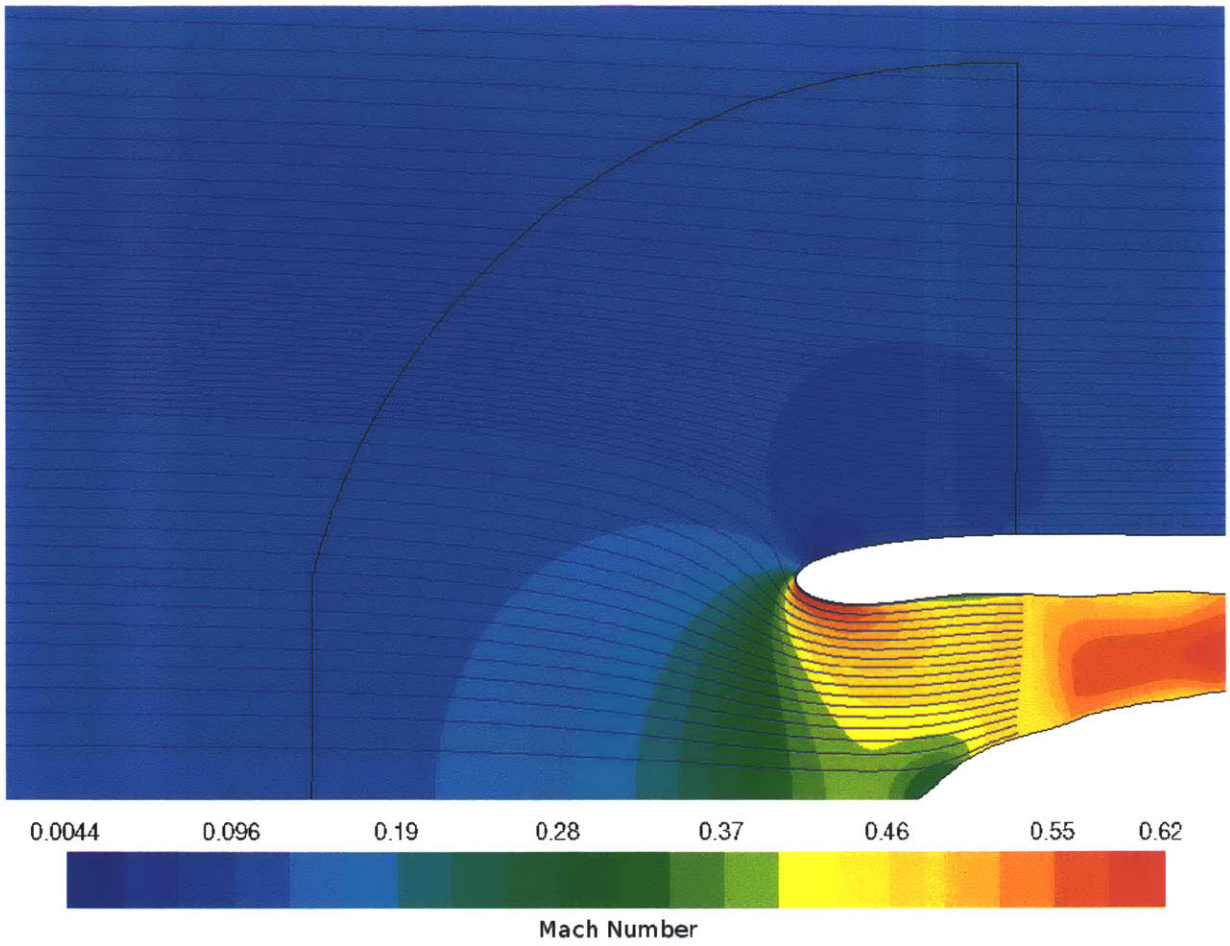

Figure 4-8: Contours of Mach number (time-mean body force calculation) with streamlines for the NASA/GE R4 fan rotor (FW-H integration surface: black outline).

being sufficiently close to the inlet that the near-field flow is affected, altering the acoustic signature compared to the unbounded flow used in the computation in order to mimic the free-field acoustic conditions from the experiments. This effect would be most pronounced for emission angles $70° < \Theta_{em} < 110°$ as the walls are closest to the nacelle over this range. Improvements in the aft arc are possible if the FW-H surface were to be repositioned. However, the agreement for the emission angle range $25° \leq \Theta_{em} \leq 65°$ is sufficient for evaluating the relative effects of serpentine inlet geometries on changes in MPT noise.

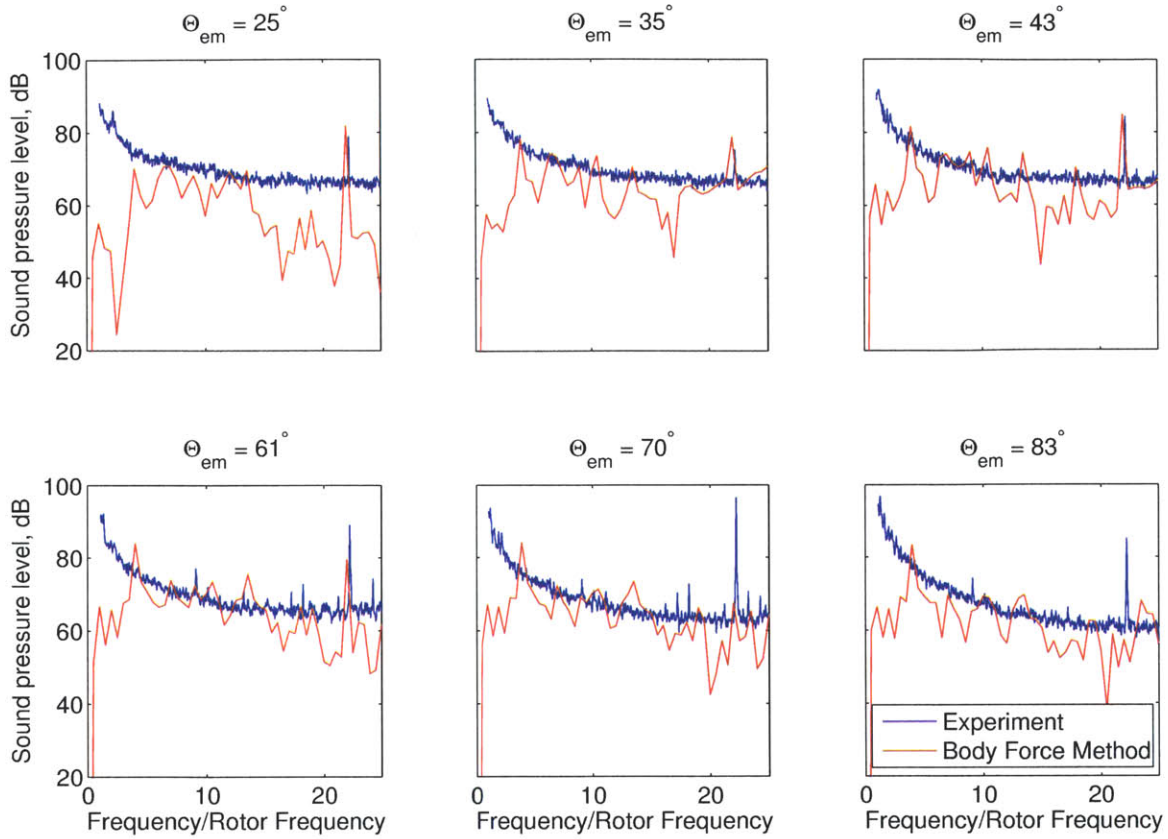

Figure 4-9: Comparison of spectra at various emission angles.

4.6 In-Duct Propagation

Analysis of the in-duct modes is conducted to gain insight into the mechanisms by which the modal content changes as the waves propagate upstream in the inlet for the axisymmetric validation case. MPT noise arises from the coalescence of the passage shocks into a once-per-revolution periodic pressure field. Additional physical insight into the mechanism responsible for this behavior is sought in order to be able to later assess how boundary layer ingestion alters it. A qualitative analysis is first conducted to investigate the effect of non-uniform shocks on the wavenumber vector distribution to assist in interpreting the simulation results. Redistribution of acoustic energy from high-order to low-order circumferential modes is observed in the computational results, consistent with the qualitative analysis described in the following paragraph.

It is hypothesized that the non-uniform shock structure near the fan leading edge results in acoustic energy redistribution as the acoustic waves travel upstream. This is because the wavefronts associated with the fan blades have wavenumber vectors $\vec{k}$ oriented differently depending on the blade stagger angle. Thus, acoustic energy can accumulate in certain preferred circumferential modes, which will be lower-order than the blade-passing modes at which most of the acoustic energy is introduced. The flow field and unsteady pressure field from the conventional inlet computation is first examined qualitatively in order to assess this hypothesis describing the mechanism leading to MPT noise.

Returning to the time-mean Mach number contours shown in Figure 4-8, regions of local acceleration are observed near the nacelle lip which can have an attenuating effect on the acoustic waves traveling upstream [22]. To illustrate that the acoustic field is not periodic over the blade pitch, contours of unsteady pressure normalized by the mean throat dynamic pressure are shown on planar cuts through the rotor one pitch apart in Figure 4-10. The coordinates are normalized by the throat radius R. Prasad and Feng [22] report similar contours from their calculation on a fan with identical-blades. In comparison, low-frequency (longer wavelength) MPT noise is seen in the current results and the shocks are neither uniform in spacing nor in strength.

To describe the redistribution of acoustic energy within the duct, the acoustic pressure field at several cross-sections of the inlet duct, shown in Figure 4-11, are analyzed. The redistribution of energy from high-order to low-order circumferential modes is observed (alongside the overall decay), consistent with the hypothesis that a non-uniform shock distribution leads to the accumulation of acoustic energy in low-order modes. This can also be seen in the spatial Fourier decomposition depicted in Figure 4-12. The effect of the overall decay in the unsteady pressure has been removed by normalizing the unsteady pressure amplitudes by the blade-passing order amplitude. This emphasizes the enhanced propagation characteristics for spatial orders lower than one-half of the blade-passing order.

While comparing the modal content at the blade-passing frequency should allow the accuracy of the in-duct propagation to be assessed, the experimental results con-

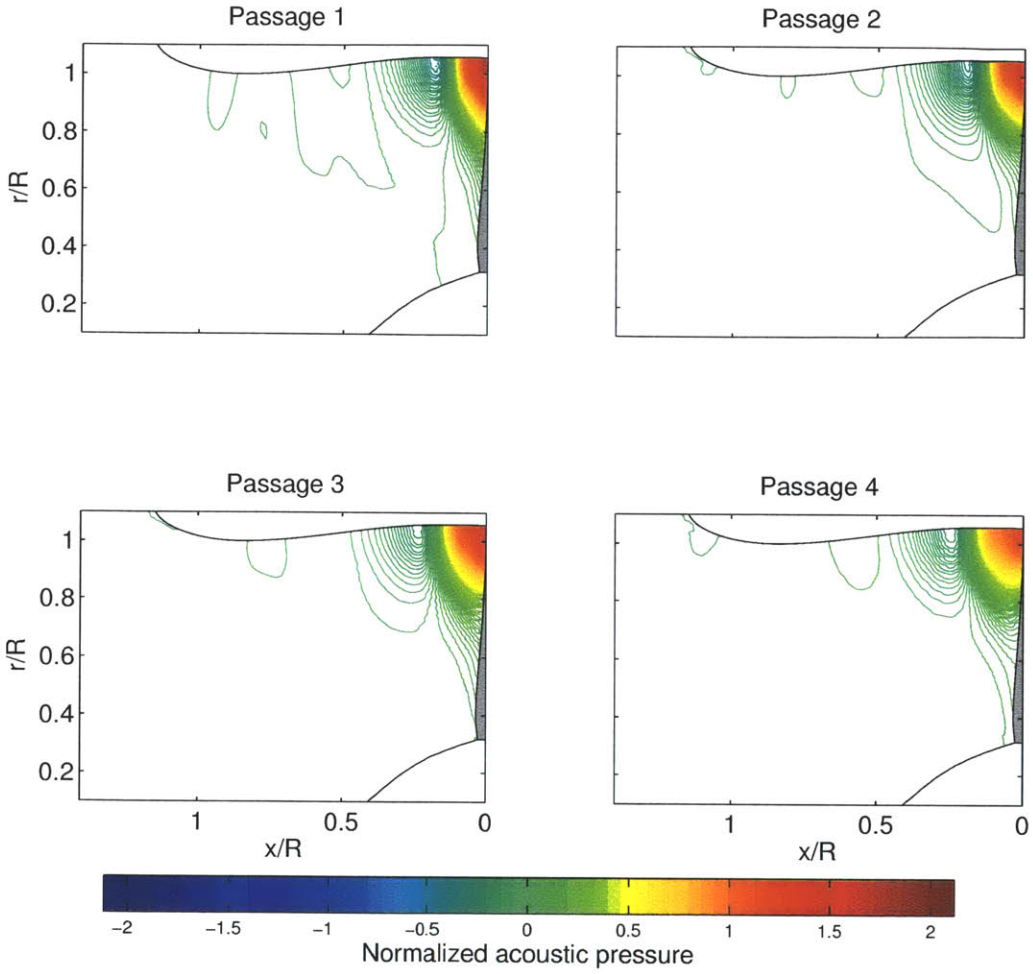

Figure 4-10: Unsteady pressure (normalized by average throat dynamic pressure) for fan passages one blade pitch apart.

tain a nearly uniform modal energy distribution which appears to be noisy as a result of the rotating rake measurement system used [18, 42]. This prevents a quantitative comparison from being made.

An alternative method of evaluating the in-duct propagation characteristics is therefore adopted. At the casing, the acoustic duct transfer function is determined using Ljung's system identification method [43] and its characteristics are analyzed. The multi-input, multi-output (MIMO) linear transfer function has inputs and outputs corresponding to circumferential mode amplitudes, m_i and m_o respectively. The input location is the fan leading edge and the output location is the inlet throat. Ide-

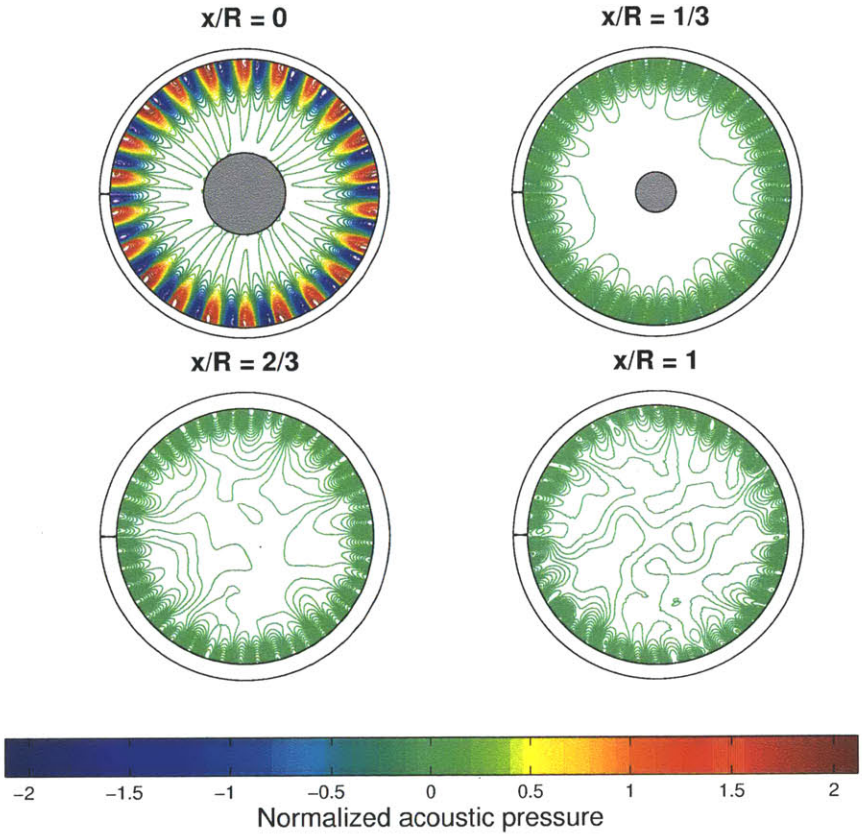

Figure 4-11: Unsteady pressure (normalized by average throat dynamic pressure) in duct cross-sections.

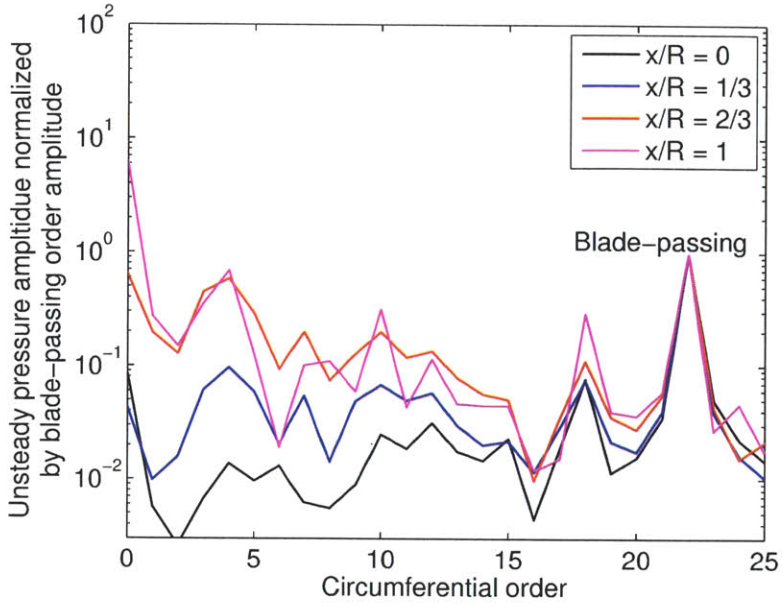

Figure 4-12: Spatial Fourier decomposition of unsteady pressure at the casing normalized by the blade-passing order amplitude.

ally, when performing a forced response analysis and system identification, a frequency sweep over the inputs is performed. In the case here, the input is naturally restricted to the pressure field generated by the body forces representing the rotor. With this the coherence of the transfer function estimate is expected to be low ($\gamma^2_{yu} < 0.6$) over most frequencies. The coherence is a measure of the correlation between input and output of a dynamic system:

$$\gamma^2_{yu}(j\omega) \equiv \frac{|\Phi_{yu}(j\omega)|^2}{\Phi_{uu}(j\omega)\Phi_{yy}(j\omega)} \tag{4.2}$$

where Φ_{yu} is the cross-spectrum between the input and output signals and Φ_{uu} and Φ_{yy} are the auto-spectra.

The coherence of the elements on the main diagonal of the transfer function matrix is generally low everywhere except at BPF (where $f/f_{shaft} = 22$) and higher harmonics, as shown in Figure 4-13. The off-diagonal elements exhibit different behavior, displaying coherence peaks at not only BPF and higher harmonics but also at other multiples of shaft frequency. As an example, for $m_i = 22$, Figure 4-14 shows

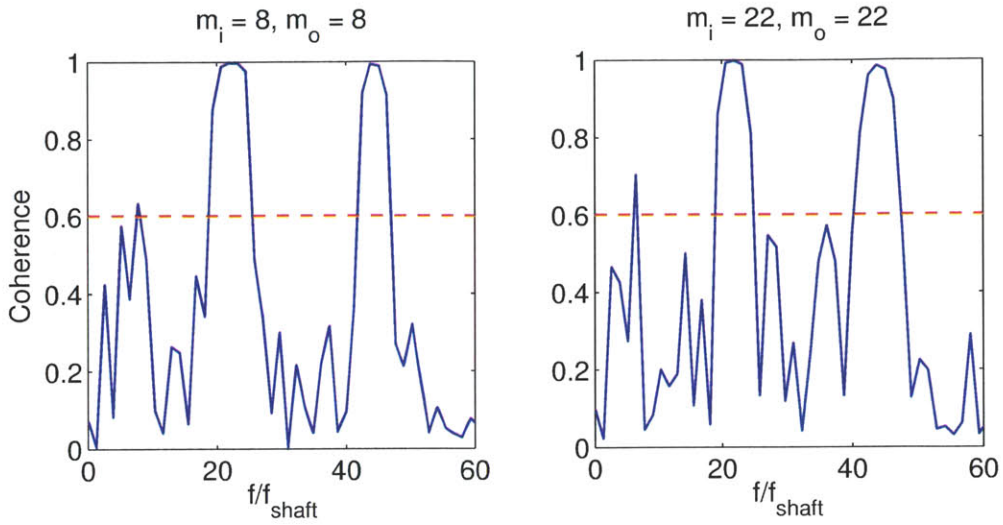

Figure 4-13: Coherence vs. frequency: diagonal elements of acoustic transfer function, showing high coherence at the blade-passing tone.

a rotating mode near 15 times shaft frequency for $m_o = +7$ (coherence of ~ 0.8 for $m_o > 0$ and coherence < 0.6 for $m_o < 0$) and near 30 and 38 times shaft frequency for $m_o = -7$. The rotating modes at frequencies other than BPF and higher harmonics carry the energy of the multiple-pure tones. Figure 4-15 depicts a stationary mode near 14 times shaft frequency for $m_i = 22$, $m_o = \pm 4$. The stationary modes indicate the presence of excited natural duct modes. Similarly amplified modes are found at $m_o = \pm 12$ and ± 20.

These results indicate that, due to shock wave interaction, the acoustic energy is redistributed to lower-order circumferential modes, consistent with the contours of acoustic pressure in Figure 4-11. This might also suggest that unsteady pressure originating in cut-off modes can possibly transfer to cut-on modes and propagate out of the inlet duct. For boundary-layer ingesting serpentine inlets, taking care to avoid such effects might offer a strategy to mitigate noise radiation from the duct.

4.7 Conclusions from the Model Assessment

In this chapter, the ability of the body-force-based fan model to produce the rotor pressure rise and flow turning as well as to generate the non-uniform shocks which

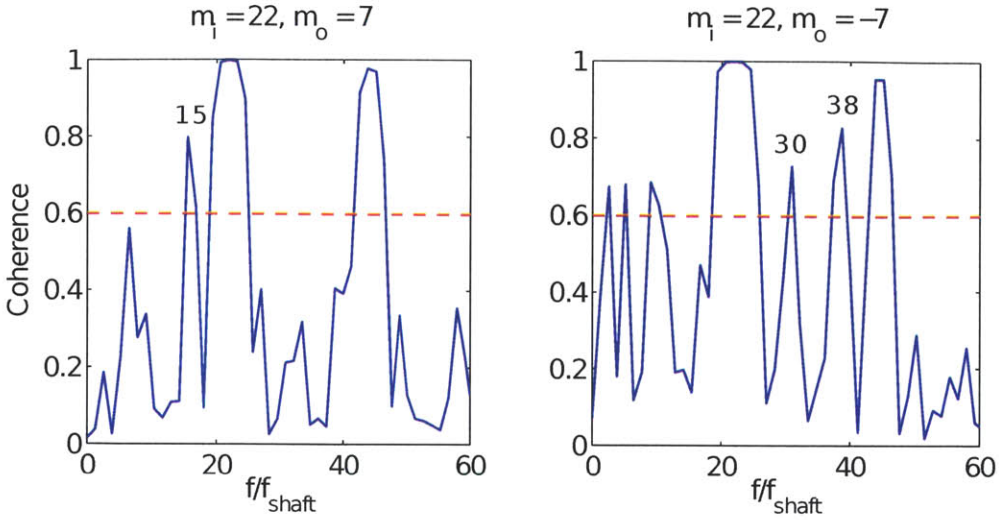

Figure 4-14: Coherence vs. frequency: off-diagonal elements with rotating modes, showing MPT generation.

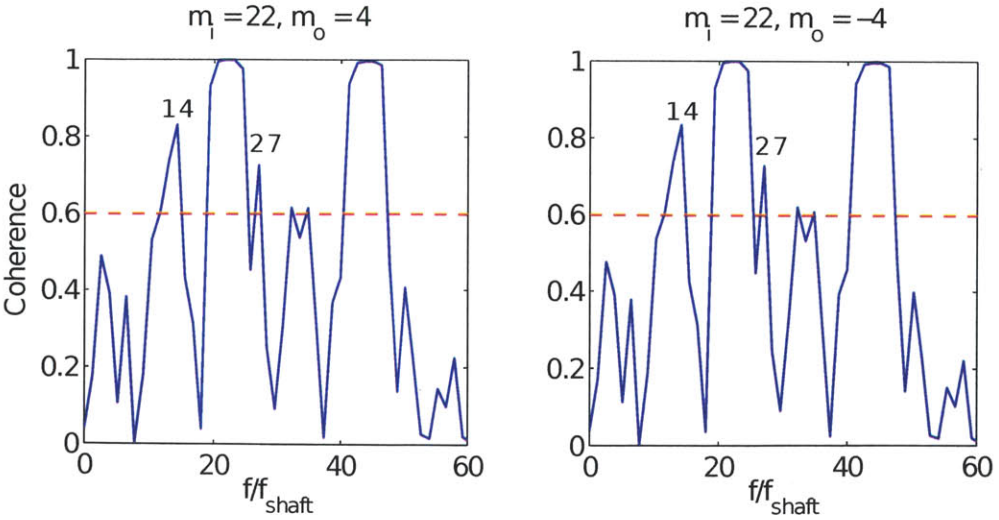

Figure 4-15: Coherence vs. frequency: off-diagonal elements with stationary modes, showing the excitation of natural duct modes.

give rise to MPT noise was assessed. The overall rotor blade row performance is well-captured by the body force approach. Agreement in the near-field relative Mach number distribution between the experimental data and the computation indicates that the body-force-based method can generate the rotor-locked shock structure necessary to produce MPT noise. Over the emission angle range of $25° \leq \Theta_{em} \leq 65°$, where results are not subject to discrepancies in the setup between experiment and computation or proximity of the FW-H surface, the RMS error in SPL at the blade-passing frequency is 8 dB. This suggests that source generation and noise propagation are adequately captured in the computation. Examining the coherence of duct acoustic transfer function estimates indicates that the interaction of the non-uniform shocks can cause a shift in acoustic energy from high- to low-order circumferential modes. From these results, the body force method is deemed suitable to assess the effects of inlet distortion noise, on a relative basis, for serpentine inlet configurations.

Chapter 5

Effects of Inlet Flow Distortion on Rotor-Alone Tone Generation and Noise Propagation

To make an initial assessment of the effects of boundary layer ingestion and the use of serpentine inlets on the generation and propagation of rotor-alone tones, a computation was carried out using the serpentine inlet and airframe surface from the Silent Aircraft Initiative SAX-40 [6]. The outcomes assisted in scoping a detailed investigation to quantify the dependence of rotor-alone tones on serpentine inlet characteristics and to determine the mechanisms leading to these dependencies. The results obtained are compared to the conventional inlet results presented in the previous chapter.

The main objectives of this chapter are (1) to quantify the effect of inlet swirl distortion on the generation and propagation of multiple-pure-tone noise in serpentine inlet systems relative to uniform inflow conditions, and (2) to characterize the underlying mechanisms responsible for the changes in source noise and the noise radiating from the inlet system. It will be shown that the source noise sound power is increased by as much as 38 dB due to the swirling inflow at the fan face while on average the overall A-weighted sound pressure level (OASPL) in the far-field is only increased by 3 dBA for the SAX-40 inlet. The detailed interpretation and interrogation of these results are the objectives of this chapter. It is conjectured that the local

shock strength is increased in regions of counter-swirl, while the sound power decay is enhanced in regions of subsonic relative Mach number induced by the streamwise vortex rotating in the same direction as the fan. The far-field spectra show that the tones above one-half of the blade-passing frequency, including BPF tones, appear to be cut-off with inlet distortion and that acoustic energy is redistributed and increased at frequencies below one-half BPF.

This chapter addresses the following questions:

- What is the impact of inlet swirl distortion on MPT noise generation?
- How does the non-uniform flow in the serpentine inlet duct affect far-field noise?
- Are the effects of non-uniform flow on source noise dominant relative to its effects on acoustic propagation?

5.1 Nacelle and Fan Geometry Definitions

In this chapter, the body force approach is implemented for the serpentine inlet for the SAX-40's integrated propulsion system with boundary layer ingestion and compared with the conventional axisymmetric inlet used in Chapter 4. The same fan blade stagger angle variation is employed for both cases. Both inlets are coupled to the NASA/GE R4 fan rotor.

The downstream end of the serpentine inlet is coupled to the conventional inlet at the location where its diameter is at a minimum. This location is referred to as the Aerodynamic Interface Plane (AIP). For both computations, a rotor-alone configuration is modeled at the cut-back operating point corrected flow. The serpentine inlet was designed for boundary layer ingestion and has an offset ratio of $OR = \delta/D = 0.52$, an upstream-to-downstream area ratio of $AR = A_{AIP}/A_{throat} = 1.03$, and a length-to-diameter ratio of $L/D = 2.0$. The aerodynamic performance and geometric details for this inlet can be found in Ref. [24]. In both the conventional and serpentine inlet cases, the fan exhaust is ducted out of the computational domain to prevent fan exhaust noise from contributing to the far-field noise levels.

5.2 Computational Setup

The computational domain for the serpentine inlet case includes the rotor region, the upstream duct and inlet, and the external flow field as shown in Figure 5-1. While the conventional inlet is exposed to free stream conditions, the aircraft suction surface and boundary layer are included in the serpentine inlet calculation. The suction surface boundary layer and related stagnation pressure deficit are defined 10 diameters upstream of the inlet using previously conducted viscous 3-D airframe computations [36], resulting in a stagnation pressure distortion at the AIP as shown in the inset in Figure 5-1.

The inherent dissipation present in the inviscid solver used is compensated for in the far-field acoustic results for both cases. The FW-H surface is placed approximately 1.5 fan diameters from the inlet throat in both computations. The serpentine inlet domain contains approximately 16 million cells in a structured grid topology. The serpentine inlet increases the number of cells needed for the internal flow but the presence of the airframe effectively halves the size of the external domain. The net result is a slight decrease in cell count relative to the 17 million needed for the conventional inlet. Variation in cells sizes in the rotor region, inlet duct and in the near-field region up to the FW-H surface are minimized to reduce numerical dispersion. Acoustic buffer zones are placed outside the FW-H surface and in the duct far downstream of the rotor to prevent spurious wave reflections. The buffer zone formulation uses grid stretching and explicit damping as discussed in Section 3.7. The stagnation pressure (including the airframe boundary layer stagnation pressure deficit) and the free-stream flow direction are prescribed at the upstream boundary of the domain. At the downstream boundary in the external flow domain the static pressure is set in order to determine the free-stream Mach number of 0.1[1]. For the internal flow, the static pressure at the boundary downstream of the rotor is adjusted to set the corrected flow through the inlet to the desired model-scale cut-back value of 38.0 kg/s. The time-step size for both computations is the same. In both

[1]Though the cut-back Mach number for the SAX-40 is 0.22, the free-stream Mach number of 0.1 is consistent with the experimental R4 wind tunnel data and is thus used throughout this work.

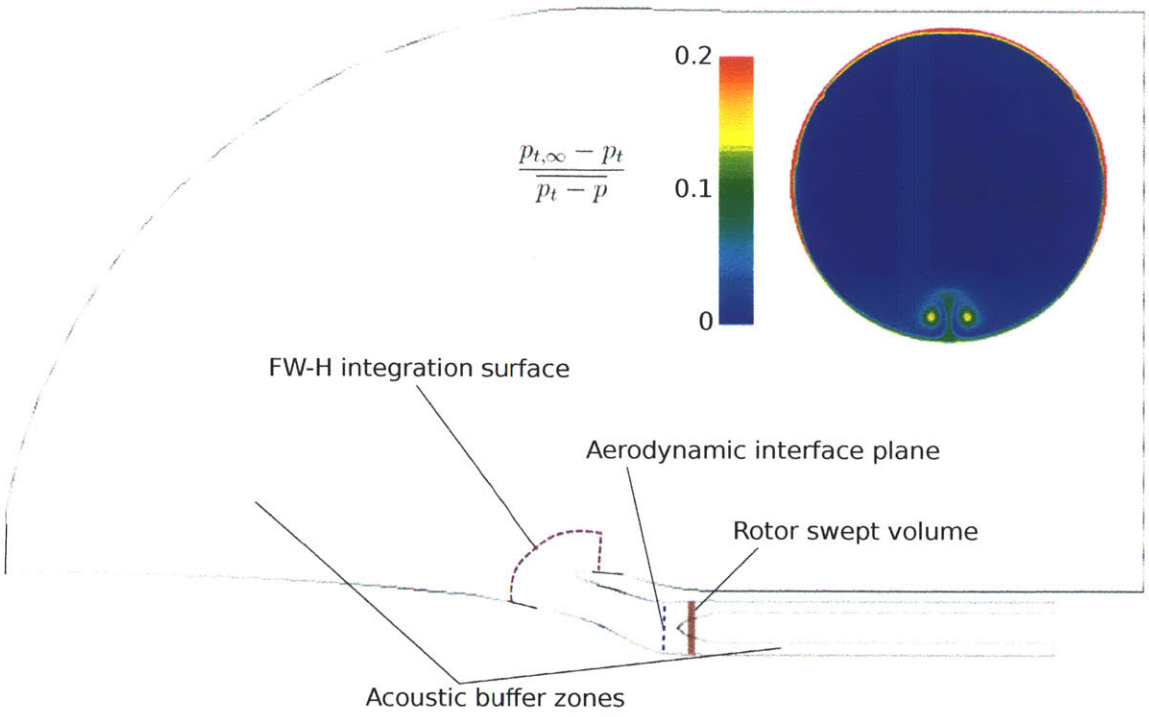

Figure 5-1: Computational domain for serpentine inlet case. Inset: non-dimensional stagnation pressure field at aerodynamic interface plane.

computations, the same far-field measurement locations relative to the fan are used.

The unsteady computations are initialized from steady calculations and carried out until two rotor revolutions of periodic acoustic data are recorded at all receiver locations. This ensures sufficient resolution in the frequency domain to identify tones down to shaft order in the far-field spectra. The approximate time required for the acoustic waves generated at the fan to reach the FW-H surface is 2.5 rotor revolutions for the serpentine inlet case. The increase over the 1.2 revolutions required for the conventional inlet is due to the presence of the extended inlet duct, which lengthens the acoustic propagation path length.

Table 5.1: In-Duct Sound Power Levels.

PWL (dB)	Serpentine Inlet	Conventional Inlet	Change
Fan face	167	129	38
AIP	133	97	36
Attenuation	34	32	2

5.3 Aerodynamic and Aeroacoustic Results

The key in-duct acoustic results are summarized in Table 5.1. The sound power level is computed up to the blade passing frequency based on the cut-on ratio of cylindrical duct modes determined assuming uniform mean flow. The solver-decay correction has been applied to the results. The interaction of the inlet distortion and non-uniform flow through the serpentine inlet duct with the fan rotor increases the source noise by 38 dB in sound power (as opposed to sound pressure) relative to the conventional inlet case at the same fan operating conditions. However, there is enhanced sound power attenuation of 2 dB through the non-uniform flow from the fan to the aerodynamic interface plane (AIP) for the serpentine inlet case. The AIP corresponds to the inlet throat for the conventional inlet and for the serpentine inlet it is the farthest upstream location where the cross-section is circular. There is also a redistribution of acoustic energy to frequencies below 11 times shaft frequency. In particular the BPF tone and MPTs above 11 times shaft frequency appear to be cut-off leading to an increase in far-field overall sound pressure level of only 7 dB or 3 dBA.

The striking contrast between the 38 dB increase in the source power and the comparatively minor 7 dB increase in far-field SPL is investigated in this section. In addition, to address the earlier stated objectives in light of these results, the in-duct aerodynamics, the rotor-alone noise and the noise propagation to far-field observers are analyzed. Furthermore, the aeroacoustic features of the conventional inlet with axisymmetric flow conditions are compared with the serpentine inlet to highlight important differences.

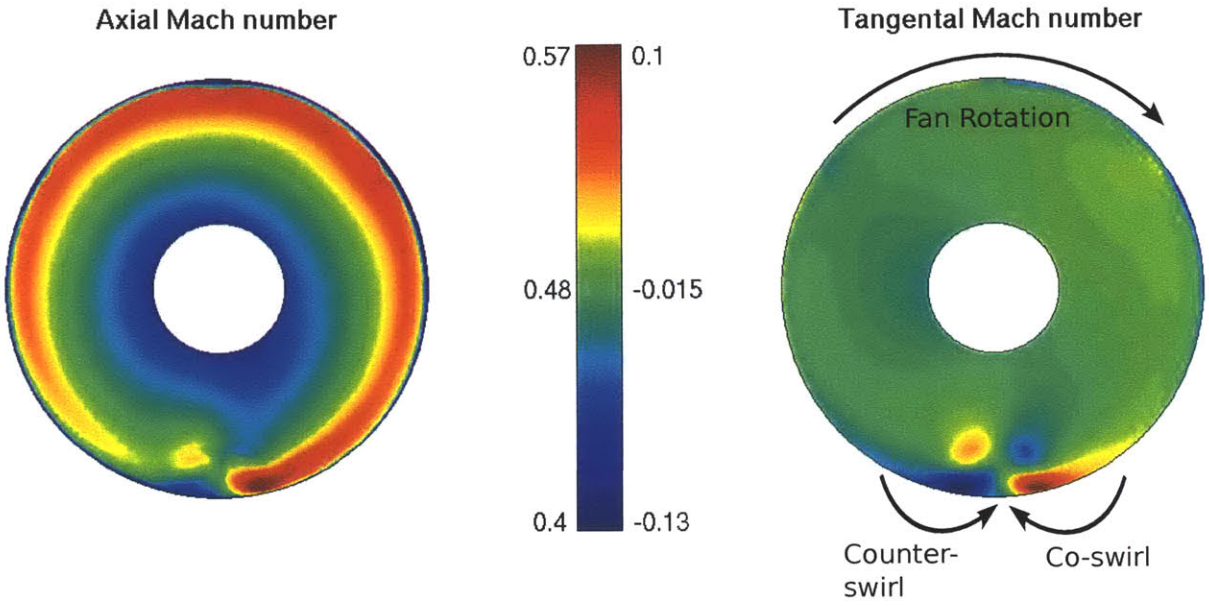

Figure 5-2: Axial and tangential Mach number distributions at rotor leading edge for serpentine inlet.

5.3.1 Inlet Distortion Characteristics

The ingestion of the airframe suction surface boundary layer at the free-stream Mach number of 0.1 results in a mass-averaged stagnation pressure deficit of 15% of the inlet dynamic pressure based on the distortion pattern at the AIP, shown in the inset of Figure 5-1. While the pressure recovery is higher at low flight Mach number, the general flow features are in agreement with those obtained by Madani and Hynes for the same inlet at cruise conditions [24]. In particular, the ingested airframe boundary layer and secondary flow effects lead to a pair of streamwise vortices inducing regions of co- and counter-swirl as depicted in Figure 5-2 on the right. The asymmetry in the axial Mach number visible on the left side of Figure 5-2 is due to the effects of the ingested streamwise vortices on the pressure field. It will be shown that the streamwise circulation associated with these vortices strongly affects the rotor blade shock generation and propagation as they alter the rotor inlet relative Mach number distribution.

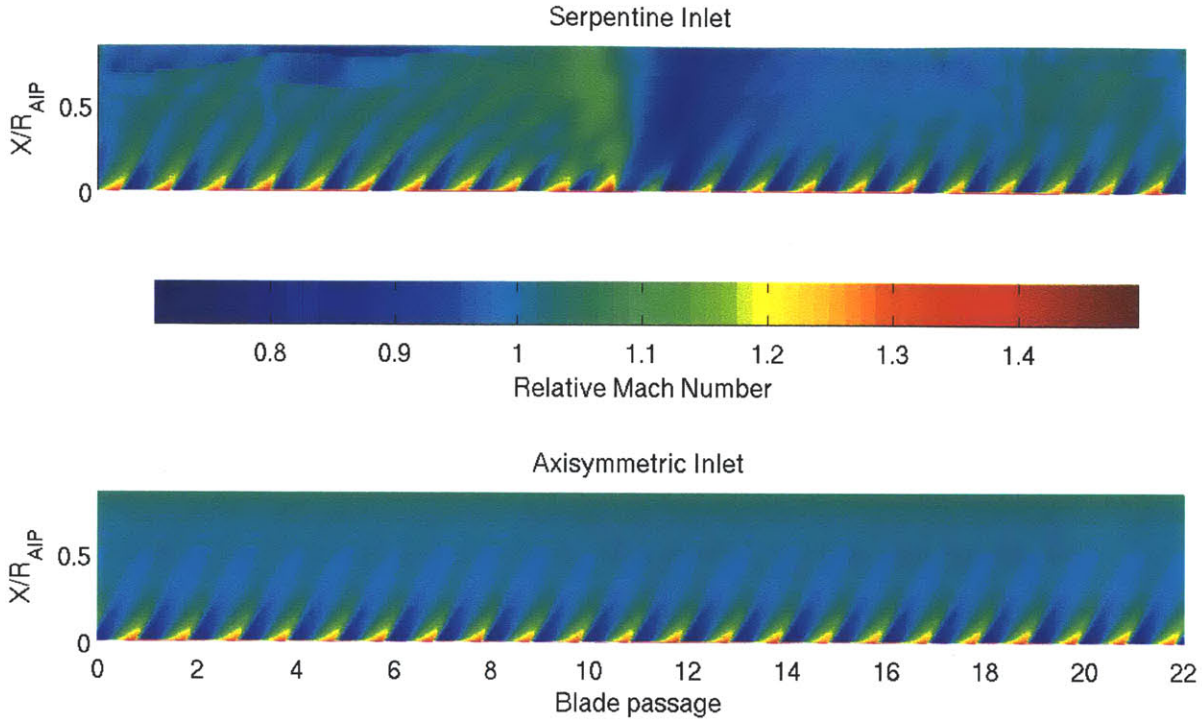

Figure 5-3: Relative Mach number at 92% span from fan ($x/R_{AIP} = 0$) to AIP/throat ($x/R_{AIP} = 0.84$), showing the impact of inlet distortion on shock generation and propagation.

5.3.2 Inlet Distortion Effect on Shock and MPT Noise Generation

The blade shock strength is governed by the incoming relative Mach number and relative inlet flow angle which can be perturbed by stagger angle changes and, more dominantly, inlet flow distortion. An unwrapped view of the instantaneous relative Mach number field at 92% span is depicted in Figure 5-3 for both the conventional and the serpentine inlet computations, extending from the fan leading edge to the AIP.

In the bottom plot small variations in shock strength and angle can be observed due to the blade-to-blade variations in stagger angle. This is the source of MPT noise in undistorted inlet flow. The maximum variation in peak relative Mach num-

ber at the fan leading edge due to the stagger angle variations is 0.04. With inlet distortion present in the top plot, regions with co- and counter-swirl result in relative Mach number variations of as much as 0.32, approximately 8 times larger than the variation due to stagger angle alone. Furthermore, the region of co-swirl leads to subsonic relative Mach numbers (dark blue region) whereas counter-swirl increases the supersonic relative Mach number (yellow region) which yields stronger shocks. This is also manifested in the angle changes of the wavefronts or the corresponding perpendicular wavenumber vectors: wavefronts inclined further away from the axial direction correspond to increased wave propagation rates while those angled closer to axial propagate at reduced rates, becoming evanescent in the limit of a purely tangential wavenumber vector.

The consequence of these changes in the incoming flow is an increase in fan sound power level of 38 dB for the serpentine inlet compared to the conventional inlet case. The underlying mechanisms and wave propagation behavior are investigated further in Section 5.4.

5.3.3 In-Duct Noise Propagation

To investigate the changes in the acoustic field between the fan face and the AIP, contours of instantaneous unsteady pressure fluctuations are shown in Figures 5-4 and 5-5 for the rotor leading edge and AIP respectively. The pressure is non-dimensionalized by the dynamic pressure at the AIP.

In the conventional inlet case, similar lobed structures, one per blade passage, are visible at both locations near the outer radius. The sound power is attenuated by 32 dB from the fan face to the AIP. For the non-uniform inflow case, in addition to the increased sound pressure level, a qualitative change in the unsteady pressure field occurs during upstream propagation. Some of the high-circumferential-order modes have decayed at the AIP and the overall power has decreased by 34 dB. This is conjectured to be due to the presence of the subsonic relative flow region induced by the co-swirling streamwise vorticity since the subsonic relative flow should result

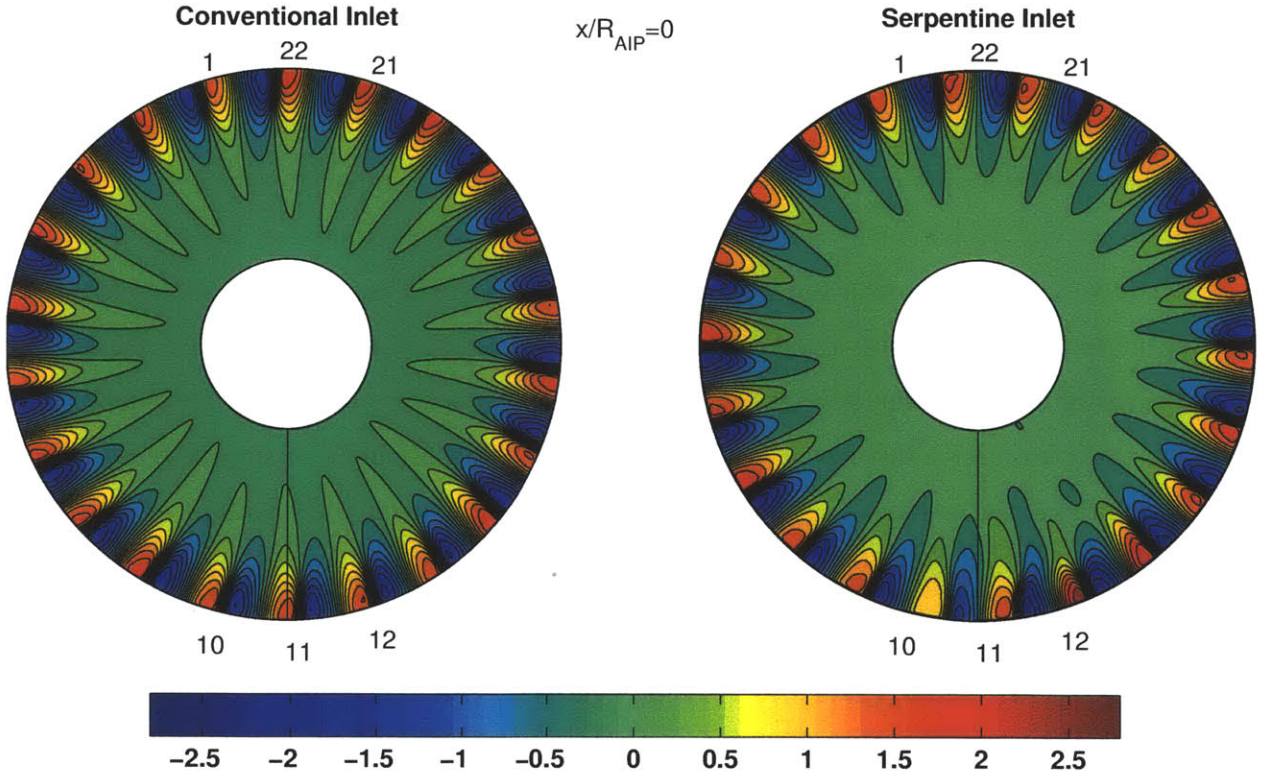

Figure 5-4: Instantaneous unsteady pressure at rotor leading edge normalized by mean dynamic pressure at AIP.

in locally evanescent wave behavior. Furthermore, the blade-passing circumferential mode is attenuated while a mode with circumferential extent of roughly 11 blade pitches is dominant. It should be pointed out that the streamwise vorticity due to boundary layer ingestion is concentrated over about $1/11^{th}$ of the circumference. This implies a connection between the inlet distortion and the duct acoustics, where unsteady pressure modes with spatial frequency equivalent to that of the distortion pattern are excited and scattered.

For the serpentine inlet, the duct extends further upstream from the AIP and Figure 5-6 depicts the unsteady pressure field at the inlet plane of the serpentine duct. High spatial harmonic modes have vanished and the unsteady pressure field is dominated by long-wavelength, low-frequency waves which remain cut-on. The decay from the AIP to the inlet plane is approximately 15 times less than that from the fan face to the AIP, although the streamwise distance is approximately 4 times longer. The decreased decay rate upstream is linked to the decreased wave amplitudes; shock dissipation mechanisms become less important as the waves attenuate. The short-wavelength pressure disturbances visible on the lower surface in the figure are related to the formation of streamwise vortices as the incoming boundary layer interacts with the inlet lip.

5.3.4 Far-Field Spectra and Overall Noise Levels

Figure 5-7 depicts the full-scale spectra for the conventional inlet (dashed lines) and serpentine inlet (solid lines) which reveals two striking results for the serpentine inlet case. First, frequencies greater than 11 times the shaft frequency, including the BPF, are absent, suggesting that they are cut-off in the inlet, and the tones are attenuated below the calculation's background noise floor[2]. This is consistent with the sound pressure field at the inlet plane shown in Figure 5-6. Analytically extending the conventional inlet duct to the same streamwise length as the serpentine inlet using the Mathews-Nagel model [20] results in only 0.5 dB of additional attenuation at the

[2]Fan broadband noise is not modeled in the simulations and the background noise floor is therefore set by numerical noise.

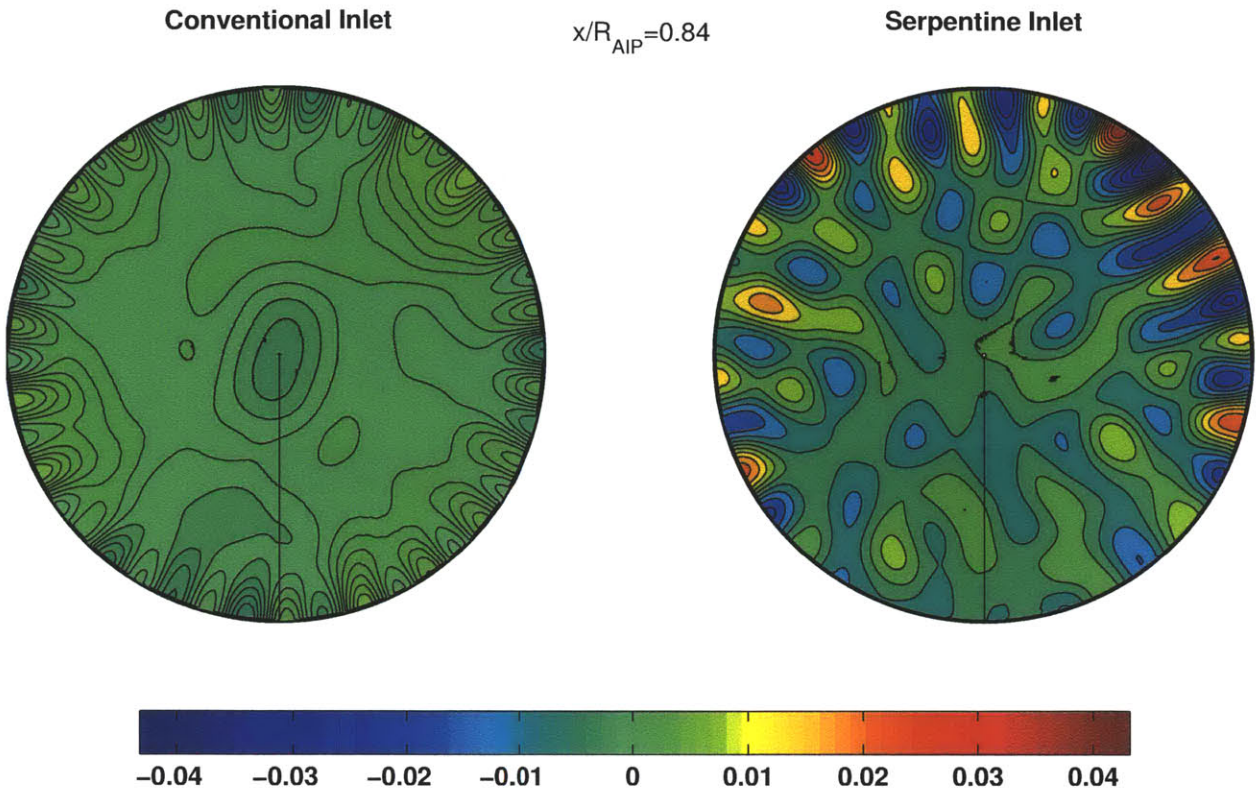

Figure 5-5: Instantaneous unsteady pressure at AIP normalized by mean dynamic pressure at AIP, showing the decay of blade-pitch wavelengths due to swirl distortion.

blade-passing frequency. The changes observed in the far-field spectra are therefore due to the effects of inlet distortion and boundary layer ingestion on propagation and not simply the extension of the inlet duct. Second, the sound pressure level for frequencies less than 11 times shaft frequency are elevated due to the interaction of the inlet flow distortion with the fan rotor and the propagation of acoustic waves through non-uniform background flow.

The nature of the mechanism leading to the amplification of the low-frequency tones is investigated in the next section. While the average linear OASPL is 7 dB higher for the serpentine inlet, due to the concentration of acoustic energy at low frequencies, A-weighting the spectra results, on average, in only 3 dBA higher OASPL for the serpentine inlet case. The presence of the airframe acts as a reflecting surface (increasing sound pressure levels by 3 dB) and therefore the A-weighted sound

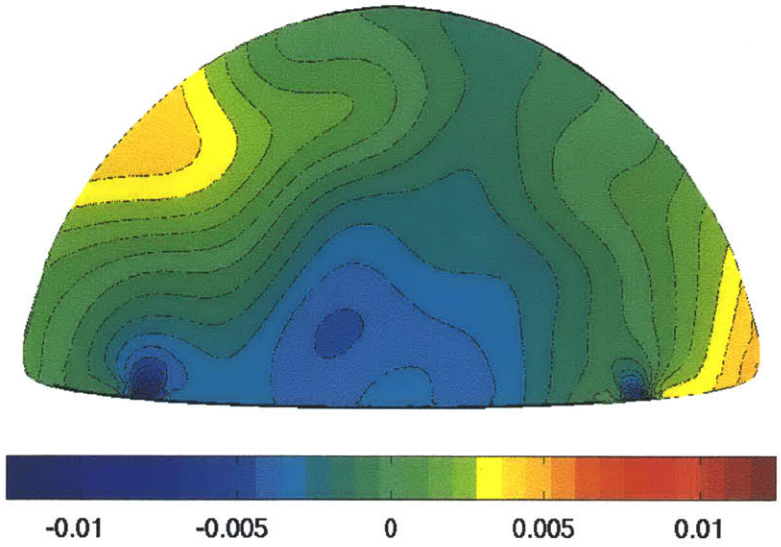

Figure 5-6: Instantaneous unsteady pressure at serpentine inlet plane normalized by mean dynamic pressure at AIP. The short-wavelength pressure disturbances on the lower surface indicate the location of the ingested streamwise vortices.

power propagated to the far-field is estimated to be similar for the two cases. The results suggest that, to reduce far-field noise, it may be possible to take advantage of the underlying mechanisms to redistribute the acoustic energy to low frequencies at which the human ear has reduced sensitivity. The results also illustrate that airframe shielding is critical for embedded propulsion system configurations, especially if the source noise is dramatically increased.

Finally, returning to Figure 5-3 and the observation made earlier that the inlet distortion is primarily confined to two blade pitches, or $1/11^{th}$ of the circumference, it is interesting to note that the tones in the far-field are absent at approximately 11 times shaft frequency and above. The next section explores how much of this effect is due to source noise changes from inlet distortion versus sound propagation through non-uniform flow.

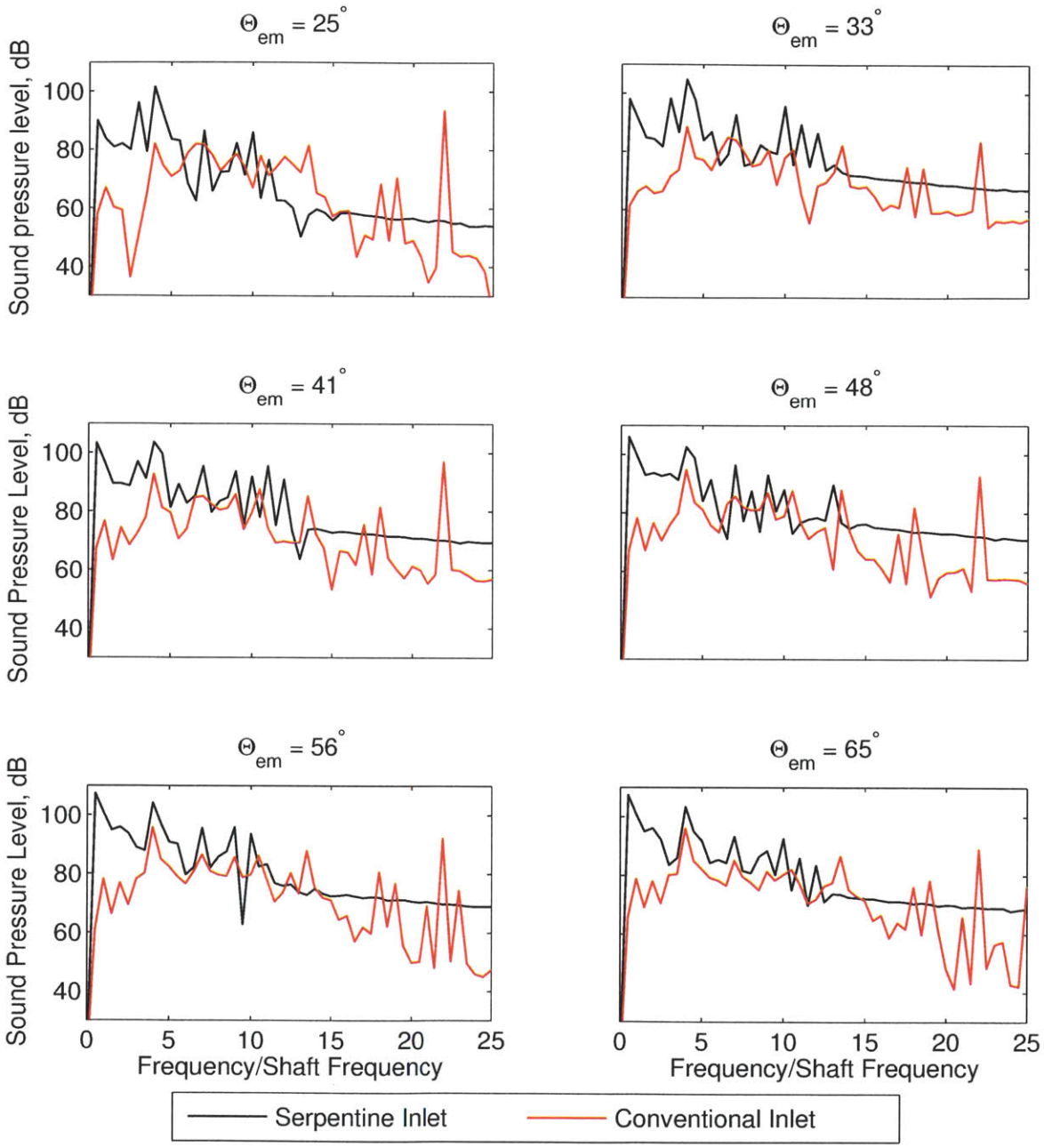

Figure 5-7: Full-scale linear far-field spectra, showing the amplification of low-frequency tones and the attenuation of high-frequency tones for the serpentine inlet case.

5.4 Analysis of Inlet Distortion Effects on Shock Strength and Linear Wave Propagation

In light of the results discussed above, a simplified model is used to illustrate the underlying mechanisms and links between inlet swirl distortion, increased shock strength and related MPT noise, and cut-off wave behavior. As discussed earlier, at the cutback fan operating condition considered here, the rotor blade tips experience supersonic inflow with detached shocks where the unchoked blade passage mass flow is governed by the rotor inlet relative Mach number M_1 and the relative inlet flow angle ξ_1. This is shown in Figure 5-8.

With inlet flow distortion present, the inlet relative Mach number and flow angle into the blade passages are perturbed, leading to variations in passage inflow conditions and thus shock strength and location. Even for identical blades, the spillage from one blade passage to another yields a non-axisymmetric shock distribution leading to multiple-pure-tone noise. While this complicated flow field and passage-to-passage interaction can only be captured in numerical simulations such as those conducted in this research, the simplified model described below is useful to guide the interrogation of the resulting shock strength variation. Assuming small perturbations, the evanescent and propagating wave behavior due to a non-axisymmetric modulation in shock strength can also be explained. The model is based on the control volume formulation by Freeman and Cumpsty [44] marked by the dashed line in Figure 5-8.

The underlying idea is that in the limit of infinitesimally small blade pitch (neglecting blade thickness and $B \to \infty$) the unchoked flow field in the blade tip region becomes axisymmetric with a circumferentially uniform shock surface[3] as sketched in the middle part of Figure 5-9. Conservation of mass, rothalpy, and momentum along the blade passage yield

[3]This is consistent with the assumptions used in the body force representation of axisymmetric through-flow for identical blade passages.

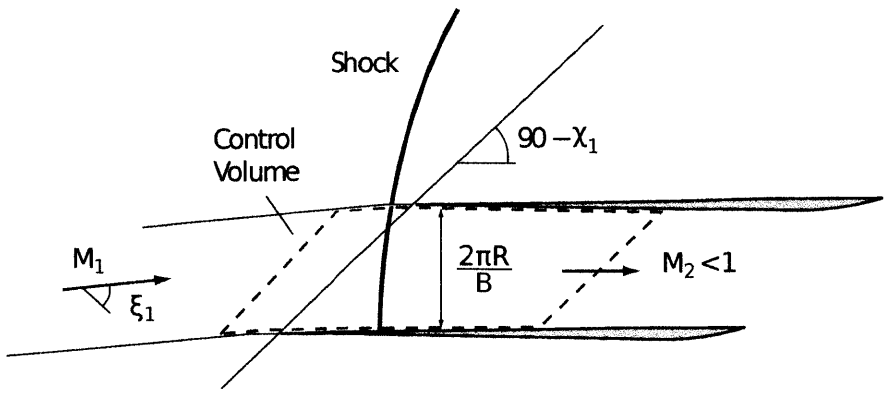

Figure 5-8: Control volume analysis for detached shock strength (adapted from Freeman and Cumpsty [44]).

$$\begin{aligned} \rho_1 u_1 \cos\xi_1 &= \rho_2 u_2 \cos\chi_1 \\ T_1\left(1+\frac{\gamma-1}{2}M_1^2\right) &= T_2\left(1+\frac{\gamma-1}{2}M_2^2\right) \\ p_1\cos\chi_1 + p_1\gamma M_1^2\cos\xi_1\cos\left(\chi_1-\xi_1\right) &= p_2\cos\chi_1 + p_2\gamma M_2^2\cos\chi_1 \end{aligned} \tag{5.1}$$

For given inflow conditions, M_1 and ξ_1, and blade leading edge camber angle, χ_1, the above set of equations can be solved for the downstream conditions and the shock surface static pressure ratio p_2/p_1 can be determined. For a fixed geometry, there are inflow conditions for which the above equations do not have a solution, indicating that the flow is choked.

Inlet flow distortion yields streamwise vortices which lead to co- and counter-swirl manifested in regions of subsonic and supersonic relative blade inlet Mach numbers in the outer span (see Figure 5-10). For the flow conditions investigated, the circumferential variation in relative inlet Mach number is dominant compared to the corresponding relative flow angle changes such that, using the above model, the shock surface strength depends predominantly on M_1 and $p_2/p_1\left(M_1,\xi_1\right) \approx \pi_{12}\left(M_1\right)$ as shown Figure 5-11. Though the incoming relative flow is subsonic at the low end of the curve depicted in the figure, there is still a static pressure rise since the relative flow Mach number decreases as the flow enters the blade passage. The variation in

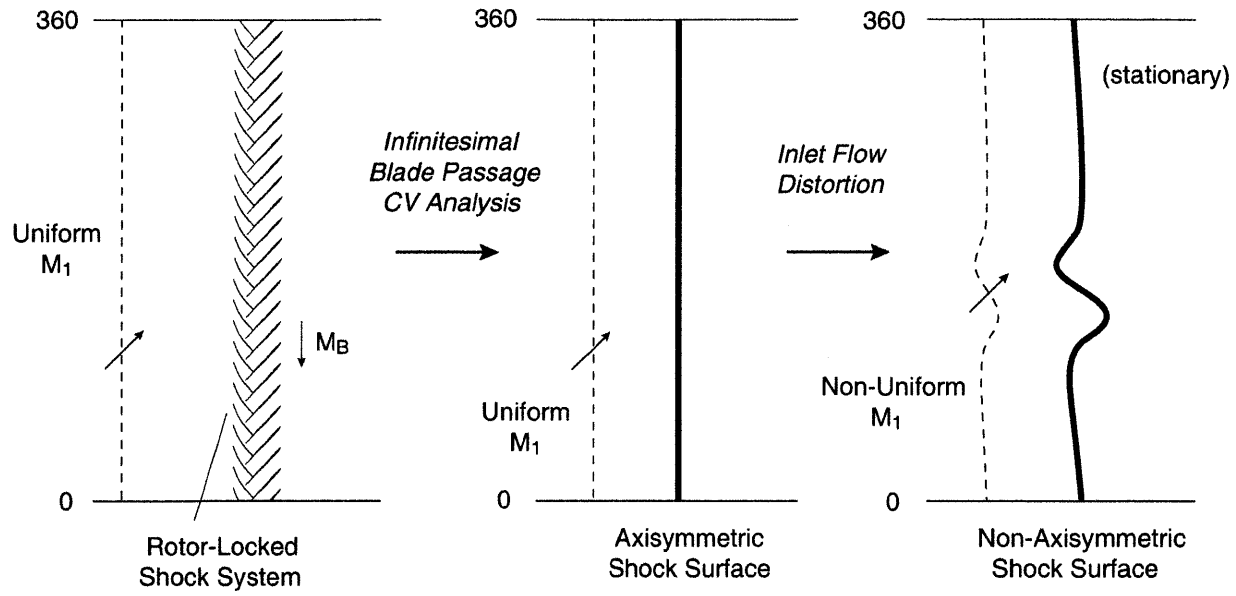

Figure 5-9: Modulated shock surface model.

relative Mach number around the circumference is schematically depicted in the inset leading to a peak-to-peak change in shock strength of $\Delta\pi_{12} = 0.3$.

Assuming now that the blade-to-blade pressure variation is a rotor-locked saw-tooth distribution $N(\theta + \Omega t)$ of unit strength, the modulated rotor-locked static pressure ratio distribution becomes

$$\pi_{12} = \pi_{12}(\theta)\, N(\theta + \Omega t) \tag{5.2}$$

For simplicity, it is assumed that the stagnation pressure upstream is uniform[4]. The peak-to-peak rotor-locked pressure variation $\Delta p_{21} = p_2 - p_1$ is then readily determined and can be written in terms of a modulated spatial Fourier series

$$\Delta p_{21}(\theta, t) = \sum_{m=0}^{\infty} P_m e^{jm\theta} \sum_{n^*=1}^{\infty} C_n e^{jn^* B(\theta+\Omega t)} \tag{5.3}$$

where B is the rotor blade count. The first Fourier series represents the modulation of the stationary shock surface while the second series is the decomposition of the

[4]This is deemed appropriate as the inlet pressure recovery is 99% at the low cut-back flight Mach number of 0.1.

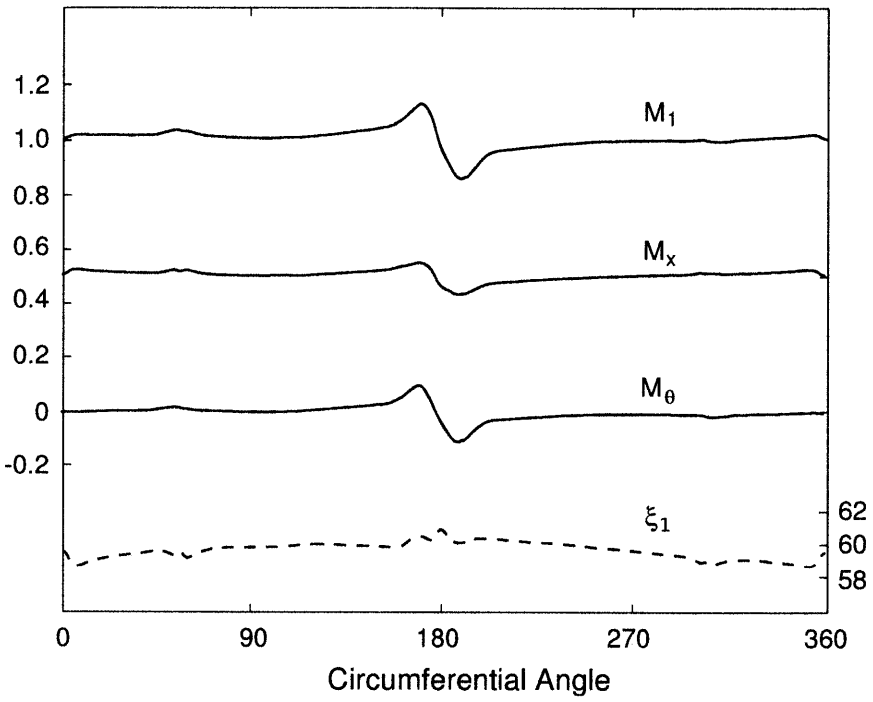

Figure 5-10: Computed Mach numbers and relative flow angle at 92% span at rotor leading edge for serpentine inlet case.

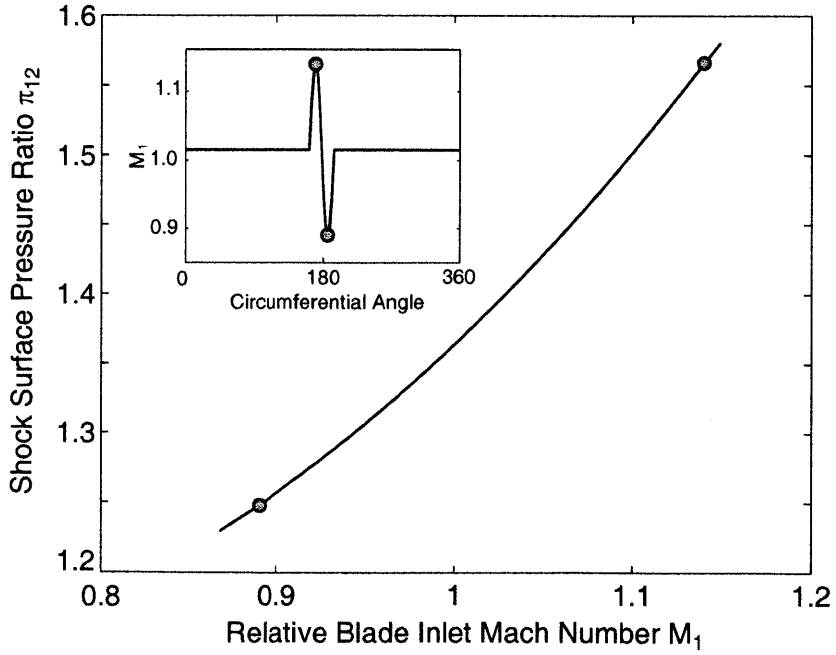

Figure 5-11: Shock strength dependence on relative Mach number; inset: inlet distortion as idealized relative Mach number distribution.

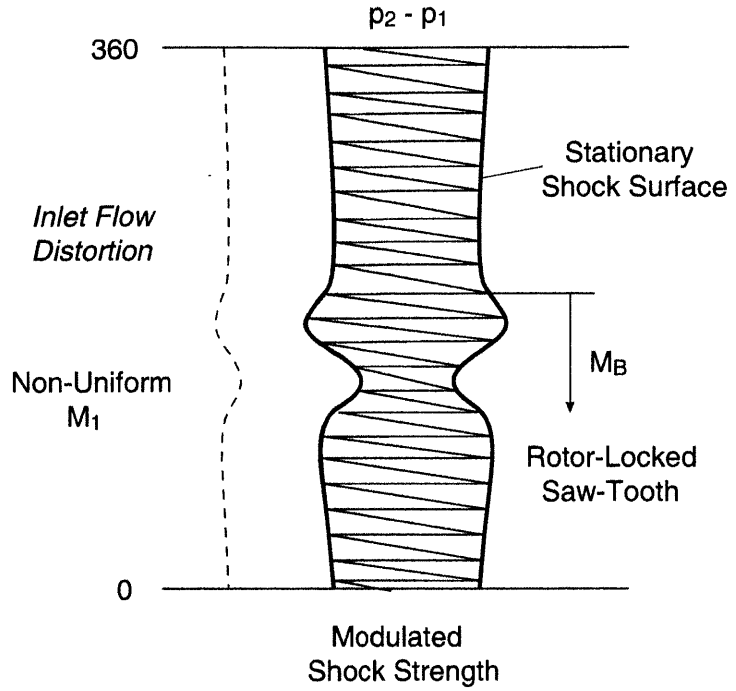

Figure 5-12: Rotor-locked sawtooth wave modulated by stationary shock surface in non-uniform flow.

rotor-locked sawtooth pressure pattern. This is illustrated schematically in Figure 5-12. The modulated shock strength induces non-zero modal amplitudes in shaft-order (and harmonics) spatial modes which are not present in the uniform inflow case.

The manner in which the wave propagation behavior upstream of the rotor is altered due to the modulated shock surface strength is investigated next. While the propagation of acoustic waves through the non-uniform mean flow in the serpentine duct is complicated, the analysis can be used to investigate the linear wave behavior in the near-field of the rotor where the duct outer radius is approximately constant. Assuming small perturbations, uniform background flow in the axial direction, and neglecting radial variations, the two-dimensional convective wave equation can be written for a periodic domain as

$$\frac{1}{a^2}\left(\frac{\partial}{\partial t}+\overline{u_x}\frac{\partial}{\partial x}\right)^2\delta p-\frac{\partial^2\delta p}{\partial x^2}-\frac{1}{R^2}\frac{\partial^2\delta p}{\partial\theta^2}=0 \tag{5.4}$$

The solution to the above equation will be of the form

$$\delta p\left(x,\theta,t\right)=\sum_{m=0}^{\infty}\sum_{n^{*}=1}^{\infty}\zeta_{mn^{*}}\left(x\right)e^{j\left[m\theta+n^{*}B\left(\theta+\Omega t\right)\right]} \tag{5.5}$$

Note the presence of the $e^{jm\theta}$ term, which appears as a result of the distorted inflow and is not time-dependent. Substituting this into Equation 5.4 yields a second order differential equation for $\zeta_{mn^{*}}$

$$\begin{aligned}\left(1-M_{x}^{2}\right)\frac{d^{2}\zeta_{mn}\left(x\right)}{dx^{2}}-2j\frac{n^{*}B}{R}M_{x}M_{u}\frac{d\zeta\left(x\right)}{dx} \quad + \\ \left[\left(\frac{n^{*}B}{R}\right)^{2}\left(M_{u}^{2}-1\right)-\left(\left(\frac{m}{R}\right)^{2}+\frac{2mn^{*}B}{R^{2}}\right)\right]\zeta_{mn^{*}}\left(x\right) \quad = \quad 0\end{aligned} \tag{5.6}$$

where $M_{1}=\sqrt{M_{x}^{2}+M_{u}^{2}}$. With the known rotor pressure field at $x=0$ and invoking Sommerfeld's irradiation condition far upstream, the solution for $x<0$ becomes

$$\zeta_{mn^{*}}(x)=\Lambda_{mn^{*}}e^{jk_{x}x} \tag{5.7}$$

where $\Lambda_{mn^{*}}=P_{m}C_{n^{*}}$ and the axial wavenumber yields

$$k_{x}=\frac{n^{*}B}{R}\left(\frac{M_{x}M_{u}-j\sqrt{\left(\frac{m}{n^{*}B}+1\right)^{2}\left(1-M_{x}^{2}\right)-M_{u}^{2}}}{1-M_{x}^{2}}\right) \tag{5.8}$$

Evanescent wave behavior is obtained when the square root remains real and therefore wave propagation is cut-off for

$$\frac{m}{n^{*}B}+1>\frac{M_{u}}{\sqrt{1-M_{x}^{2}}} \tag{5.9}$$

For a uniform shock surface strength (no distortion, $m=0$ only), the familiar wave propagation condition $M_{1}>1$ is recovered and modes are cut-on for supersonic relative blade inlet Mach numbers. With inlet flow distortion the shock surface strength is non-uniform ($m\geq 0$) and the cut-on behavior depends on the reduced spatial frequency, $m/n^{*}B$. For values much less than one, the behavior approaches

the uniform inflow case whereas for values close to one, where the length scale of the shock strength variation is of order blade pitch, modes can be cut-off even if the relative inlet Mach number is supersonic. For the serpentine inlet flow conditions in the computation discussed above, the maximum inlet relative Mach number near the blade tips is 1.1 and the axial Mach number is approximately 0.5. Therefore in order for a mode to be cut-off, the reduced spatial frequency must satisfy

$$\frac{m}{n^* B} > 0.13 \tag{5.10}$$

Since $B = 22$ for the NASA/GE R4 rotor investigated here, the cut-off condition becomes $m > 2n^*$. Considering the lowest harmonic $n^* = 1$, the analysis suggests that any shock surface modulation of spatial harmonic extent greater than $m = 2$ can lead to cut-off behavior. For the type of inlet distortion observed in the simulation, the fundamental component of the distortion $P_{m=0}$ is typically larger than $P_{m>0}$ by at least an order of magnitude. With this, the simplified model suggests that, since the sound intensity $I_{mn^*} \propto \Lambda^2_{mn^*}$ for uniform inflow, the net increase in sound intensity relative to uniform inflow is negligible. It can thus concluded that, for small perturbations, linearized shock surface modulation in a uniform background flow cannot by itself yield the observed 38 dB increase in fan rotor sound power level. Instead, it is conjectured that the combination of non-uniform shock surface strength and the propagation of sound through non-uniform inflow results in the computed increase in sound power.

The conclusion from analysis is that non-uniform flow affects the acoustic propagation more dominantly than it affects the source unsteady pressure distribution. To accurately capture the non-uniform flow effects, fully three-dimensional, unsteady simulations such as those employed in this work are required. Chapter 7 presents the results of a parametric study of serpentine inlet simulations to determine the influence of the non-uniform background flow on source noise generation and wave propagation.

5.5 Conclusions

The generation and propagation of rotor-alone tones in conventional and serpentine inlet ducts have been investigated using the body-force-based approach developed in Chapter 3 and assessed in Chapter 4. The non-uniform flow in the serpentine inlet results in a 38 dB increase in sound power at the fan face relative to the uniform flow condition. In the far-field, however, the average increase in OASPLs at the receiver locations is only 7 dB or 3 dBA.

The far-field spectra differ qualitatively for the two cases. Compared to the conventional inlet, the serpentine inlet results have higher SPLs at frequencies less than one-half BPF, while tones above this frequency appear to be cut-off. Examination of the inlet distortion pattern in the vicinity of the fan leading edge revealed that the frequency above which tones are absent in the far-field may to be related to the circumferential extent of the distortion. A simplified model of the rotor noise source generation in non-uniform flow was presented which explains the circumferential variation in shock strength due to inlet distortion. The presence of inlet distortion energizes higher-order circumferential modes at the BPF in the model. A linearized wave propagation analysis assuming uniform flow based on this model provides criteria for propagating modes. The analysis indicates that the increase in source sound power, the amplification of tones below one-half BPF and the apparent cut-off of tones above this frequency are predominantly governed by acoustic propagation effects through the non-uniform flow rather than by inlet distortion effects on the fan's unsteady pressure field. This motivates a parametric study of duct geometries in order to determine the dependence of the far-field spectra on inlet distortion characteristics, presented later in Chapter 7.

Chapter 6

Sound Power In Non-Uniform Flow

This chapter presents an assessment of the error resulting from ignoring flow non-uniformities in the computation of sound power. In the previous two chapters, in-duct sound power was computed by assuming uniform flow in order to perform a modal decomposition of the unsteady pressure field based on analytical solutions to the governing Helmholtz equation. This is consistent with the approach by Sutliff [42] employed in the analysis of the experimental data for the R4 rotor, allowing direct comparisons to be made between the conventional and serpentine inlets. For conventional inlets with axisymmetric inflow, the only flow non-uniformities stem from radial flow field gradients. The error arising from the use of the uniform-flow assumption is determined for both the conventional and serpentine inlet cases previously investigated. The error is defined as the difference between the least-squares fit to the radial pressure distribution and the computed solution. The serpentine inlet has a total normalized RMS error at BPF which is a factor of 3.2 higher at the AIP than it is at the same location for the conventional inlet. In non-uniform flow, the solution to the Helmholtz equation governing the acoustic pressure field does not have an analytical solution that is separable into sums of azimuthal Fourier and radial Bessel modes. This is the reason for the increase in error in the case with distorted inflow.

An alternative approach is therefore needed for assessing sound power in non-uniform flow. As discussed in Section 2, the work by Myers on unsteady disturbance energy fluxes [27] provides a basis for determining the sound power in arbitrarily non-

uniform flows and further is not restricted to annular or rectangular duct geometries as are approaches based on analytical solutions to the Helmholtz equation. Instead, it can be used to determine the sound power propagating through any arbitrary control surface. The difference between the sound power computed by assuming uniform flow and by using disturbance energy fluxes is assessed at the fan leading edge, the AIP, and the inlet plane (upstream end of the serpentine duct) and it is found that the uniform-flow assumption can over-predict the sound power level by as much as 11 dB.

An important aspect of noise assessment is the determination of the frequency distribution of the acoustic energy. The work by Myers did not address how to obtain a spectrum of sound power. By extending the existing approach, a method is developed to determine the spectrum of sound power by dissecting the contributions from the Fourier series representation of each of the terms in disturbance energy flux. This enables the accurate computation of sound power spectra for arbitrarily-shaped surfaces in any non-uniform flow. This is an important capability necessary for the assessment of the effects of serpentine inlet geometry on MPT noise.

6.1 Flow Non-Uniformity Effects on Sound Power

Sound power in ducts is commonly determined by assuming uniform flow in a circular or annular duct. Under these assumptions, the solution to the Helmholtz equation for the unsteady pressure field in the duct is separable into circumferential and radial parts as described in Candel and Poinsot [45]:

$$p'(x, r, \theta, t) = \Psi(r, \theta)\, e^{jk_{||}x - j\omega t} \tag{6.1}$$

where the transverse eigenfunction $\Psi(r, \theta) = R(r)\Theta(\theta)$. The circumferential solution must be representable by a Fourier series owing to its periodicity, while the radial problem is described by Bessel's equation such that solutions are comprised of sums of Bessel functions (restricted to Bessel functions of the first kind for the hard-walled cases considered here). The uniform-flow approach assumes that the transverse eigen-

function Ψ has such a solution, composed of modes (m, n) where m represents the circumferential order and n the radial order. The mass-averaged Mach number in the duct, along with the duct inner and outer radii, are used to determine the cut-on ratio of each mode. At each frequency, every circumferential mode thus has a finite number of cut-on radial modes, n_{max}. It is then assumed that the radial field can be represented by $(n_{max} + 1)$ modes; this is the number of Bessel functions used in a least-squares fit of the radial unsteady pressure field data. The error to be minimized in the least-squares fit is given by [42]

$$\epsilon = \sum_{n=0}^{n_{max}} p'_{mnf} J_m \left(\kappa_{mn} r\right) - p'_{mrf} \tag{6.2}$$

where J_m is the Bessel function of the first kind of order m, and κ_{mn} is the nth solution of the equation [42]

$$\kappa_{mn} \frac{J_{m+1}\left(\kappa_{mn}\right)}{J_m\left(\kappa_{mn}\right)} - m = 0 \tag{6.3}$$

p'_{mnf} is the fluctuating pressure amplitude for a given circumferential mode m, radial mode n, and frequency f, while p'_{mrf} is the fluctuating pressure amplitude for a given circumferential mode and frequency at a radial location r.

To assess the impact of non-uniform flow on this error, the RMS value of the error ϵ from the hub to tip radii is determined for each cut-on circumferential mode at the blade-passing frequency at the AIP for the conventional and serpentine inlets, as depicted in Figure 6-1. The RMS errors are normalized by the peak p_{mrf} value over all cut-on circumferential modes at the BPF. For the majority of the cut-on circumferential modes, the error is increased for the serpentine inlet case. To quantify the overall effect, this error is summed over all modes. This gives a total peak-normalized RMS error of 0.74 for the conventional inlet versus a total peak-normalized error of 2.37 for the serpentine inlet, representing an increase by a factor of 3.2.

Another aspect of the uniform-flow assumption that can be assessed, in terms of the impact of non-uniform flow on the solution accuracy, is the propagation of cut-

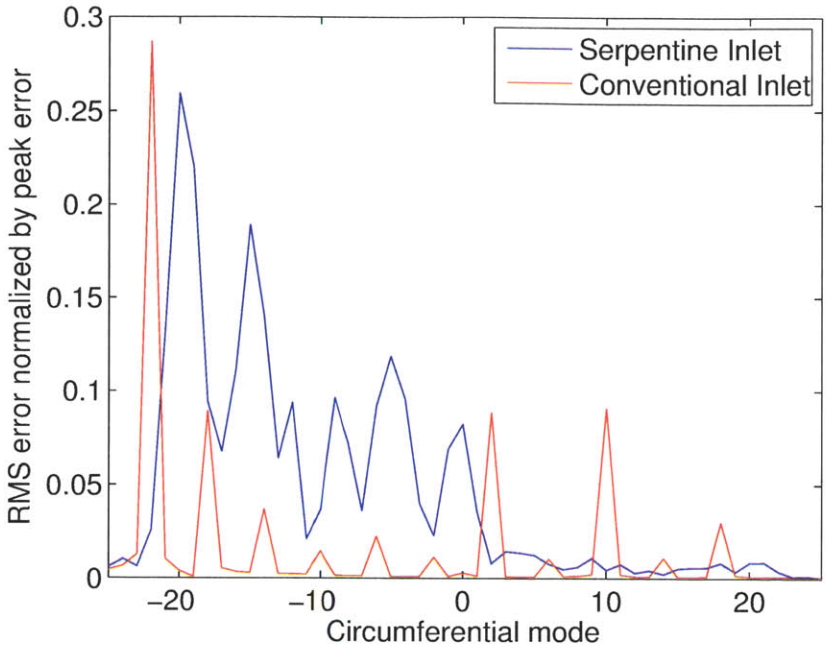

Figure 6-1: RMS error (normalized by peak error) vs. circumferential modes at BPF using a least-squares fit of Bessel-based radial modes at the AIP.

on modes. In uniform flow, assuming a constant cross-section duct, cut-on modes propagate without decay. While the cross-section of the duct from the fan to the AIP varies, comparing the ratio of the amplitudes of the cut-on modes at the fan to their amplitudes at the AIP for the conventional and serpentine inlets reveals the impact of the non-uniform flow in the serpentine inlet case. These ratios are plotted at the BPF in Figures 6-2 and 6-3. In a uniform flow with no variation in the duct cross-sectional area and linear acoustics, the ratio for all cut-on modes would be 1.0.

It can be seen that in both cases, the majority of the modes are attenuated while some are amplified. Non-linear effects due to the existence of shocks near the fan, as well as changes in duct cross-section and radial mean-flow gradients all contribute to the deviations of the ratio from 1.0 for the conventional inlet; for this inlet, the average ratio across all cut-on modes is 0.0058, while for the serpentine inlet it is 0.023. This represents an increase by a factor of 3.9 due to the non-uniform flow. This might seem to indicate that the serpentine inlet's propagation behavior is actually a better

match to the uniform-flow Helmholtz equation solution behavior (i.e., closer to 1.0) than that of the conventional inlet. However, the non-linear acoustic effects near the fan are responsible for the decay of the majority of the propagating modes. Thus the higher average modal amplitude ratio for the serpentine inlet case is due to the increased number of modes for which the ratio is greater than one, indicating that acoustic energy is redistributed from one mode to another due to the non-uniform flow. The non-uniform flow in the serpentine inlet enhances the redistribution of acoustic energy between modes, increasing the average ratio of the modal amplitudes at BPF from the fan leading edge to the AIP by a factor of 3.9.

These two analyses emphasize that it is not possible to adequately represent the acoustic field in a duct with the types of non-uniform flows which result from boundary layer ingestion using distinct Bessel-function based radial and Fourier-series-based circumferential modes. Rather, the acoustic field as a whole must be considered. Another way of approaching the problem of how to compute the sound power in non-uniform flow is required, presented in the next section.

6.2 Sound Intensity as a Basis for Computing Sound Power

The sound power ϖ_p propagating through a surface A is given by

$$\varpi_p = \int_A \vec{I} \cdot d\vec{A} \tag{6.4}$$

where $\vec{I}$ is the sound intensity vector. In non-uniform flow, the challenge lies in determining $\vec{I}$. Myers [27] developed a general expression for the disturbance energy flux $\vec{W}$, whose time-average is the sound intensity vector:

$$\vec{I} = \frac{1}{\Delta t} \int_t^{t+\Delta t} \vec{W}(\tau)\, d\tau \tag{6.5}$$

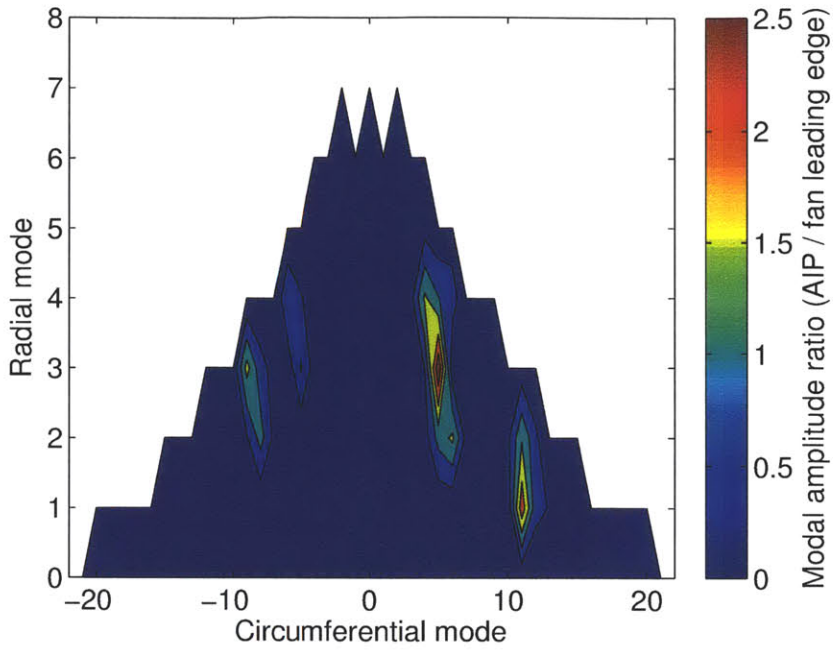

Figure 6-2: Deviation of cut-on modal amplitudes from uniform-flow values for the conventional inlet.

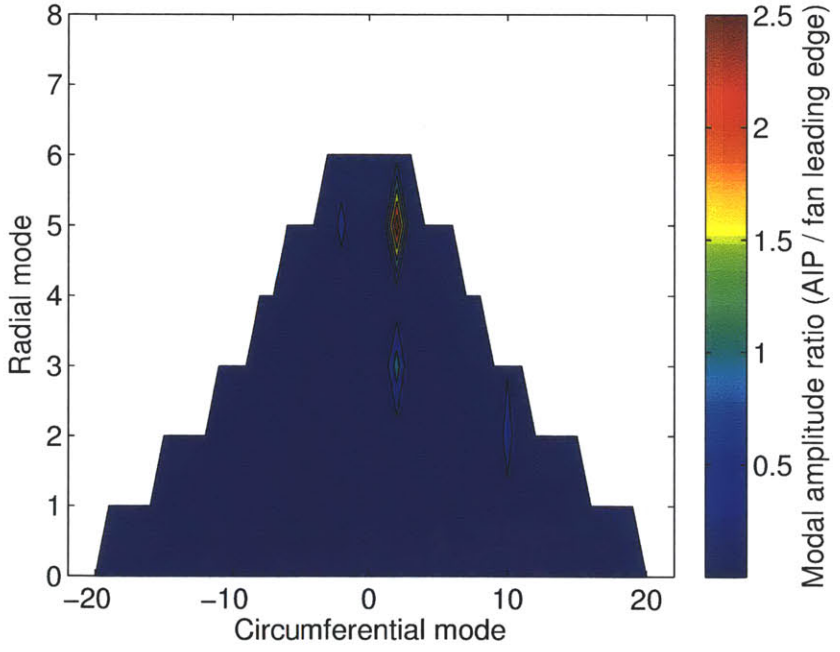

Figure 6-3: Deviation of cut-on modal amplitudes from uniform-flow values for the serpentine inlet.

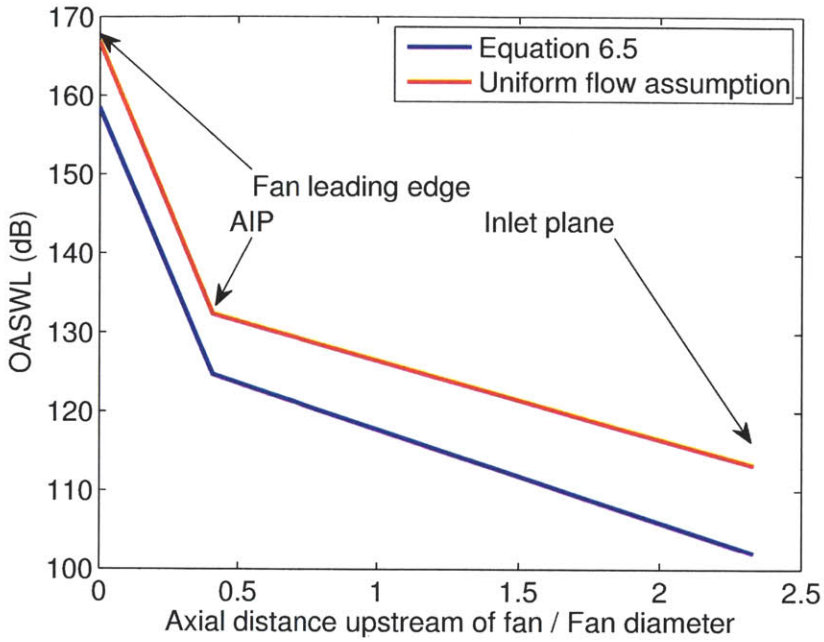

Figure 6-4: Overall sound power level in-duct evolution for serpentine inlet.

$\vec{W}$ is given by Equation 2.6; for inviscid, adiabatic flow it simplifies to

$$W_i(t) = l_i' H' - T_0 l_i' s' + l_{0i} T' s' \tag{6.6}$$

where the primes indicate fluctuating quantities and the subscript 0 indicates a time-averaged value. In Figure 6-4, an assessment of the impact of computing the sound power in this manner, as opposed to using the uniform flow assumption, is shown for the serpentine inlet case studied in Chapter 5. The figure directly compares the overall sound power level (OASWL), computed up to and including the blade-passing frequency, for the uniform-flow assumption and using Equation 6.5. The uniform flow assumption results in over-prediction of the overall sound power by 8 dB at the fan leading edge and AIP and by 11 dB at the inlet plane. These are significant errors whose magnitudes emphasize the importance of accounting for non-uniform flow when computing sound power. Therefore the intensity as given by Equation 6.5 will be used for the determination of sound power in serpentine inlets in the following sections.

6.3 Sound Intensity Spectra in Non-Uniform Flow

A method for obtaining the sound power spectrum in non-uniform flow is needed to analyze the acoustic fields obtained from the computations. Since the sound power is the integral of the sound intensity over a surface, the problem is reduced to obtaining the frequency distribution of contributions to the sound intensity vector $\vec{I}$. Since the intensity is the time-average of the disturbance energy flux $\vec{W}(t)$, a simple Fourier transform of the signal $\vec{W}(t)$ does not provide the intensity spectrum as only the DC component of the transformed signal has a non-zero time average. Instead, the contributions to the intensity from the constituent terms of $\vec{W}(t)$ must be determined at each frequency. Recall that in inviscid, adiabatic flow the disturbance energy flux is given by Equation 6.6. $W_i(t)$ can be written as the sum of Fourier series representing the three terms in Equation 6.6:

$$W_i(t) = \sum_{\eta=-\infty}^{\infty} [\mathrm{lH}]_{\eta i} e^{j\eta t} - T_0 \sum_{\eta=-\infty}^{\infty} [\mathrm{ls}]_{\eta i} e^{j\eta t} + l_{0i} \sum_{\eta=-\infty}^{\infty} [\mathrm{Ts}]_{\eta} e^{j\eta t} \tag{6.7}$$

where

$$\begin{aligned} [\mathrm{lH}] &= l_i' H' \\ [\mathrm{ls}] &= l_i' s' \\ [\mathrm{Ts}] &= T' s' \end{aligned}$$

Each of these terms is composed of a product of two time-varying signals which can be represented by Fourier series. Since the sound intensity is the sum of the DC components of the series in Equation 6.7, a representation of these series by the products of the Fourier series of their constituent terms is sought. The product of two Fourier series is another Fourier series:

$$\sum_{m=-\infty}^{\infty} a_m e^{jmt} \sum_{n=\infty}^{\infty} b_n e^{jnt} = \sum_{\eta=-\infty}^{\infty} c_\eta e^{j\eta t}$$

The DC part of the single series, $c_{\eta=0}$, is .

$$c_{\eta=0} = \sum_{n=-\infty}^{\infty} a_n b_{-n} = a_0 b_0 + \sum_{n=1}^{\infty} (a_n b_{-n} + a_{-n} b_n) \tag{6.8}$$

Therefore, since the fluctuating quantities l_i', H', s', and T' have DC components equal to zero by definition, the sound intensity can be written as

$$\begin{aligned} I_i &= [\mathrm{lH}]_{(\eta=0)i} - T_0 [\mathrm{ls}]_{(\eta=0)i} + l_{0i} [\mathrm{Ts}]_{(\eta=0)} \\ I_i &= \sum_{\eta=1}^{\infty} \left[\left(l'_{\eta i} H'_{-\eta} + l'_{-\eta i} H'_{\eta} \right) - T_0 \left(l'_{\eta i} s'_{-\eta} + l'_{-\eta i} s'_{\eta} \right) + l_{0i} \left(T'_{\eta} s'_{-\eta} + T'_{-\eta} s'_{\eta} \right) \right] \end{aligned} \tag{6.9}$$

where the quantities with subscript η represent the coefficients of the Fourier series representations of the relevant quantities. The spectral sound intensity at frequency $f = \eta/\tau$ (τ is the fundamental period of oscillation) is then simply the ηth term of this series:

$$I_i(f) = \left(l'_{\eta i} H'_{-\eta} + l'_{-\eta i} H'_{\eta} \right) - T_0 \left(l'_{\eta i} s'_{-\eta} + l'_{-\eta i} s'_{\eta} \right) + l_{0i} \left(T'_{\eta} s'_{-\eta} + T'_{-\eta} s'_{\eta} \right) \tag{6.10}$$

By integrating over a control surface of interest (such as a duct cross-section) the sound power spectrum is obtained. This represents the contribution to the total sound power from components of the underlying field at a given frequency. The capability to accurately represent the spectrum of sound power propagating through an arbitrary control surface with non-uniform background flow enables acoustic analysis in a general class of geometries and flows without restrictions on the duct cross-section or flow non-uniformities. This capability is needed is in serpentine inlets with boundary layer ingestion, since the flow is non-uniform and the duct is curved and may have a varying cross-section.

6.4 Concluding Remarks

Using the uniform-flow solution to the Helmholtz equation to determine which modes propagate in non-uniform flow leads to errors in computed sound power. This error has been assessed for axisymmetric but radially non-uniform flow and for non-uniform flow containing swirl-type distortion. The sum across propagating circumferential modes of the peak-normalized RMS error is a factor of 3.2 higher at the BPF for the case with distorted flow. This increase in error is due to the fitting of radial modes using Bessel basis functions in non-uniform flow. For a constant cross-sectional area duct with uniform flow, cut-on modes theoretically propagate without decay. Examining the ratio of cut-on modal amplitudes from the fan leading edge to the AIP, the average modal amplitude ratio at the blade-passing frequency (which would be 1.0 in the constant cross-section, uniform-flow case) is less than 0.03 for both cases, but is 3.9 times higher for the serpentine inlet as several modes are amplified. This amplification can only occur in non-uniform flow.

In light of this increase in error, an approach based on the work by Myers is presented as an alternative for computing sound power without simplifying assumptions. Results for the serpentine inlet case from Chapter 5 showed that the uniform-flow assumption results in over-prediction of the sound power by up to 11 dB OASWL. In the approach presented in this chapter, the disturbance energy flux is determined at every location in the flow field; the local sound intensity vector is obtained by taking the time-average of this flux. Integrating this vector over a control surface gives the sound power propagating through that surface.

From the terms comprising the disturbance energy flux, the spectral content of the sound intensity (and thus the sound power) can be obtained. This enables the detailed assessment of sound power propagation in any type of geometry and/or flow. This improved analysis tool is employed in the remainder of this thesis.

Chapter 7

Parametric Study of Serpentine Inlet Designs

The results of Chapter 5 provided insight into the effects of non-uniform flow on MPT noise generation and propagation for a specific serpentine inlet. To investigate the mechanisms by which the serpentine duct geometry affects MPT noise, a parametric study of serpentine inlet designs are presented and analyzed. The goal is to uncover the links between the non-uniform flow and the acoustics for boundary-layer ingesting serpentine inlets with swirl-type distortion. NASA's ANOPP noise prediction code [46, 47] does not currently include the effects of inlet swirl distortion on MPT noise. To extend the capabilities of ANOPP, the impact of the swirl-type distortions which result from boundary layer ingestion must be determined.

The approach taken here is to parametrically study the effects of serpentine inlet geometry, holding the ingested boundary layer properties fixed. In this chapter, the parameter space for the serpentine inlets, the duct geometry used and the chosen solution to airframe-engine integration issues are presented, followed by an overview of the computational setup. The dependence of the MPT noise on the duct geometry is quantified over the parameter space explored. For this first assessment of the impacts of duct geometry on noise generation and propagation, the parameters varied are the serpentine duct downstream-to-upstream area ratio (1.01 and 1.05) and the duct offset to downstream diameter ratio (0.25 and 0.75). The key results are that (1) the

apparent far-field cut-off frequency is not dependent on the details of the serpentine inlet geometry, but rather depends on the external flow outside the inlet; (2) the overall sound pressure levels in the far-field increase by 3.8 dB when the duct area ratio increases from 1.01 to 1.05; (3) the sound power level at the fan is not sensitive to the inlet duct geometry but is increased by the ingestion of streamwise vorticity; and (4) the critical internal flow feature in the serpentine inlets is lift-off of the streamwise vortices from the bottom of the duct. When this occurs the far-field directivity is altered and the in-duct sound power attenuation is reduced by 9 dB.

These findings enable the development of a response-surface correlation for the effects of serpentine duct geometry with swirl-type distortion on far-field noise, as described in Chapter 8.

7.1 Parameter Space, Duct Geometry, and Integration

The parameters varied in this investigation are the duct area ratio and offset ratio, defined as

$$AR = \frac{A_{AIP}}{A_{throat}} \tag{7.1}$$

and

$$OR = \frac{\delta}{D_{AIP}} \tag{7.2}$$

respectively. A_{throat} and A_{AIP} are the areas of the upstream and downstream ends of the serpentine duct; δ is the vertical duct offset and D_{AIP} is the downstream duct diameter. Unlike the serpentine duct studied in Chapter 5, the ducts studied parametrically here have circular cross-sections over their entire lengths. This choice was made since a uniform cross-section (but with varying area) removes the influence of cross-sectional change from the results. This reduces the complexity of the task of extracting the flow mechanisms leading to changes in acoustic behavior for serpentine inlets.

The parametric study consists of four cases, at the corners of the parameter space

bounded by $1.01 \leq AR \leq 1.05$ and $0.25 \leq OR \leq 0.75$, as depicted in Figure 7-1, which shows the duct symmetry planes. All ducts have axial length-to-diameter ratios $L/D_{AIP} = 2$. The bounding values were chosen for the following reasons:

- $AR = 1.05$: The free-stream Mach number is 0.1 (same as for the previously studied cases), streamtube contraction occurs outside of the inlet. The flow is qualitatively similar to that in Figure 4-8, with a stagnation point on the outside of the nacelle and acceleration of the flow around the inlet lip. Increasing the area ratio amplifies the overspeed outside the inlet. A maximum value of 1.05 is selected to maintain consistency with the work of Madani & Hynes [24].

- $AR = 1.01$: This is the minimum area ratio from the work of Madani & Hynes [24].

- $OR = 0.25$: Choosing a non-zero minimum offset assists in obtaining the sensitivity of the acoustics to the offset ratio. Testing a $OR = 0$ configuration would have been a desirable additional data point, buy time limited the parametric study to two non-zero offsets.

- $OR = 0.75$: For the conditions used in the current work, two-dimensional viscous calculations have shown that the in-duct flow separates at offset ratios approaching 1.0. The highest offset ratio of 0.75 is selected to ensure that the real (viscous) flow remains attached.

The serpentine ducts consist of a cosine centerline distribution with linearly-varying area. The centerline is given by

$$\frac{y}{D} = \frac{OR}{2}\left(1 + \cos\left(-\pi + \pi \frac{x}{D}\frac{L}{D}\right)\right) \tag{7.3}$$

and the cross-sectional area is given by

$$A^* = \frac{1}{AR} + \left(1 - \frac{1}{AR}\right)\frac{s^*}{s^*_{max}} \tag{7.4}$$

where s^* is the dimensionless arc length along the duct centerline.

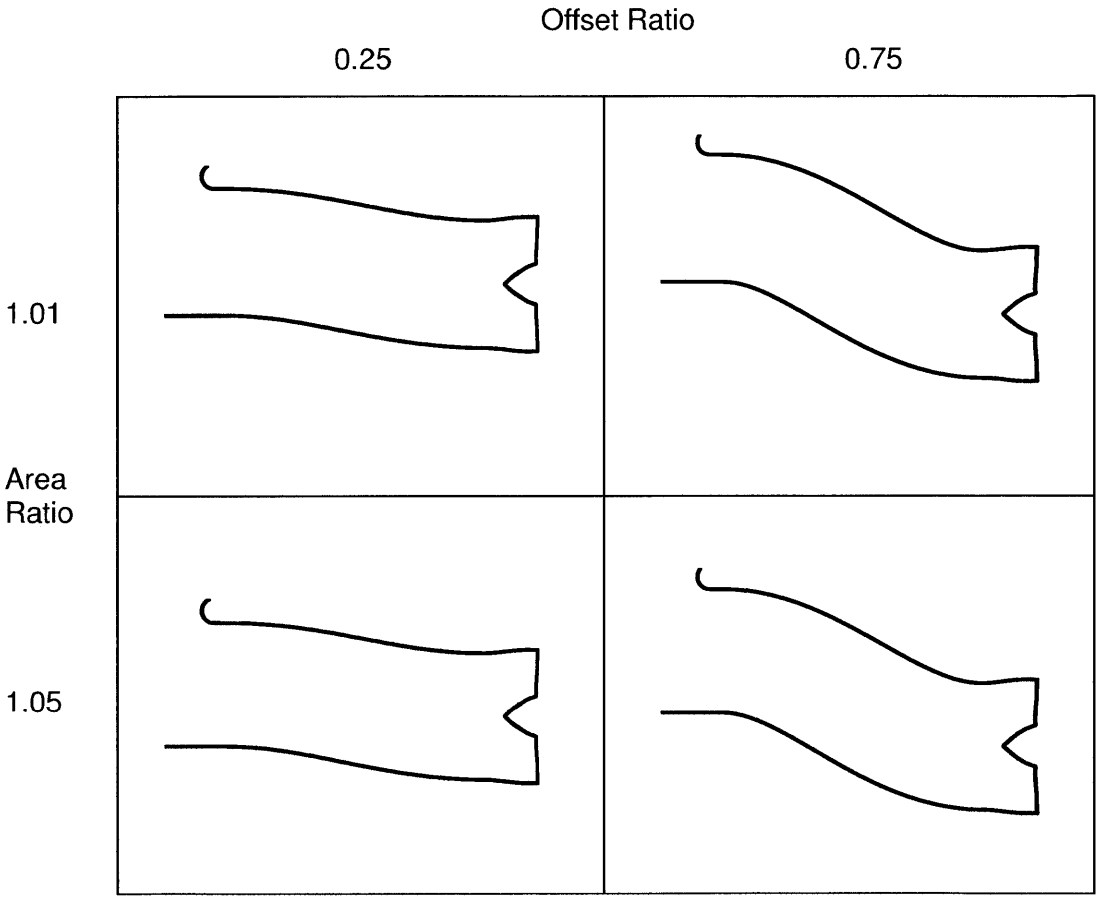

Figure 7-1: Serpentine inlets used in the parametric study.

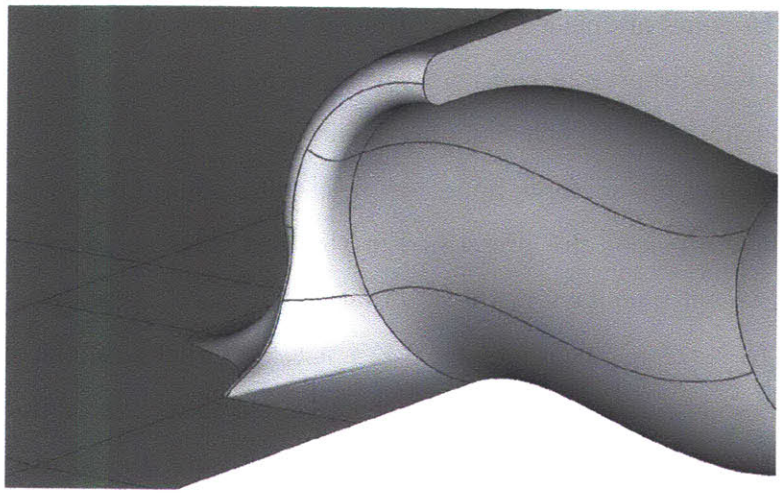

Figure 7-2: Cut through the duct symmetry plane, showing the integration of the serpentine inlet onto flat plate.

The serpentine inlet ducts are mated to the diffusing portion of the NASA/GE R4 conventional nacelle and body-force-based fan model such that the AIP is located at the throat of the conventional inlet, in a manner identical to the inlet studied in Chapter 5. At the upstream end, the serpentine inlets are flush-mounted on a flat plate representing an airframe upper surface, illustrated in Figure 7-2. The inlet is smoothly blended to the plate. The flat plate is used for simplicity since the focus is on the acoustics rather than the aerodynamics.

7.2 Computational Setup

The computational domain includes the rotor region, the upstream duct and inlet, and the external flow field, in a similar configuration to the serpentine inlet case presented in Chapter 5. The same boundary layer and related stagnation pressure deficit used in Chapter 5 are defined 10 diameters upstream of the inlet.

The inherent dissipation present in the inviscid solver used is compensated for in the far-field acoustic results for all cases. The FW-H surface is placed approximately 1.5 fan diameters from the inlet plane. The computational domain for each case comprises approximately 15 million cells, employing a structured grid topology.

Acoustic buffer zones are placed outside the FW-H surface and in the duct far downstream of the rotor to prevent spurious wave reflections. The buffer zone formulation uses grid stretching and explicit damping as discussed in Section 3.7. The stagnation pressure (including the airframe boundary layer stagnation pressure deficit) and the free-stream flow direction are prescribed at the upstream boundary of the domain. At the downstream boundary in the external flow domain, the static pressure is set to make the free-stream Mach number 0.1. For the internal flow, the static pressure at the boundary downstream of the rotor is used to set the corrected flow through the inlet. In all four computations, the same far-field measurement locations relative to the fan are used as were employed in the validation of the conventional inlet presented in Chapter 4.

The unsteady computations are initialized from steady calculations, converged for a corrected flow of 38 kg/s in the inlet, and carried out until two rotor revolutions of periodic acoustic data are recorded at all receiver locations. This ensures sufficient resolution in the frequency domain to identify tones down to shaft order in the far-field spectra. The approximate time required for the acoustic waves generated at the fan to reach the FW-H surface is 2.5 rotor revolutions.

7.3 Mean Flow Aerodynamics

Two features of the duct mean flow aerodynamics which play an important role in MPT noise generation and propagation are the ingestion of streamwise vorticity and, for the duct with $AR = 1.01$ and $OR = 0.75$, the in-duct lift-off of the streamwise vortices. These phenomena are explained next.

7.3.1 Ingestion of Streamwise Vorticity

Previous work [23, 24] has primarily examined the performance of embedded propulsion systems at cruise. At a cruise Mach number of 0.8, the SAX-40 has approximately 30% BLI [24] and an inlet pressure recovery of approximately 0.92. At the low-speed condition ($M_\infty = 0.1$) used in this work, there is approximately 20% BLI and the

inlet pressure recovery is greater than 99%. In both cases the AIP Mach number is approximately 0.5, so that the flow decelerates into the inlet at cruise and accelerates into the inlet for $M_\infty = 0.1$. Thus the mass-averaged pressure coefficient at the AIP for the cruise condition is positive while for the low-flight-speed condition is it negative. The net result is that while for the cruise condition, it is the stagnation pressure deficit which can dominate the character of the inlet distortion, at low speeds it is the ingested vorticity in the boundary layer which is most important. While this vorticity is generally perpendicular to the flow direction upstream of the inlet, as it interacts with the inlet lip it is tipped into and stretched along the streamwise direction which causes swirl distortion in the inlet duct, as depicted in Figure 7-3. The streamwise vorticity is enhanced by the stretching of the vortex lines as the flow accelerates into the inlet. The effect is to create a region of high-speed flow centered around the vortex cores. This phenomenon is observed at the inlet planes of all four ducts (Figure 7-5). Refer to Figure 7-4 for the location of the inlet plane and other locations at which the flow field has been captured.

The type of vortices extant at the inlet plane can be determined by examining circulation distributions. In Figure 7-6, the magenta crosses indicate the estimated locations of the vortex cores. These were assumed to coincide with the locations of maximum circumferential velocity since the forced-vortex cores (outside of which free-vortex behavior was expected) were initially thought to be compact as a result of the inviscid nature of the flow. The blue and red curves indicate the furthest radii from these cores at which the circulation increases.

The vortices resemble Burgers vortices, which combine a Rankine vortex core with a free-vortex outer region. Though in an inviscid flow vortices are typically represented as having compact cores, discretization effects due to the relatively coarse grid govern the resultant vorticity distribution, emulating the effect of viscosity in a real flow. The Burgers vortex can be characterized by the Reynolds number based on radius b above which the circumferential velocity always decreases [48]:

$$Re_b = -\frac{b \cdot u_{rb}}{\nu_{turb}} \tag{7.5}$$

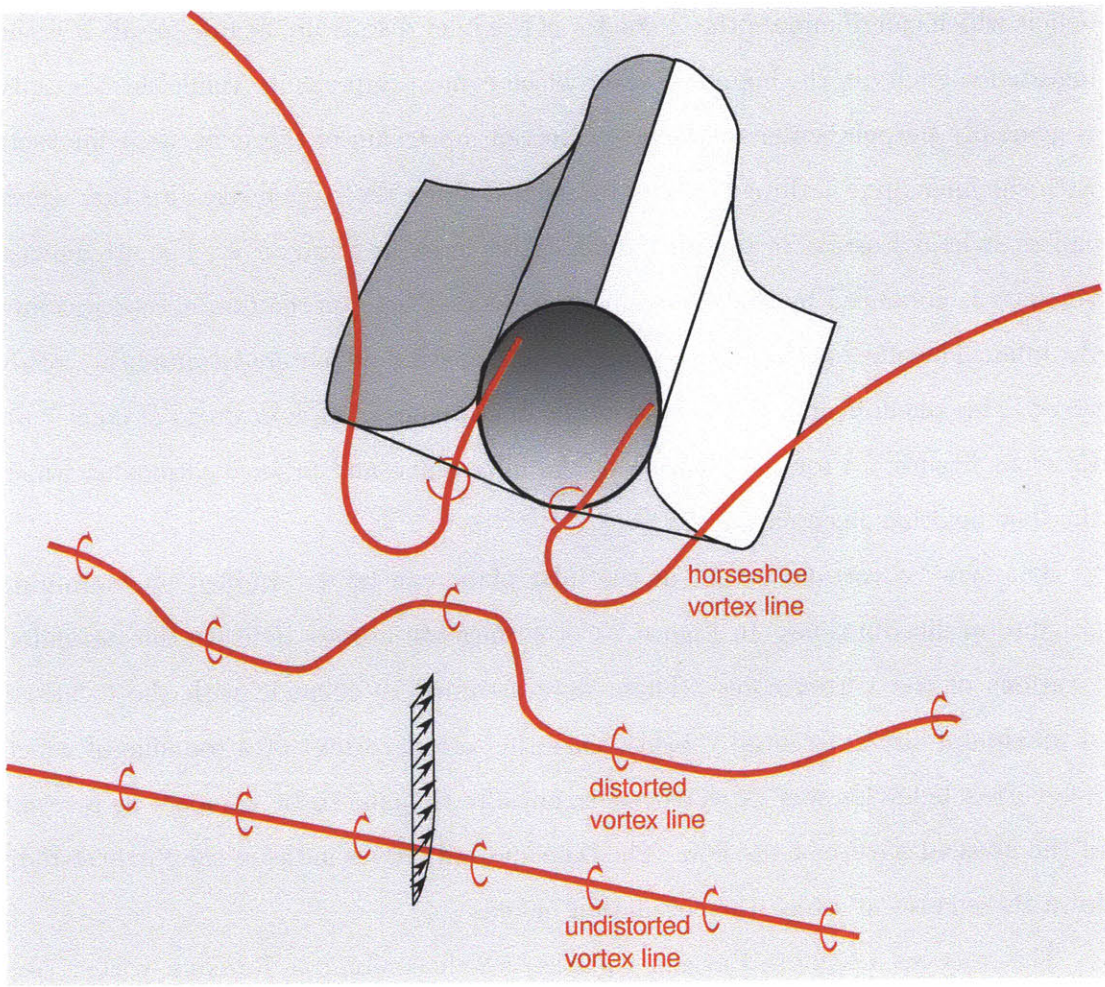

Figure 7-3: Generation and ingestion of streamwise vorticity due to boundary layer ingestion.

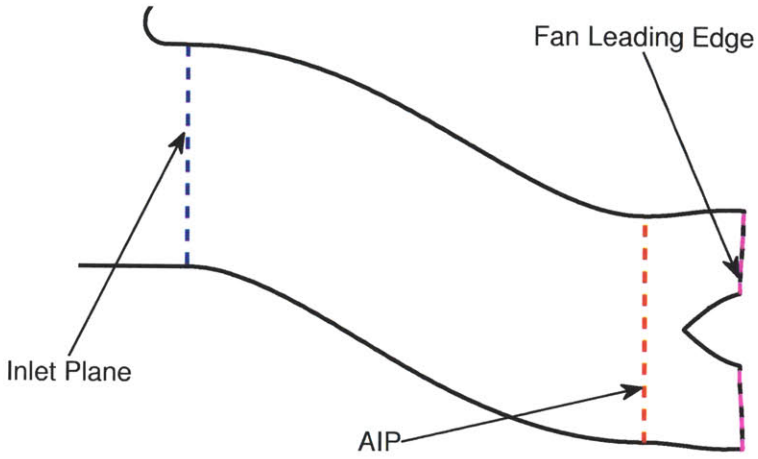

Figure 7-4: Schematic of serpentine duct symmetry plane showing cross-sectional locations of interest.

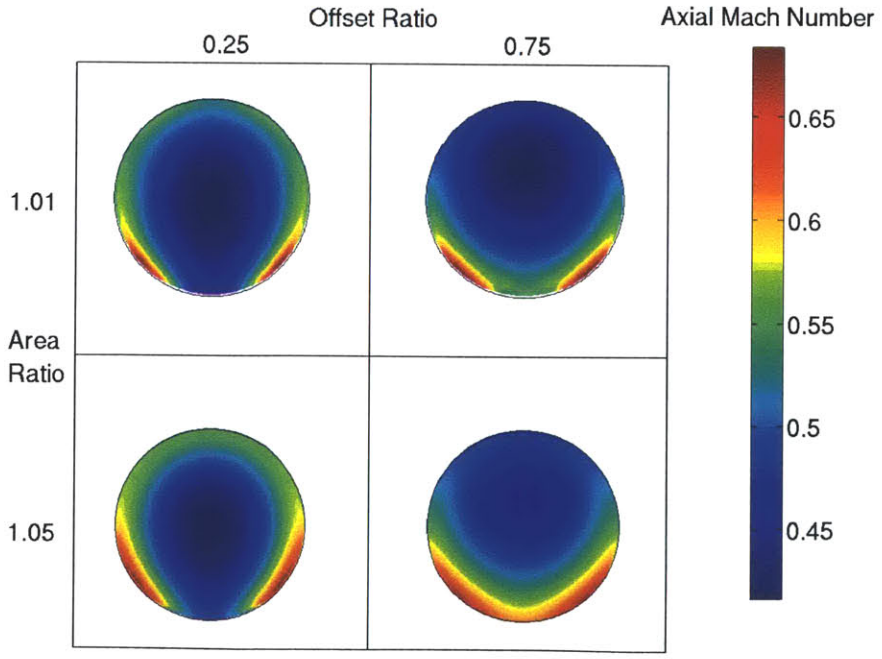

Figure 7-5: Axial Mach number at inlet plane, showing localized flow accelerations.

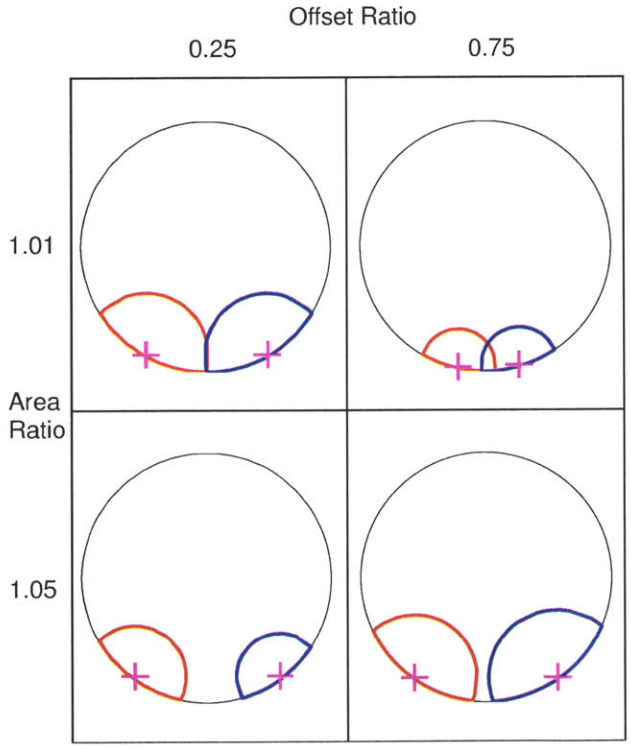

Figure 7-6: Red and blue: extent of vortices at upstream end of serpentine inlet; magenta crosses indicate locations of maximum circumferential velocity.

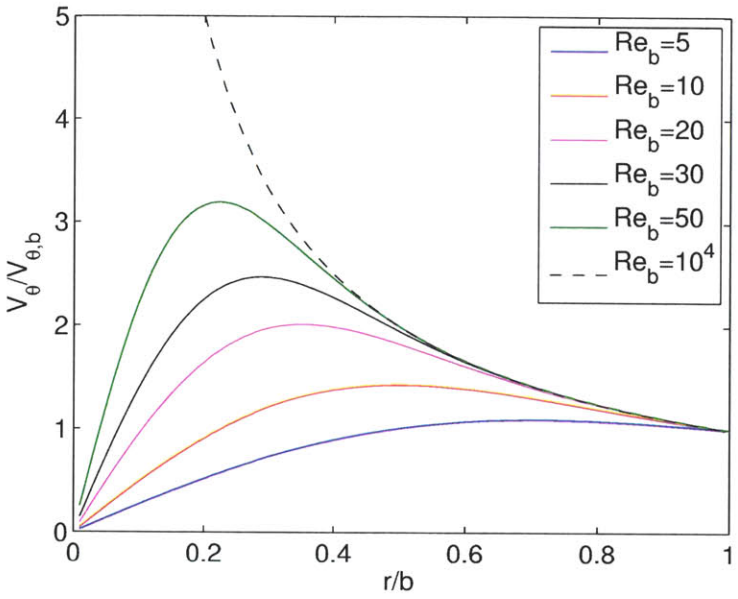

Figure 7-7: Burgers vortex non-dimensional circumferential velocity for a range of Reynolds numbers.

where u_{rb} is the radial velocity at radius b and ν_{turb} is the turbulent kinematic viscosity. For large Re_b, the Burgers vortex approaches the free vortex (potential flow solution) while for small Re_b it approaches a Rankine (forced) vortex, as depicted in Figure 7-7. To illustrate the discretization effects which cause the vortices to behave like viscous (small Re_b) Burgers vortices, the non-dimensional circumferential velocity distributions can be compared to the theoretical distribution for the Burgers vortex. These are plotted in Figures 7-8 to 7-11. The qualitative distributions in the four ducts resemble the Burgers vortex behavior of Figure 7-7 for Re_b between 5 and 20.

Though each duct's vortices are of a different size, the locations of the vortex cores are similar except for the duct with $AR = 1.01$ and $OR = 0.75$, for which they are closer together. From Figure 7-9, it is observed that the circumferential velocity distribution for this duct is in good agreement with the Burgers vortex for $Re_b = 18$, which is at least double the Re_b value associated with the distributions in the other three ducts. The behavior of this duct is qualitatively different than the other three in that the streamwise vortices lift off the duct bottom in the inlet. The consequences of this are investigated in the next subsection.

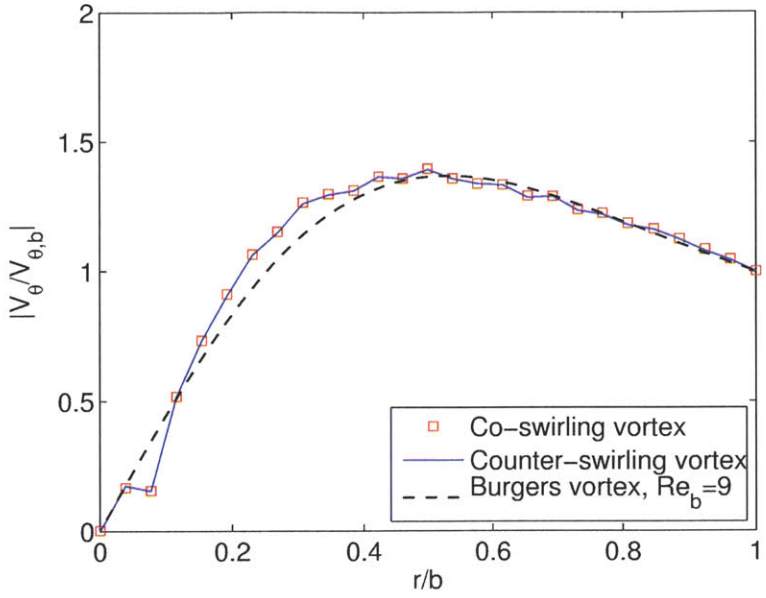

Figure 7-8: Non-dimensional local circumferential velocity vs. non-dimensional radius, $AR = 1.01$, $OR = 0.25$, compared to Burgers vortex for $Re_b = 9$.

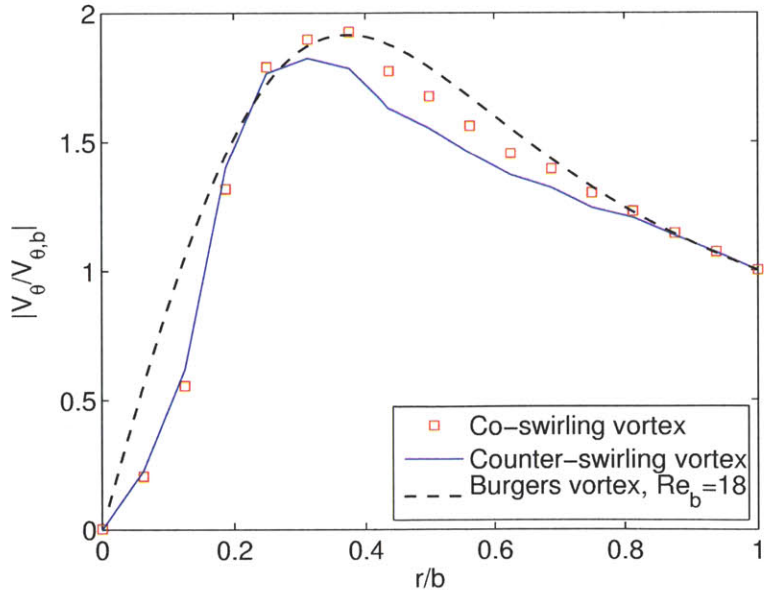

Figure 7-9: Non-dimensional local circumferential velocity vs. non-dimensional radius, $AR = 1.01$, $OR = 0.75$, compared to Burgers vortex for $Re_b = 18$.

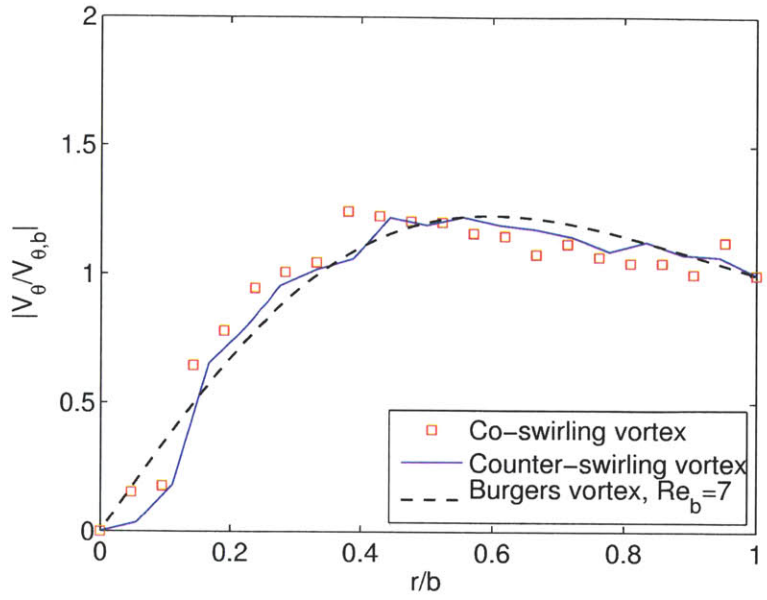

Figure 7-10: Non-dimensional local circumferential velocity vs. non-dimensional radius, $AR = 1.05$, $OR = 0.25$, compared to Burgers vortex for $Re_b = 7$.

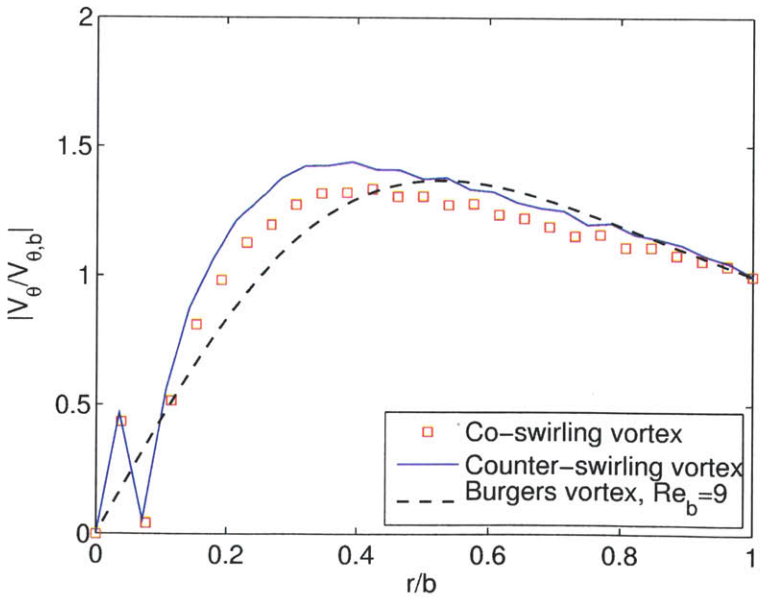

Figure 7-11: Non-dimensional local circumferential velocity vs. non-dimensional radius, $AR = 1.05$, $OR = 0.75$, compared to Burgers vortex for $Re_b = 9$.

7.3.2 Vortex Lift-Off

As noted above, an examination of the flow at the inlet planes of the four ducts revealed that the duct with $AR = 1.01$ and $OR = 0.75$ has more closely-spaced streamwise vortices than do the other three ducts. The reason is that this inlet contains a flow feature not found in the other three: the lift-off of the streamwise vortices. The mechanism leading to this vortex lift-off is investigated here. A combination of the local flow acceleration at the upstream end of the duct combined with the large normal pressure gradients in the duct bends is responsible for the lift-off.

Counter-rotating vortex pairs produce an induced velocity field which propels both vortices forward [49]. At the upstream end of the serpentine inlet, the streamwise vorticity originates from the bending of the boundary layer vortex lines around the inlet lip (horseshoe vortex formation). This produces a pair of counter-rotating vortices which will induce a velocity field resulting in upward motion of the vortices. For the inlets under consideration, this induced velocity is negligible since it is approximately two order of magnitude smaller than the mean duct velocity based on the known inlet diameter and corrected flow in the inlet. This enables the use of simple momentum arguments to explain the vortex lift-off phenomenon.

Assuming quasi-two-dimensional flow in the duct, the higher-velocity flow (from the vortex cores) will have a larger radius of curvature when subjected to the same mean duct pressure gradients than will the surrounding lower-velocity flow. This can be seen by examining the steady momentum equation normal to the flow direction for inviscid flow:

$$\partial p/\partial n = -\rho u^2/r_c \tag{7.6}$$

where r_c is the local radius of curvature. The concept is schematically illustrated in Figure 7-12. As the flow rounds the first bend in the duct, the normal pressure gradient turns the flow downward. The vortex cores are already at the duct bottom so the pressure gradient in this bend does not redistribute the flow. In the second bend, the pressure gradient turns the flow upward. The high-speed flow, which coincides with the vortex cores, has a larger radius of curvature compared to the mean flow when

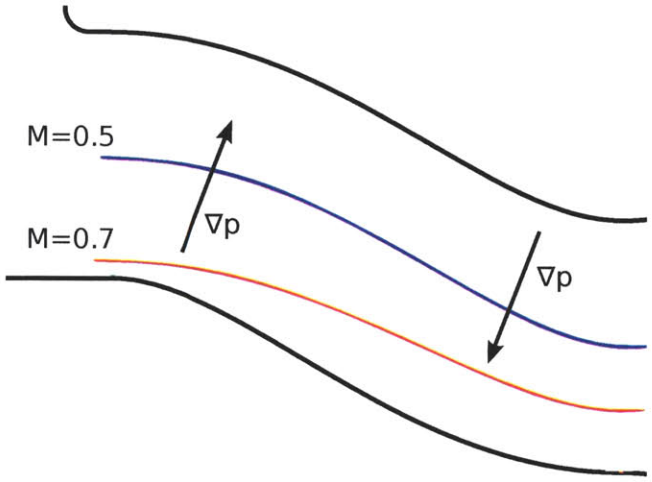

Figure 7-12: Vortex streamtube lift-off as a result of non-uniform incoming velocity.

subjected to the same pressure gradient. This results in the upward displacement of the vortex core streamlines. The amount of displacement depends on two factors: the magnitude of the normal pressure gradient (which itself depends on the duct offset) and the ratio of the vortex core velocity to the mean duct velocity.

Figure 7-13, which depicts the pressure coefficient on the duct symmetry planes, reveals that this vortex lift-off phenomenon is only present for the $AR = 1.01$, $OR = 0.75$ inlet. The lift-off can be seen more clearly in the blown-up view of this inlet given in Figure 7-14. The change in area ratio has only a modest effect on the mass-averaged Mach number at the upstream end of the duct (0.49 for $AR = 1.01$ and 0.51 for $AR = 1.05$), so that the key to the vortex lift-off lies with the peak axial Mach numbers on the inlet planes. The duct offset ratio is the primary factor which affects the vortex line stretching (and thus the peak axial Mach number) via the upstream influence of the overspeed on the bottom part of the first duct bend. The peak axial Mach number is increased from 0.61 for the ducts with $OR = 0.25$ to 0.69 ($AR = 1.01$) and 0.67 ($AR = 1.05$) for ducts with $OR = 0.75$. At this location, the flow is starting to turn downward due to the downstream serpentine duct, so the peak total Mach number also increases with the duct offset ratio, as can be seen in Table 7.1. The highest peak axial Mach number, combined with the lower mass-averaged Mach

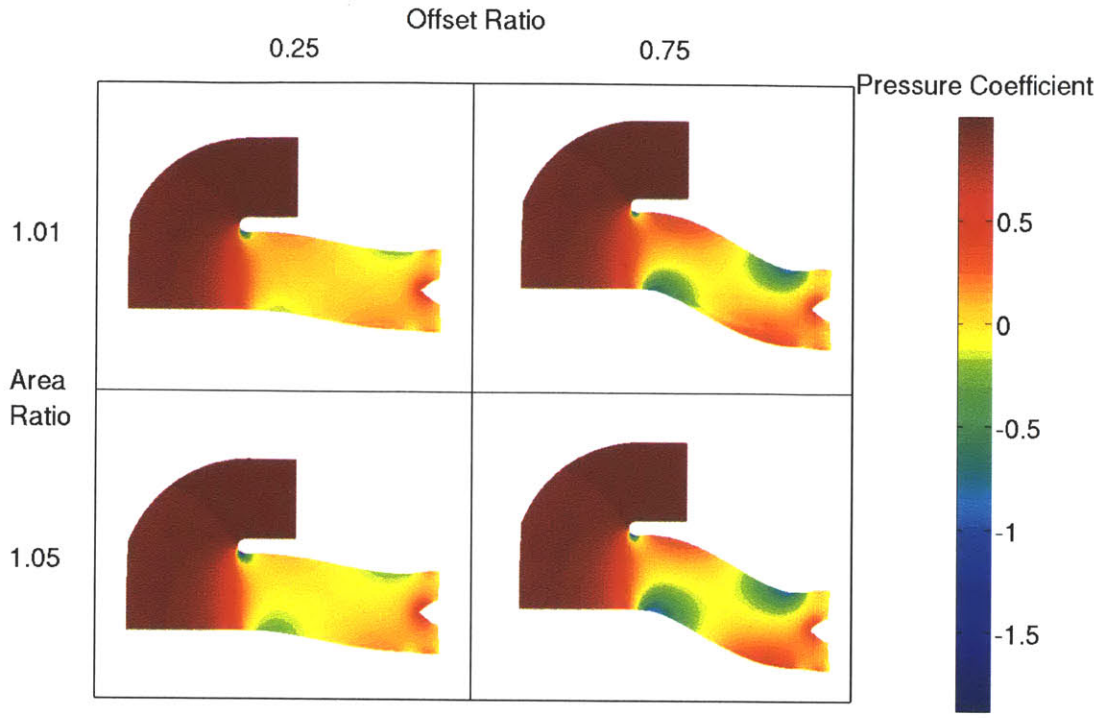

Figure 7-13: Compressible-flow pressure coefficient on duct symmetry planes.

Table 7.1: Peak Mach numbers on inlet planes.

AR \ OR	0.25	0.75
1.01	0.62	0.70
1.05	0.61	0.68

number for the $AR = 1.01$ ducts and larger normal pressure gradients present in the $OR = 0.75$ ducts, is responsible for the lift-off of the streamwise vortices. In the other ducts the pressure gradient and/or the ratio of peak axial Mach number to mass-averaged Mach number on the inlet plane are not large enough to produce a visible lift-off of the streamwise vortices, though the exact requirements for vortex lift-off to occur cannot be determined from this limited parametric study.

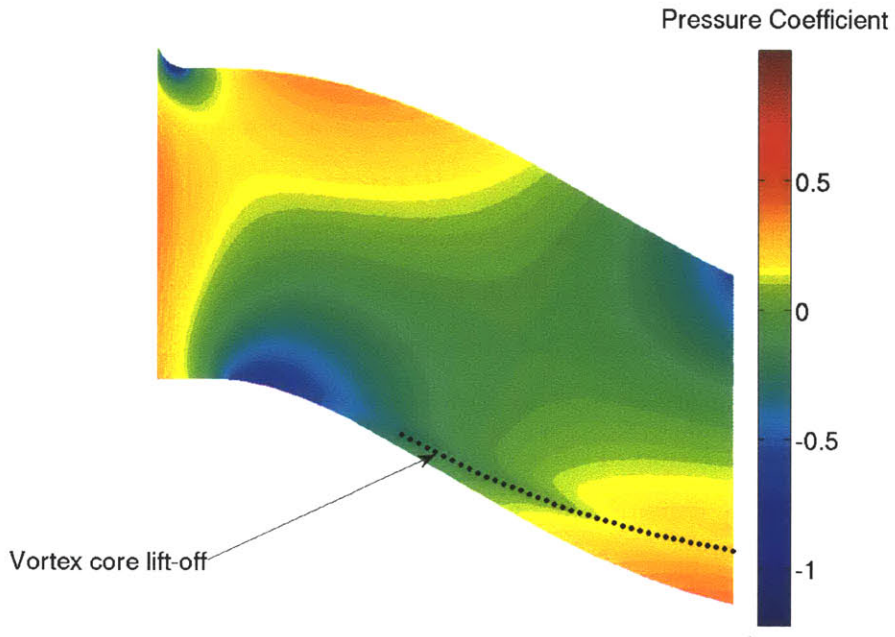

Figure 7-14: Compressible-flow pressure coefficient on duct symmetry plane for $AR = 1.01$, $OR = 0.75$, depicting the effects of vortex lift-off.

7.3.3 Fan Aerodynamics

The effects of the ingested streamwise vorticity on the flow at the AIP and fan leading edge are assessed to determine their impact on the fan performance. The three ducts without vortex lift-off have distortions at the AIP and fan similar to the serpentine inlet studied in Chapter 5. In contrast, in the $AR = 1.01$, $OR = 0.75$ duct the streamwise vorticity is concentrated near mid-span. Therefore swirl-type distortion affects fan behavior very differently than the stagnation-pressure type distortions which are dominant at cruise conditions.

A common metric for quantifying the degree of inlet distortion in a ducted flow is the $DC(60)$, which is defined as

$$DC(60) = \frac{\overline{p_t}^M - p^M_{t,avg.\ over\ worst\ 60°}}{\overline{p_t - p}^M} \tag{7.7}$$

This metric quantifies magnitude and the localization of stagnation pressure distor-

tion. For a given stagnation pressure deficit, a higher $DC(60)$ value indicates that the stagnation pressure distortion is concentrated over a circumferential region approaching 60° pitchwise extent. For inlet distortion at cruise conditions, Madani & Hynes [24] reported $DC(60)$ values at the AIP ranging from 0.414 to 0.625 depending on the duct geometry. Table 7.2 lists the computed $DC(60)$ values at the AIP and fan leading edge for the current study. While the duct with lifted-off streamwise vortices has $DC(60)$ values approximately 2-3 times higher than those of the other ducts, all the values in the table are at least an order of magnitude smaller than the results obtained by Madani & Hynes. This indicates that swirl distortion due to the presence of streamwise vorticity is more dominant than the stagnation pressure deficit for the low-speed free-stream conditions used in this work.

Conditions at the fan are only weakly dependent on duct geometry if vortex lift-off does not occur. The lift-off shifts the effects of the distortion away from the outer span, altering the flow field near the fan in the region where the rotor shocks are generated. The details of the changes to the flow field at the fan are explained in detail below.

The three ducts without vortex lift-off have similar flow fields at the fan leading edge (Figures 7-15 and 7-16), with streamwise vortices impacting the fan at the outer radius in the bottom portion of the duct, while for the $AR = 1.01$, $OR = 0.75$ duct the lifted-off streamwise vortices are located near mid-span at the fan. The vortices impacting the fan alter the local operating point of the blade row by changing the incoming relative Mach number and the incidence angle of the flow onto the blades, as schematically illustrated in Figure 7-17. This effect is quantitatively depicted at the outer radius in Figures 7-18 and 7-19. In these figures 0° along the abscissa is the location of the bottom center of the duct. The regions of subsonic and enhanced supersonic relative flow near the duct bottom (above 300° and below 50°) are due to the streamwise vortices.

The duct in which the vortex lift-off phenomenon occurs (shown in red) does not exhibit a strong increase in relative Mach number in this region due to the displacement of the counter-rotating vortex away from the end wall. The variations in the

Table 7.2: $DC(60)$at AIP and fan leading edge for parametric study.

Duct	AIP	Fan leading edge
$AR = 1.01$, $OR = 0.25$	0.009	0.008
$AR = 1.01$, $OR = 0.75$	0.017	0.013
$AR = 1.05$, $OR = 0.25$	0.006	0.004
$AR = 1.05$, $OR = 0.75$	0.007	0.004

relative Mach number in the remainder of the circumference are due to the redistribution of flow caused by the swirl distortion. It is observed in Figure 7-19 that the incidence angle distribution is more symmetric about the top-center of the duct (180°) than is the relative Mach number distribution. This is a result of the nearly-constant stagnation pressure of the incoming flow (pressure recovery is >99%), which requires increases to the incoming circumferential Mach number to be balanced by decreases in the axial Mach number and vice-versa. The changes in axial Mach number, which varies from 0.36 to 0.44, are dominant in shaping the incidence angle distribution. The reason for this is that the mean relative circumferential Mach number (dominated by the wheel speed) is larger than the mean axial Mach number (0.91 compared to 0.41). The change in axial Mach number owing to swirl distortion is symmetric because the sign of the swirl is irrelevant. Given an (approximately) constant stagnation pressure, swirling the flow will reduce the axial Mach number by the same amount regardless of the swirl direction (for a given stagnation-to-static pressure ratio). Thus the approximately symmetric incidence angle distribution of Figure 7-19 is obtained.

The key impact effects of swirl distortion on the fan aerodynamics are changes to the relative Mach number and incidence angle distributions. For the ducts without vortex lift-off, theses changes are most pronounced in the outer span. The effect of vortex lift-off is to migrate these changes towards mid-span.

7.4 Acoustics

We now link the changes in MPT noise generation and propagation to flow distortion features and assess the source noise generation, the far-field noise, and the in-duct

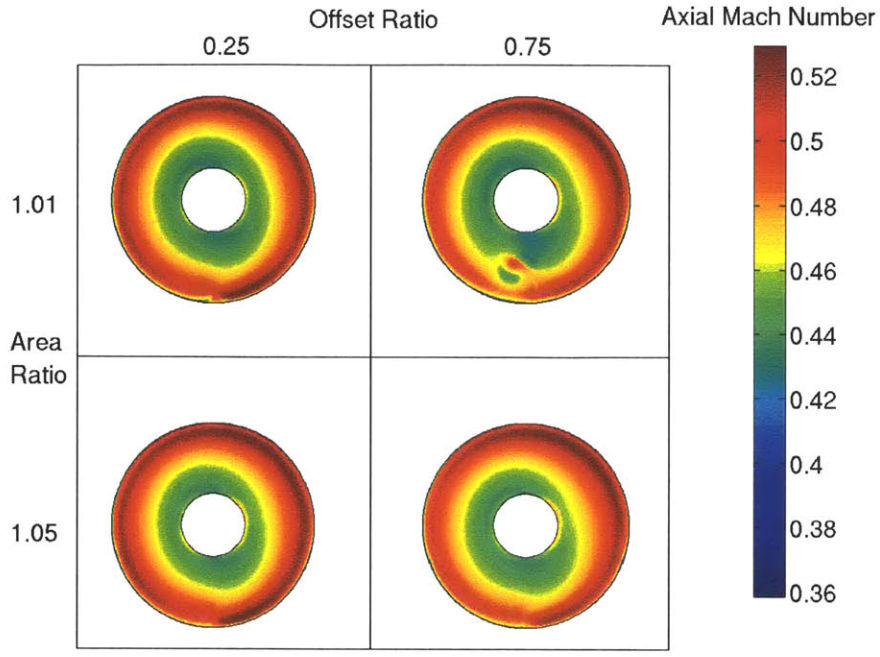

Figure 7-15: Axial Mach number at fan leading edge, emphasizing the displacement of the swirl distortion towards mid-span due to vortex lift-off.

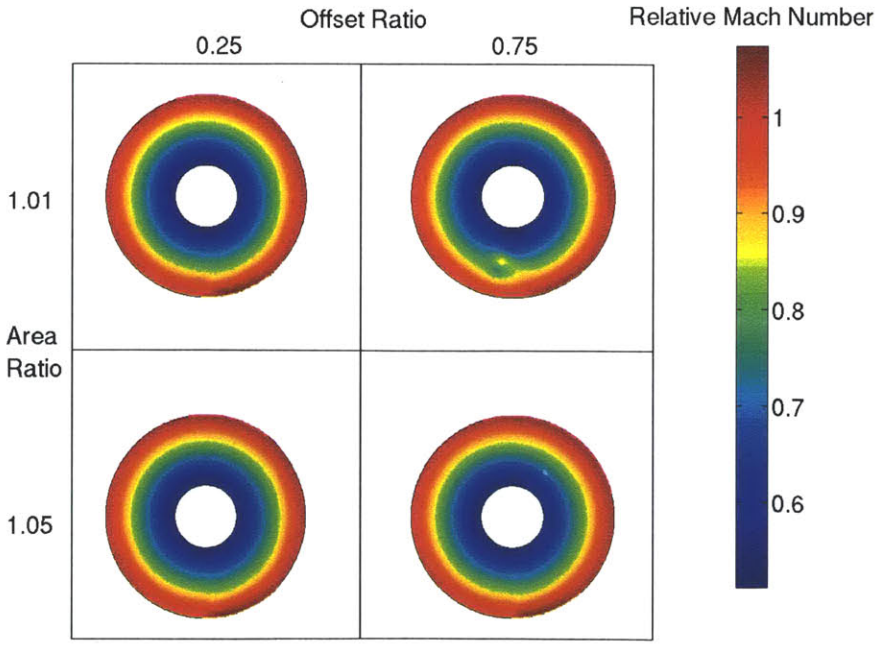

Figure 7-16: Relative Mach numbers at fan leading edge, emphasizing the displacement of the swirl distortion towards mid-span due to vortex lift-off.

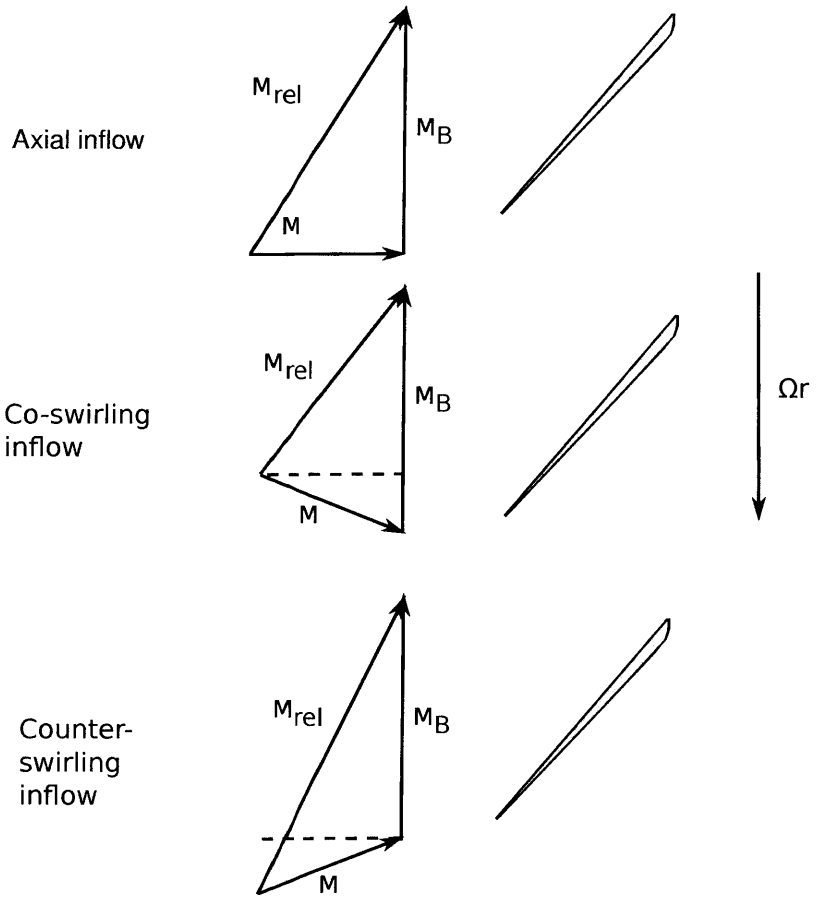

Figure 7-17: Schematic illustration of the effect of swirl distortion on the relative Mach number incident to a blade row, showing the decrease due to co-swirl and the increase due to counter-swirl.

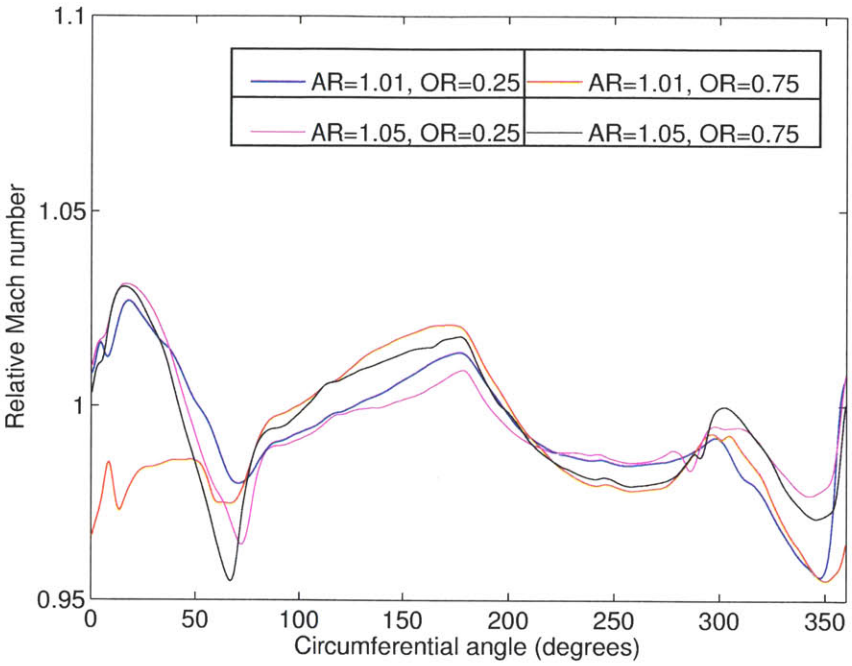

Figure 7-18: Relative Mach number vs. circumferential angle at outer radius (casing). The increase and decrease due to counter- and co-swirl, respectively, can be seen at angles above 300° and below 50°.

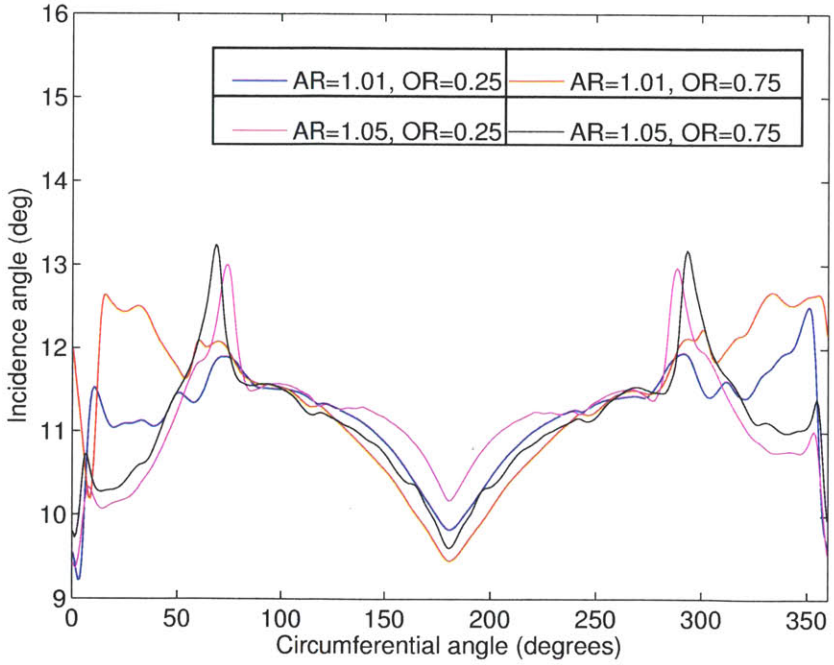

Figure 7-19: Incidence angle vs. circumferential angle at outer radius (casing).

propagation. It is found that the source noise does not vary with duct geometry and it is the ingested streamwise circulation which determines the change in source strength relative to the conventional axisymmetric inlet case. The changes in far-field spectra are predominantly caused by a combination of in-duct attenuation for short wavelengths and the non-uniform external flow. The far-field directivity is affected by the presence of in-duct vortex lift-off, though the mechanism responsible for this is not clear. The far-field overall noise levels increase with the duct area ratio since the higher axial Mach numbers which occur at the inlet plane as a result of increasing the area ratio allow more acoustic energy to propagate to the far-field. The in-duct sound power attenuation is reduced by 9 dB in the presence of lifted-off streamwise vortices as the counter-swirling vortex decreases the attenuation rate of cut-off waves near mid-span.

7.4.1 Noise Source Generation

The noise source is characterized by the sound power level at the fan leading edge. The sound power is computed by integrating the local sound intensity as described in Chapter 6. The sound power is increased as a result of incidence angle changes due to swirl distortion. This is illustrated schematically in Figure 7-20. For low-speed free-stream flows, the stagnation pressure deficit within the boundary layer is less than 1% of the free-stream value. In this situation, the ingestion of streamwise vorticity is more important than the distortion transfer within the serpentine inlet duct. This conclusion is supported by the analysis of Section 5.4 which showed that at the BPF, there is little change in the fan pressure field due to once-per-revolution distortion when the variation in incoming stagnation pressure is negligible. The location of the streamwise vortices can change as a result of altering the duct geometry, but the impact on the fan leading edge acoustic field is negligible since the acoustic energy is concentrated at the blade-passing frequency, as can be seen in Figure 7-21.

The frequency spectra over the whole fan face cross-section in Figure 7-21 therefore display a lack of sensitivity to the inlet duct parameters. The overall sound power level (for frequencies up to and including the BPF) for all the four ducts is 159 dB.

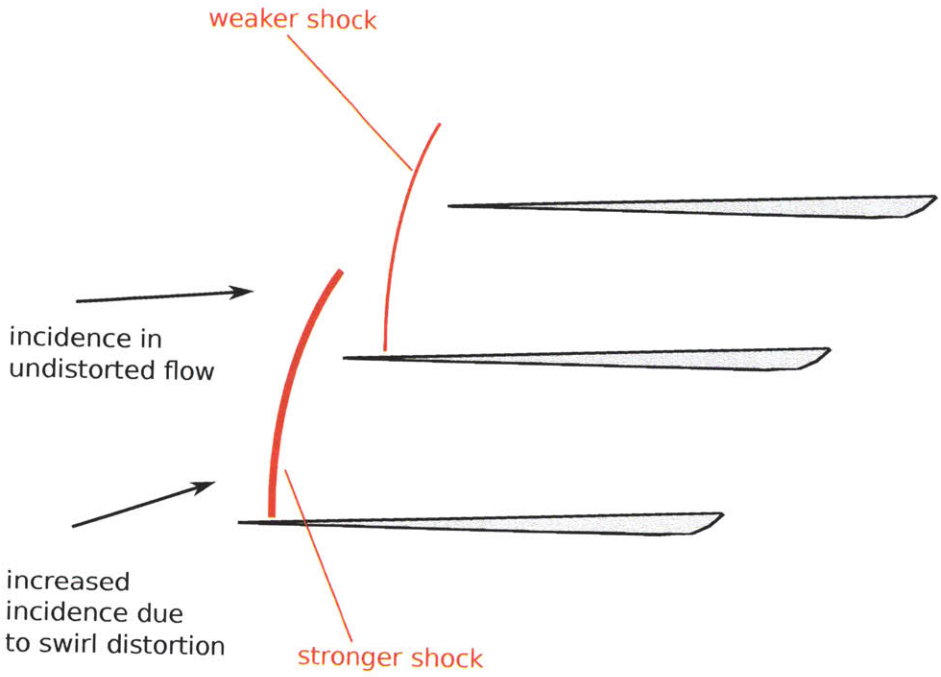

Figure 7-20: Schematic illustration of increase in shock strength due to incidence angle changes caused by swirl distortion.

This indicates that the distortion transfer within the inlet duct, even in the presence of streamwise vortex lift-off, has little effect on source noise.

7.4.2 In-Duct Propagation

This subsection discusses the effect of swirl distortion on sound power propagation within the serpentine inlets of the parametric study. There are two distinct cases to consider depending on the location of the streamwise vortices: the swirl distortion can either be concentrated in the outer span or can be shifted towards the duct centerline by vortex lift-off. Swirl distortion in the outer span primarily alters the sound power by attenuating high frequencies, while this effect is reduced when the distortion is concentrated near mid-span.

First consider the effect of the distortion being located in the outer span, as illustrated in the left side of Figure 7-22. Based on the insight gained from the investigation of the SAX-40 inlet in Chapter 5, the key mechanism responsible for altering the in-duct propagation (relative to uniform inflow) in the presence of swirl

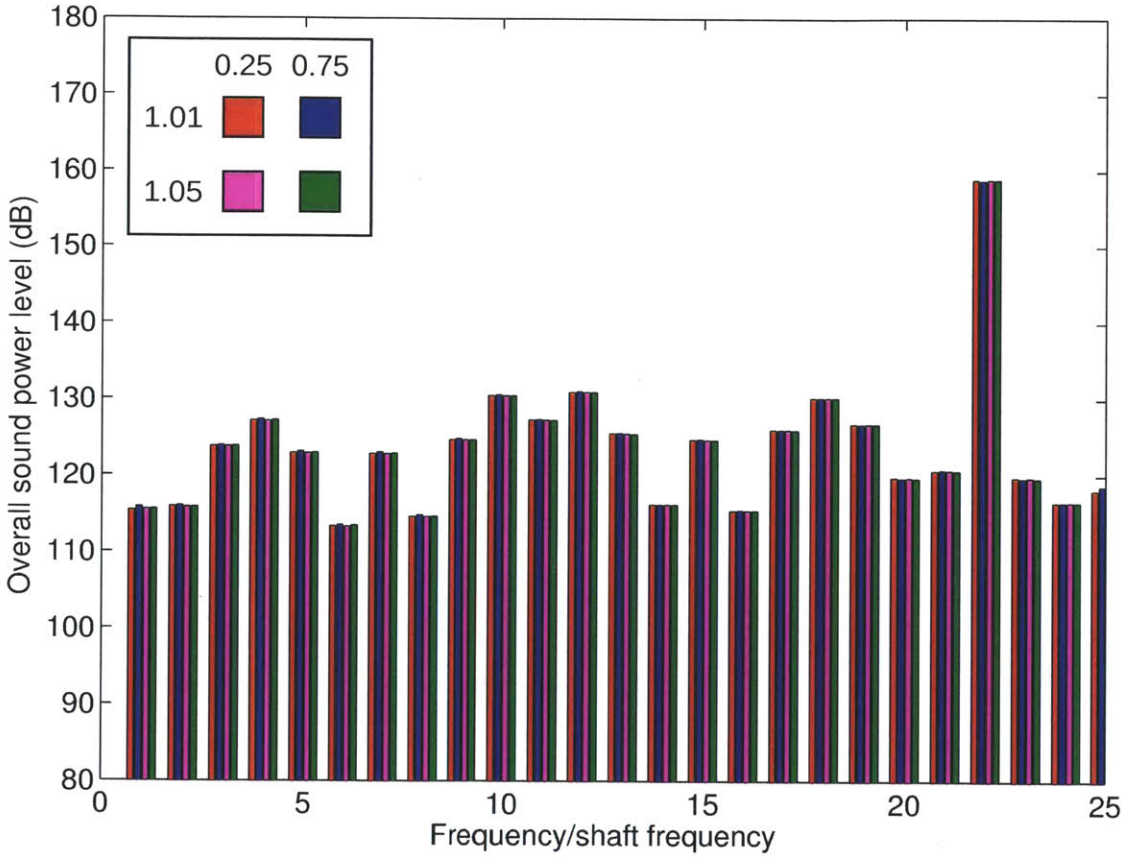

Figure 7-21: Sound power spectra at the fan leading edge, showing the independence of source noise on duct geometry.

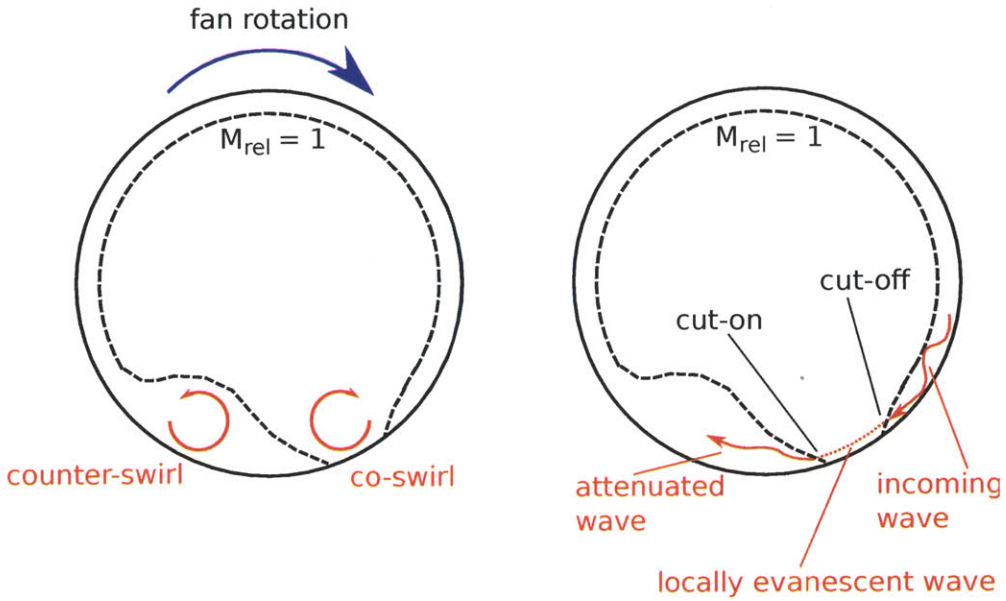

Figure 7-22: Wave attenuation by co-swirling streamwise vortex in the outer span.

distortion is the creation of a region of evanescent wave behavior by the co-swirling vortex as it lowers the relative Mach number below sonic. As waves pass through this region they decay but continue to propagate as illustrated in the right part of Figure 7-22. The result is enhanced attenuation compared to the undistorted inflow case. This mechanism affects wavelengths on the order of the length of the subsonic relative flow region more strongly than wavelengths on the order of the circumference.

Next consider lifted-off streamwise vortices. The left part of Figure 7-23 illustrates the effect of this phenomenon on the flow. The counter-swirling vortex increases the local relative Mach number near mid-span. The result is that cut-off waves passing through this region have reduced rates of decay. This is represented by the right part of Figure 7-23. This effect will also be concentrated on short wavelengths (higher frequencies) in a manner similar to the outer-span vortex case.

The cumulative effect of waves spiraling upstream through the inlet with vortex lift-off is the enhancement of the sound power through the duct, as shown in Figure 7-24. The average decay from the AIP to the upstream inlet plane for the three ducts without vortices in the outer span is 21.7 dB. Between the same two locations for the remaining duct, the decay is only 14.6 dB, resulting in a 7.1 dB enhancement in the

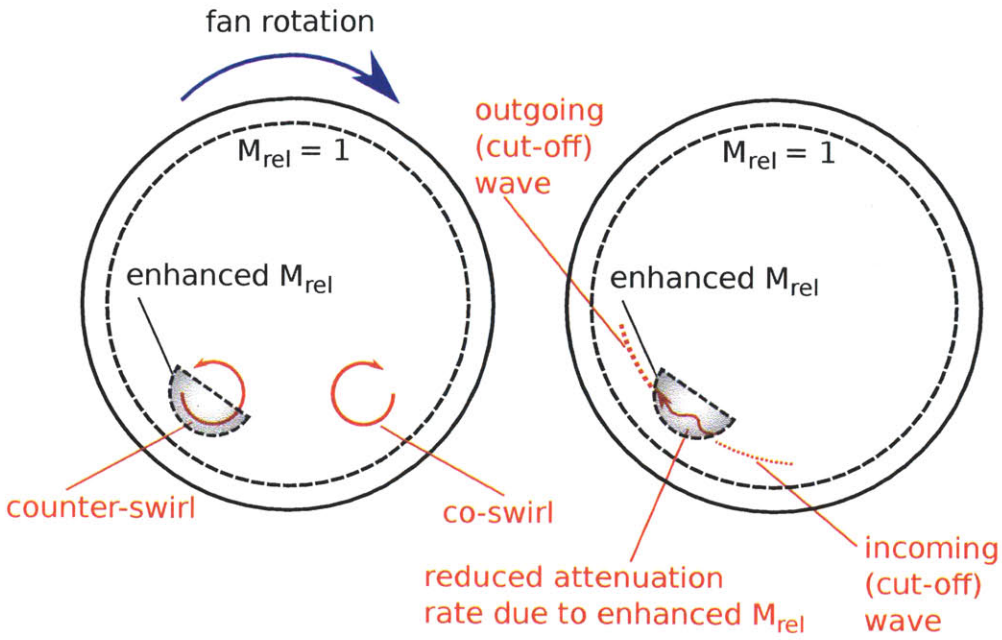

Figure 7-23: Reduction in sound power decay rate due to counter-swirling, lifted-off streamwise vortex.

sound power propagated through the serpentine portion of the inlet. The reduced decay for the $AR = 1.01$, $OR = 0.75$ duct is also visible from the fan leading edge to the AIP, such that at the upstream end of the inlet this duct has an overall sound power level 9.3 dB higher than the average values for the other three ducts. This is a significant increase as this indicates an enhancement of the propagating acoustic energy by a factor of 8.

The overall sound intensity fields support the explanation that it is the region around the counter-swirling vortex which is responsible for the enhanced sound power. Figure 7-25 depicts the overall sound intensity fields at the AIP. The feature which differentiates the sound intensity fields is the region where the streamwise vortices are lifted off, near mid-span for the $AR = 1.01$, $OR = 0.75$ inlet. Local intensity enhancement of 20 to 30 dB compared to the other ducts is observed. As the streamwise vortices move towards the duct bottom at the inlet plane, the enhanced sound intensity region migrates as well. Figure 7-26 reveals that this enhancement is carried forward through the entire inlet.

The enhanced decay of short wavelengths due to outer-span swirl distortion as

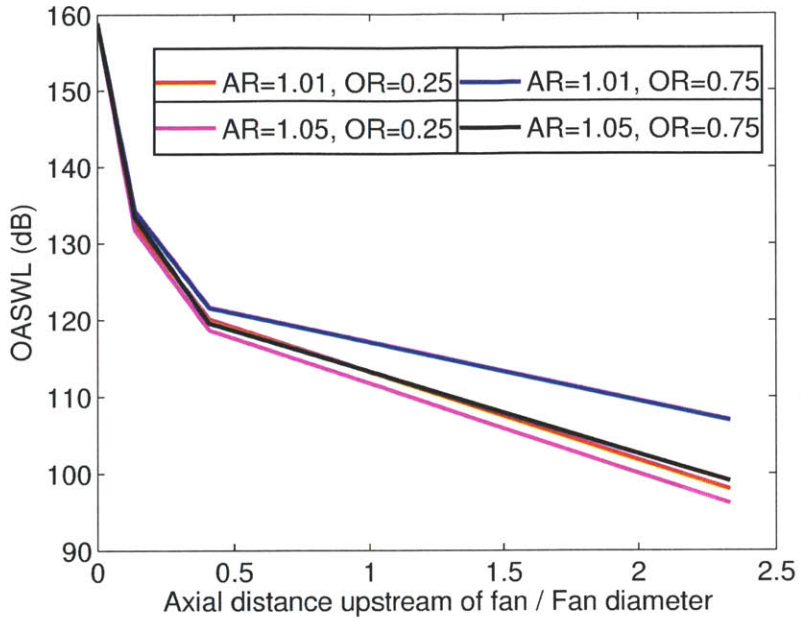

Figure 7-24: In-duct overall sound power level (up to and including the blade-passing frequency) evolution, showing the enhancement in sound power resulting from vortex lift-off.

well as the enhanced propagation of these same wavelengths due to vortex lift-off are exemplified by the instantaneous snapshots of unsteady pressure on the duct symmetry plane of Figure 7-27. The frequencies most affected are those between one-half BPF and BPF. This is seen by comparing the frequency spectra at the AIP and inlet plane locations, depicted in Figures 7-28 and 7-29. The spectra at the AIP are qualitatively similar to those at the fan leading edge, though comparison with Figure 7-21 reveals that there is decay from the fan to the AIP of up to 37 dB. In contrast, the spectra at the inlet plane show increased attenuation of the high-frequency tones, particularly the blade-passing tone. For the duct with vortex lift-off ($AR = 1.01$, $OR = 0.75$), the 9 dB increase in overall sound power is concentrated at frequencies of 13 to 20 times the shaft frequency.

7.4.3 Far-Field Propagation

In the far-field, the spectra obtained are qualitatively similar to those obtained for the SAX-40 inlet studied in Chapter 5. The full-scale sound pressure level spectra

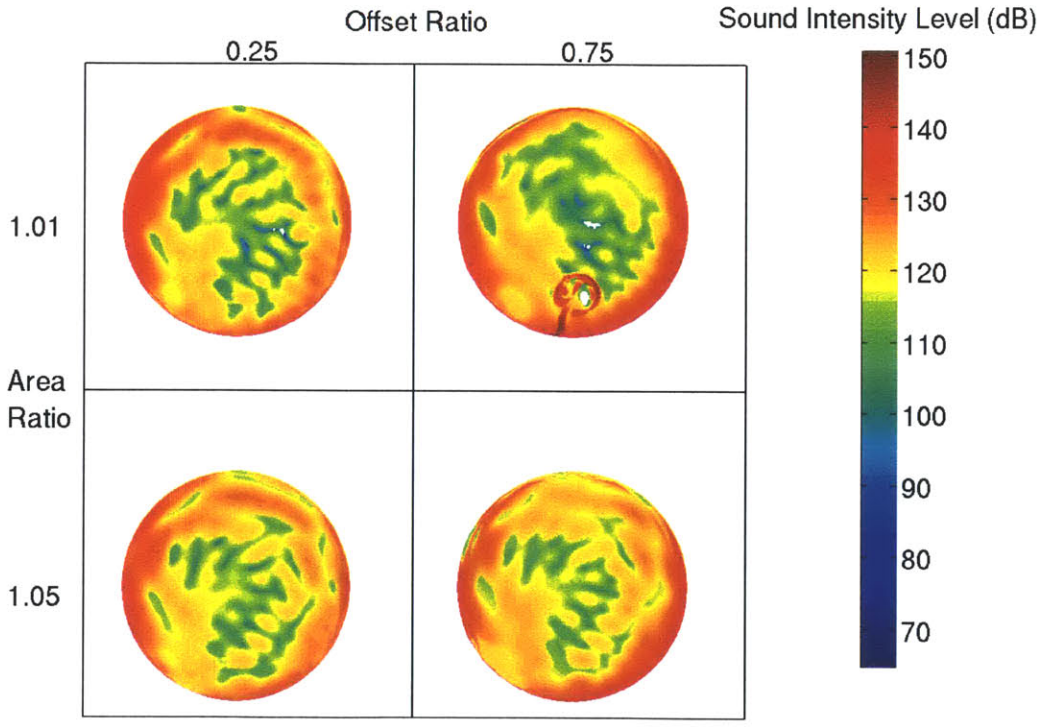

Figure 7-25: Overall sound intensity fields (up to and including the blade-passing frequency) at AIP.

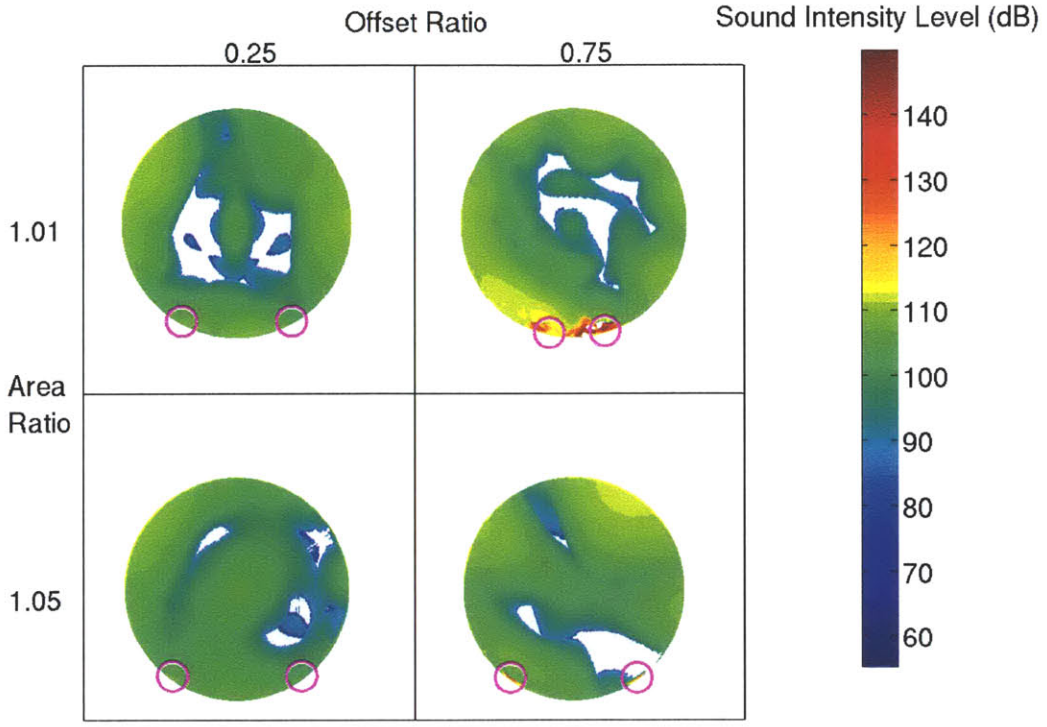

Figure 7-26: Overall sound intensity fields (up to and including the blade-passing frequency) at the duct inlet; magenta circles indicate locations of maximum/minimum circumferential velocity used to identify vortex cores in Section 7.3.

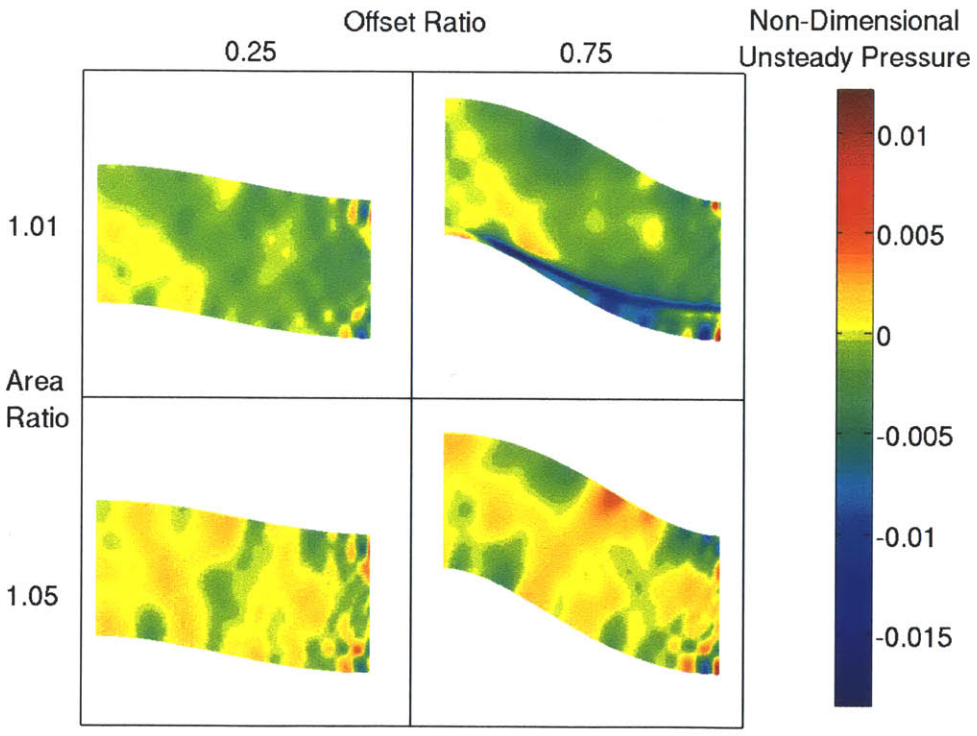

Figure 7-27: Instantaneous unsteady pressure (normalized by AIP dynamic pressure) on duct symmetry planes.

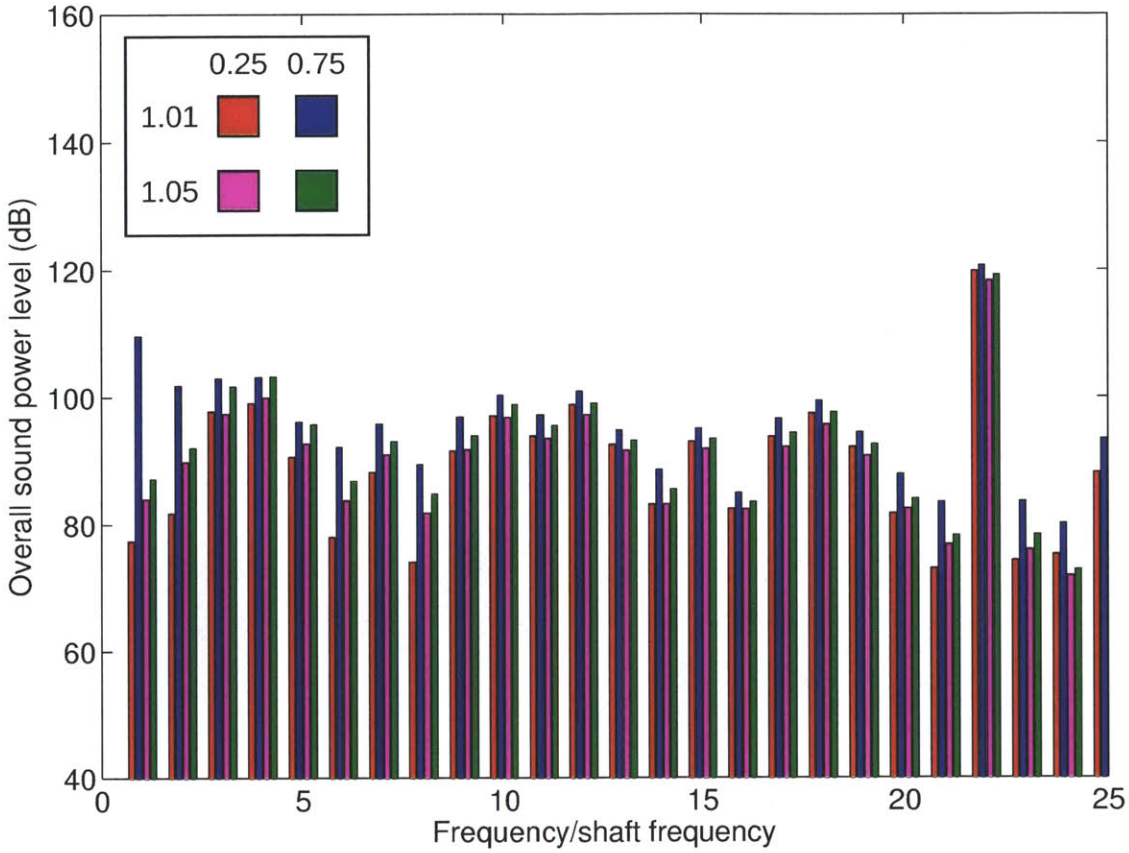

Figure 7-28: Sound power spectra at AIP, showing enhanced sound power for $AR = 1.01$, $OR = 0.75$ duct.

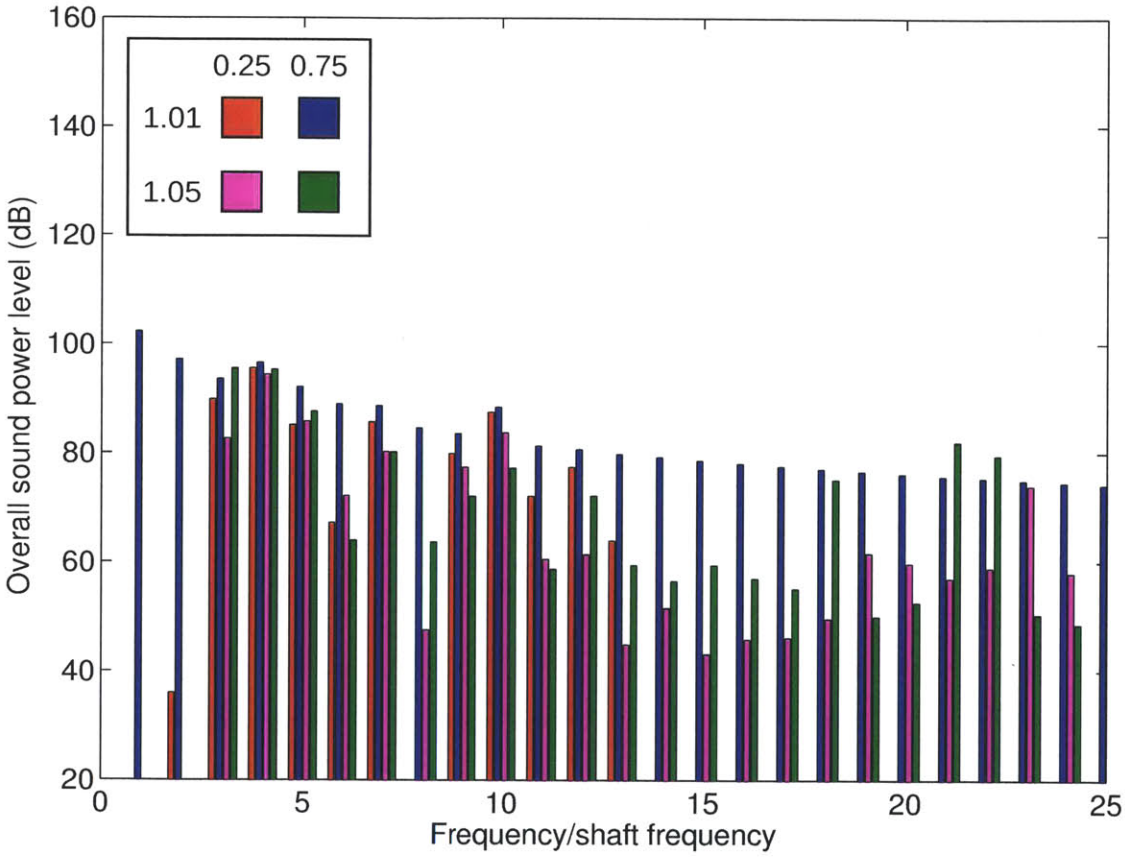

Figure 7-29: Sound power spectra at inlet plane, showing regions of enhanced sound power due to vortex lift-off (blue bars).

of Figure 7-30 share the common characteristic of an apparent cut-off of tones above a critical frequency. Given the spacing of the tones (typically 2-3 shaft orders), it is unclear whether the observed variations in apparent cut-off frequency are significant. It may simply be that the highest frequency at which a tone is present below cut-off differs for each duct. The apparent cut-off frequency is thus approximated as one-half of the BPF, and is not affected by the serpentine duct geometry. The inlets with area ratios of 1.05 have higher noise floors than the inlets with area ratios of 1.01. This may be related to the increased flow non-uniformities outside the inlet for the $AR = 1.05$ ducts, but the numerical mechanism is not yet well-understood. This could be explored in future work.

The apparent cut-off in the far-field is not an artifact of levels falling below the numerical noise floor, as the attenuation due to spherical spreading is insufficient to produce such a result. This can be shown via analysis of the frequency dependence of the spherical wave spreading relationship in uniform flow. The power carried by a radially-propagating spherical wave is given by

$$p'v' = (p')^2 \frac{\sqrt{1 + \left(\frac{\bar{a}}{\omega r}\right)^2}}{\bar{\rho}\bar{a}} \tag{7.8}$$

The distance from the inlet plane to the FW-H integration surface in the computations is approximately 1.5 fan diameters. At this distance, the frequency dependence of the power (which scales in the same way as does the sound pressure) is given in Figure 7-31. The BPF tone is only attenuated by 0.25 dB more than the fan shaft frequency. The apparent cut-off cannot therefore be attributed to spherical spreading effects.

The 9 dB enhancement in sound power at the inlet plane for the $AR = 1.01$, $OR = 0.75$ duct is not evident in the far-field because the additional acoustic energy is concentrated at frequencies above one-half of the blade-passing frequency. The implication is that the non-uniform flow outside the duct is responsible for the cut-off of the high-frequency tones, including the blade-passing frequency. Since this external flow is largely unchanged for all the boundary layer-ingesting inlet computations conducted in this research, it follows that there is no significant change in the far-

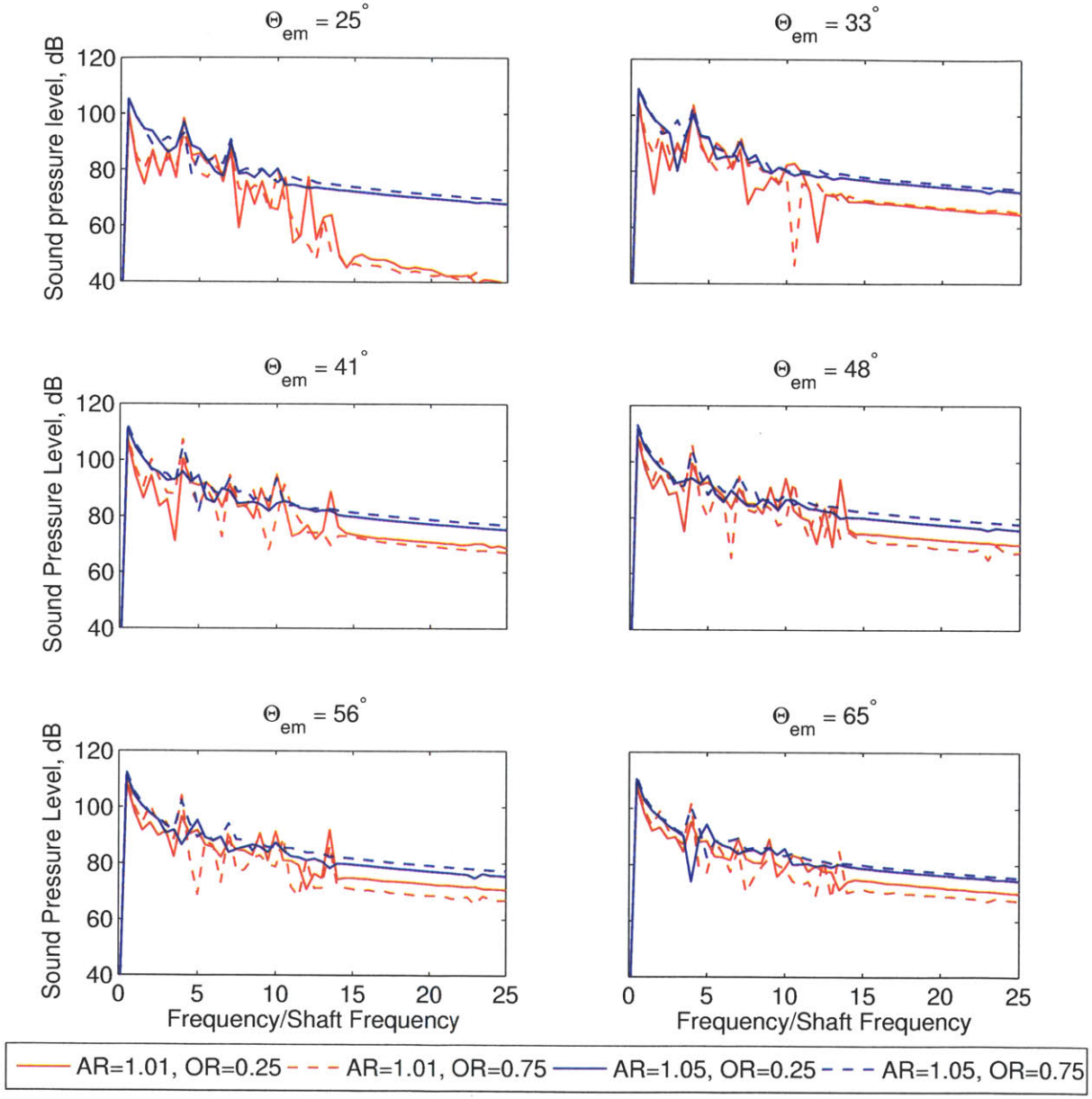

Figure 7-30: Far-field spectra at various emission angles (BPF is at $f/f_{shaft} = 22$).

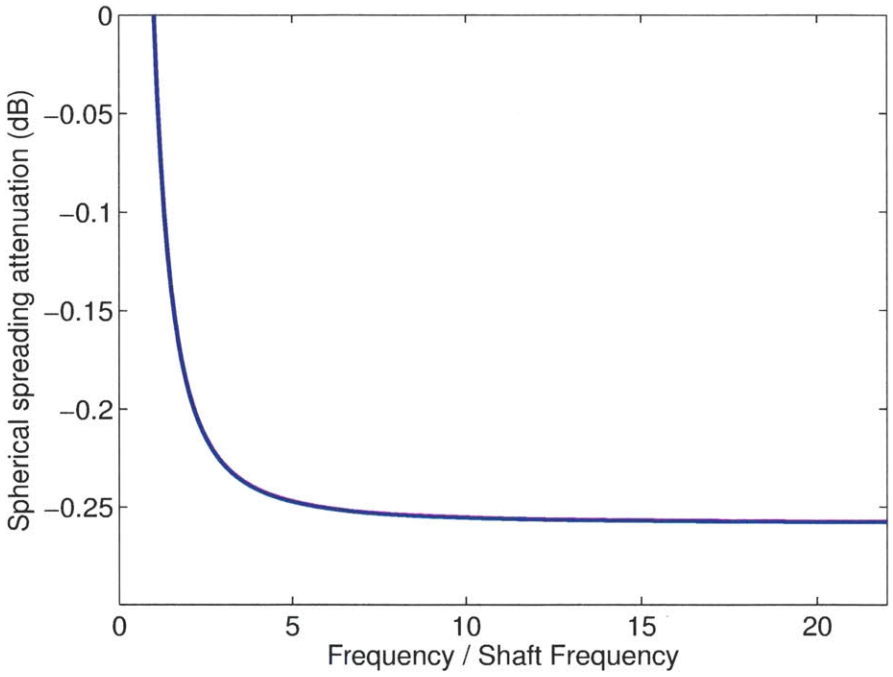

Figure 7-31: Frequency dependence of SPLs for spherically-spreading waves at 1.5 fan diameters from the inlet plane.

field apparent cut-off frequency between the various ducts. To establish the link between the external flow and the far-field cut-off frequency, computations in which the stagnation point on the nacelle is varied could be carried out.

7.4.3.1 Changes Relative to Conventional Inlet To Quantify the Impacts of Swirl Distortion of Far-Field MPT Noise

The changes in far-field noise relative to the conventional inlet results are analyzed to determine the effects of duct geometry on the peak far-field levels and directivity. The takeaways are that (1) the peak overall sound pressure level (OASPL) is increased between 13.2 and 17.9 dB for the four inlets considered, with 3.8 dB of this 4.7 dB range attributed to the change in area ratio as a result of changes in the external flow; and (2) the directivity is primarily affected by vortex lift-off, though the mechanism responsible is not fully understood.

The peak change in level relative to the conventional inlet is dependent upon the inlet geometry. For the four inlets studied, this peak occurs at $\Theta_{em} = 33°$. Table 7.3

Table 7.3: Peak change in OASPL (in dB) relative to conventional inlet.

AR \ OR	0.25	0.75
1.01	13.2	14.2
1.05	17.1	17.9

gives the numerical values of these peaks. The area ratio has a stronger effect on the peak change in level (3.8 dB on average) than does the duct offset ratio (at most ± 0.5 dB) because changing the area ratio alters the external flow. Since the corrected flow through the inlets is unchanged from one duct to the next, the accelerations required in the streamtube contraction region outside the inlet increase with AR.

Focusing on the directivity, the OASPLs are plotted in Figure 7-32 after having subtracted the peak value from each curve. Relative to the other three cases, the duct with $AR = 1.01$, $OR = 0.75$ has a steeper slope at emission angles below 33° and a higher value of approximately -2 dB for emission angles greater than 37°. The mechanism leading to this change in directivity is not yet fully understood. Performing further computations to obtain different results with vortex lift-off may reveal the scaling for these directivity changes.

Adjusting the serpentine inlet spectra for the peak changes in OASPL and the changes in directivity relative to the conventional inlet results isolates the changes in the spectrum as shown in Figure 7-33. To enable an overall assessment of the change in far-field spectrum, the average change in spectrum is computed and is displayed in red in Figure 7-34. At frequencies above one-half of BPF (black dashed line) the far-field noise is completely cut-off for the serpentine inlet cases. A simplified representation of the changes in spectra is given by the blue line in the figure. This will be used to formulate a response surface correlation in the next chapter.

7.5 Summary of Parametric Study Results

A parametric study of serpentine inlet designs was conducted, in which the duct area ratio and offset ratio were varied while keeping the ingested boundary layer, fan

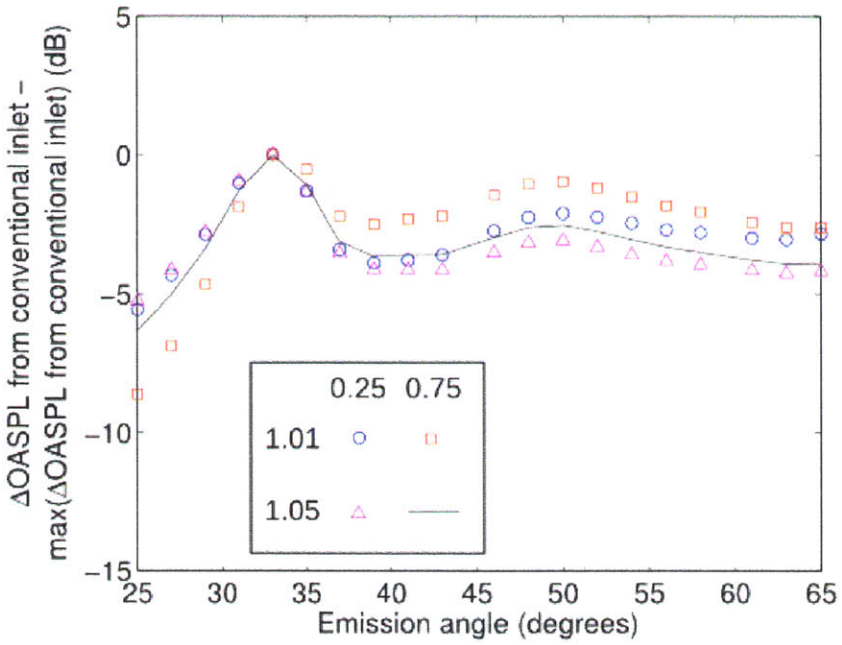

Figure 7-32: Change in directivity (relative to peak level) compared to conventional inlet result.

corrected flow, and body-force-based fan model constant.

The interaction of the boundary layer vorticity and the inlet lip results in horseshoe vortex formation and the ingestion of streamwise vorticity into the inlet. The nature of the vortices has been investigated. The rotational velocity fields are well-represented by viscous Burgers vortices. This is attributed to the coarse discretization, which affects the flow field similarly to viscosity in a real flow, spreading out the Rankine vortex core even in inviscid flow.

The internal flows for the four ducts studied are primarily differentiated by the presence of vortex lift-off for the $AR = 1.01$, $OR = 0.75$ duct. The combination of relatively high local axial Mach number at the inlet plane and large normal pressure gradients within the duct bends (due to the large offset) results in the vortex core streamtubes lifting off the bottom of the duct.

The source noise generation, as characterized by the overall sound power level at the fan leading edge, is set by the ingested streamwise circulation and is 159 dB for all the serpentine inlets studied.

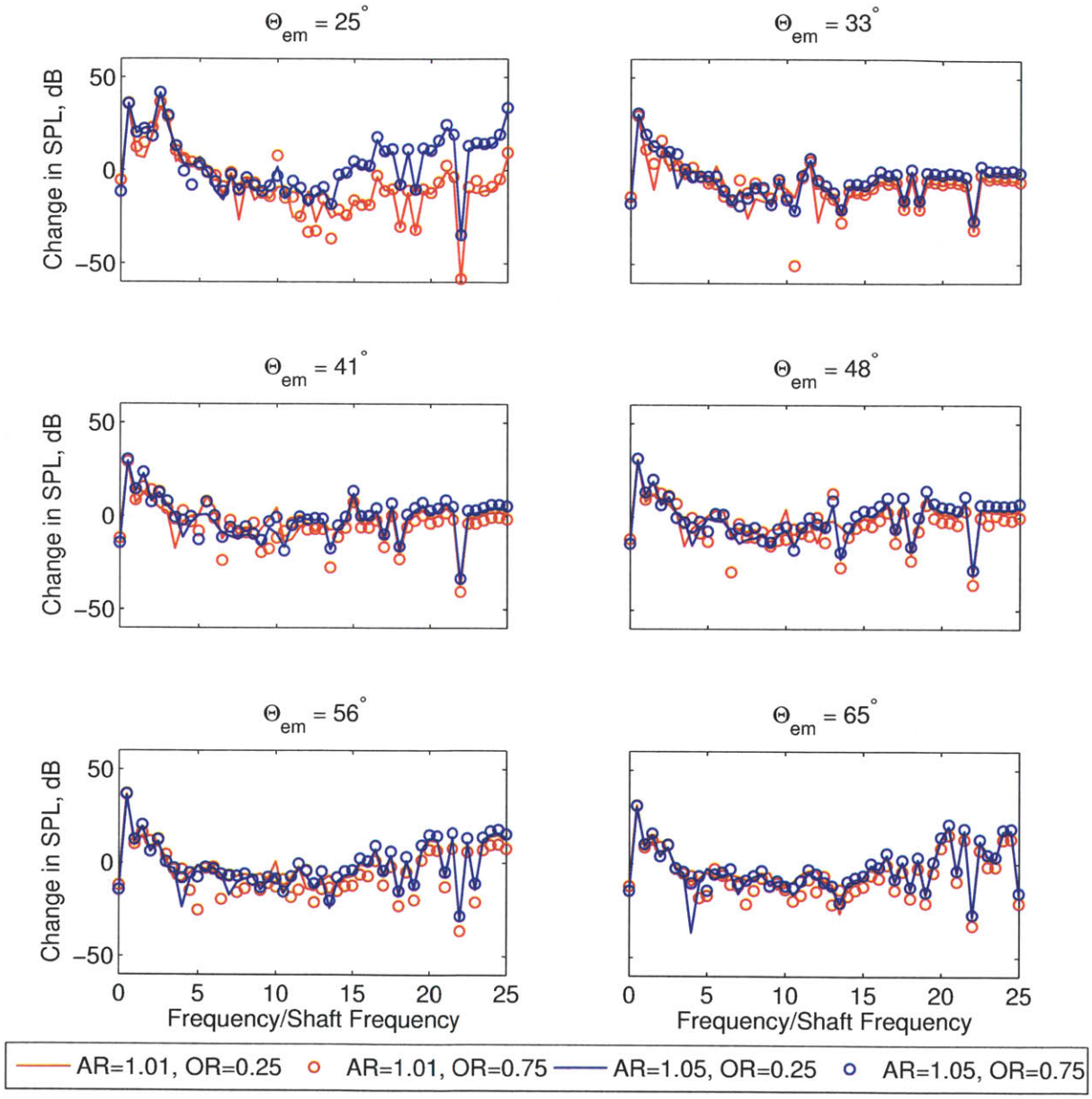

Figure 7-33: Change in far-field spectra for serpentine inlets relative to conventional inlet results after accounting for change in peak level and directivity.

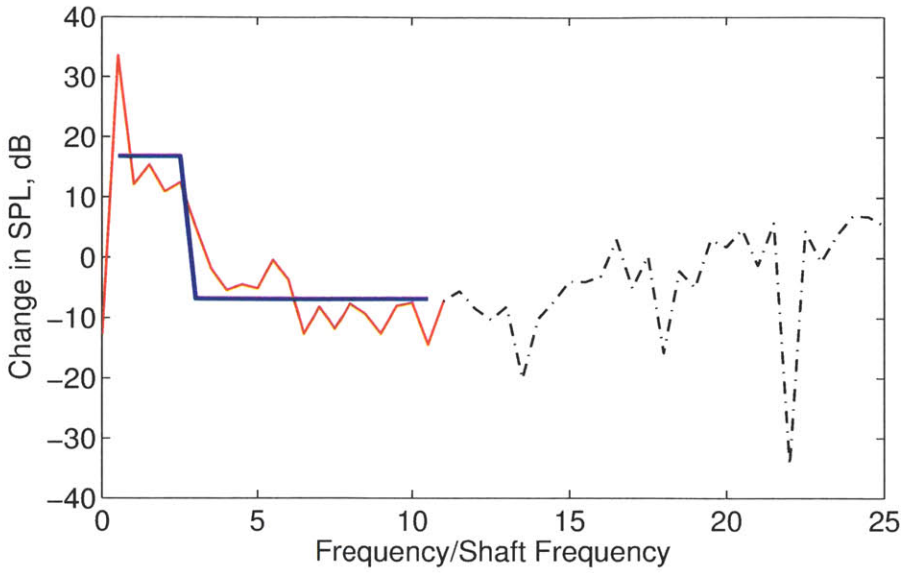

Figure 7-34: Average change in far-field spectrum for serpentine inlets relative to conventional inlet results after accounting for change in peak level and directivity; data above 11 times the shaft frequency (black) appears to be cut-off in the far-field. The blue curve gives the average amplification and attenuation of the cut-on tones.

Vortex lift-off enhances the propagation of sound power in the inlet duct by 9 dB. Since it results in a doubling of the $DC(60)$ at the fan, it might also decrease the turbomachinery performance.

It was determined that the apparent cut-off of tones above approximately $1/2$ of the blade-passing frequency in the far-field, first observed for the duct studied in Chapter 5, is not dependent on the serpentine inlet geometry for the swirl-type distortions considered but is instead set by the non-uniform external flow.

Far-field overall sound pressure levels vary with both duct area ratio and offset ratio. The overall level increases by 3.8 dB with changes in area ratio from 1.01 to 1.05 as the inlet plane area alters the external flow upstream of the inlet. The changes in overall level which result from increasing the duct offset ratio from 0.25 to 0.75 are small (less than 1 dB). The far-field directivity is not directly affected by the duct parameters but is altered in the presence of in-duct vortex lift-off. The mechanism responsible for this directivity change is not fully understood.

The next chapter synthesizes these findings to extract design guidelines for ser-

pentine inlets and to develop a response-surface correlation for the effect of swirl-type distortion and boundary layer ingestion on MPT noise.

Chapter 8

Design Guidelines & Response-Surface Correlation

In this chapter, preliminary design guidelines for serpentine inlets are presented as a response-surface correlation. The correlation is intended to augment NASA's ANOPP noise prediction code [46,47] with the capability to model the effect of swirl-type inlet distortion on MPT noise.

The output of the response-surface correlation is the far-field noise, and depends upon the inlet duct parameters. It is based on the results of a parametric study of serpentine inlet designs which revealed that it is the swirl distortion set up by the ingestion of streamwise vorticity which is the dominant mechanism which alters MPT noise generation and propagation. The model is formulated in terms of the change in far-field noise relative to a conventional axisymmetric inlet, divided into three components: the changes in peak overall sound pressure level, directivity, and spectrum. The applicability of the response-surface correlation is restricted to low-speed free-stream flows with primarily swirl-type inlet distortion. The characteristics of the serpentine inlet duct which affect the far-field noise are the area ratio (affects peak overall level) and the presence of vortex lift-off (alters directivity). To assess the quality of the estimations resulting from the response surface correlation, it is applied to a test case. The agreement for the test case is within 1 dB of the level of agreement obtained for the parametric study cases.

8.1 Preliminary Design Guidelines

The parametric study of serpentine inlets revealed that for low-speed inlet distortion, characterized by high (>99%) inlet pressure recovery and low (<0.02) $DC(60)$, the ingestion of streamwise vorticity dominates the distortion effects. The far-field noise is only weakly dependent on the duct offset ratio and area ratio. Instead, it is controlled by the swirl distortion resulting from the ingestion of streamwise vorticity. Upstream of the inlet, the vortex lines are generally in the perpendicular to the flow direction but, as flow enters the inlet and interacts with the inlet lip, the vortex lines stretch and turn, generating streamwise vorticity. The vortex line stretching is related to the axial flow acceleration through the inlet, set by the duct area ratio. This initial streamwise vorticity is more important than the additional vorticity introduced within the serpentine inlet due to flow turning because each duct bend introduces streamwise vorticity of the opposite sign resulting in cancellation.

The key findings from Chapter 7 on the effects of swirl-type distortion on source noise, propagation, and far-field noise levels are reiterated here. For the cases studied, the source noise is increased by up to 38 dB relative to the conventional axisymmetric inlet case due to swirl distortion. The source noise does not depend on the inlet duct geometry over the range explored. For the in-duct noise propagation, the primary factor which differentiates the parametric study results is the presence of vortex lift-off. When this phenomenon occurs, the in-duct attenuation of overall sound power is reduced by 9 dB between the fan and inlet plane. The increase in sound power from the AIP to the inlet plane comprises 7 dB of the 9 dB total. The mechanism responsible for this change is the local increase in the relative Mach number due to the counter-swirling vortex near mid-span, which reduces the rate of attenuation of evanescent waves in the inlet. In the far-field, the peak overall SPL is increased on average by 13.7 dB for $AR = 1.01$ and by 17.5 dB for $AR = 1.05$. A variation in this peak level of less than 1 dB occurs with changes in duct offset between $OR = 0.25$ and $OR = 0.75$. The change in directivity of the overall SPL, shown in simplified form in Figure 8-1, is affected predominantly by vortex lift-off. When this occurs, sound

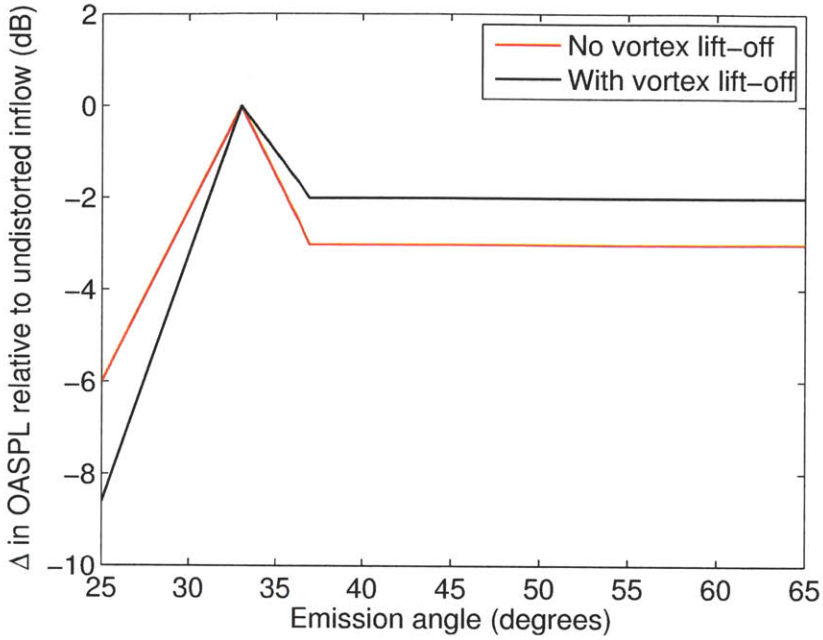

Figure 8-1: Simplified change in directivity of overall SPLs for serpentine inlets, relative to the conventional inlet case.

pressure levels at emission angles below 33° are reduced and levels at angles higher than 33° are increased. The changes in spectrum, as depicted by the blue curve in Figure 7-34, are characterized by an increase of 17 dB for tones below 0.15 times the BPF, a decrease of 7 dB for tones between 0.15 and 0.5 times BPF, and the complete cut-off of tones above 0.5 times BPF.

Based on these findings, preliminary design guidelines for low-noise embedded propulsion systems can be stated. These are:

1. Vortex lift-off should be avoided, as it increases far-field noise via the directivity. While this does not preclude using ducts with offsets as large as $OR = 0.75$, the AIP to inlet plane (throat) area ratio must be as large as 1.05 to ensure that the vortices remain near the duct wall.

2. Since increasing AR from 1.01 to 1.05 increases the far-field noise by 3.8 dB on average, using a large AR to eliminate vortex lift-off will not reduce far-field noise. Over the range of flows and duct parameters investigated, swirl distortion always increases far-field noise. Furthermore, the increase in far-field

noise due to swirl distortion (at least 13 dB) is dominant compared to the 4.7 dB maximum variation observed as a result of changes in inlet geometry.

3. Use inlet lip geometries to mitigate streamwise vorticity development, such as leading edge strake extensions.

The ingested streamwise vorticity is the dominant mechanism leading to increased MPT noise; the far-field noise is weakly dependent on the duct area and offset ratios. This insight, combined with items (1) and (2) above, suggests that to minimize MPT noise propagation in the presence of swirl distortion, both the area ratio and offset ratio of the duct should be minimized. In many applications, however, this may not be possible, for example when the detectability of the propulsion system is an important parameter. It might also be possible to take advantage of the shift in acoustic energy towards low frequencies to enhance the effectiveness of acoustic liners in the inlet.

8.2 A Response-Surface Correlation of the Effects of Swirl Distortion on MPT Noise

In this section, a simple correlation for the effects of boundary layer ingestion and inlet distortion on MPT noise is developed based on the results of the parametric study of serpentine inlets. The purpose of the correlation is to provide the capability for including effects of inlet distortion on MPT noise in ANOPP.

The applicability of the model is as follows:

- Free-stream Mach number: $M_\infty = 0.1$
- AIP Mach number: $M_{AIP} \approx 0.5$
- Frequency: up to BPF
- Emission angle: $25° \leq \Theta_{em} \leq 65°$
- Area ratio: $1.01 \leq AR \leq 1.05$

- Duct offset: $0.25 \leq OR \leq 0.75$
- Duct length: $\frac{L}{D_{AIP}} = 2$

The response-surface correlation is limited to this parameter space. Outside this range, it may not capture the relevant physics.

The required inputs are the duct area ratio and knowledge of whether or not vortex lift-off occurs for the inlet under consideration. The outputs are (relative to the same fan installed in a conventional inlet):

1. The change in peak overall far-field SPL (which occurs at 33° emission angle)
2. The change in far-field directivity for the overall SPL
3. The changes in far-field spectrum

Note that the presence of the airframe acts as a reflecting surface and therefore increases far-field noise by 3 dB due to reflections from the upper airframe surface. The change in noise below the aircraft was not assessed in this work but a noise shielding approach by Colas [50] based on diffraction integral theory indicates that the SAX-40 airframe attenuates turbomachinery noise by up to 30 dB.

8.2.1 Detailed Description of the Response-Surface Correlation

The response-surface correlation consists of three parts, simplified from the results obtained in Chapter 7. These are items (1)-(3) from earlier in this section.

The peak OASPL occurs at $\Theta_{em} = 33°$ and its change from the conventional inlet level is only a function of the duct area ratio:

$$\Delta OASPL_{peak} = \begin{cases} 13.7\,\text{dB}, & AR = 1.01 \\ 17.5\,\text{dB}, & AR = 1.05 \end{cases} \tag{8.1}$$

To separate the contribution from the area ratio and from the swirl distortion, linear dependence on the area ratio is assumed. Without additional data points at other

area ratios, this is a best guess as to the nature of the dependence. The result is:

$$\Delta OASPL_{peak} = 95\,(AR - 1) + 12.75\,\text{dB} \tag{8.2}$$

The change in directivity is given in Figure 8-1. In equation form,

$$\Delta Dir_{no\ vortex\ lift-off} = \begin{cases} -24.75 + 0.75\Theta_{em}\,\text{dB}, & \Theta_{em} < 33^\circ \\ 24.75 - 0.75\Theta_{em}\,\text{dB}, & 33^\circ \leq \Theta_{em} \leq 37^\circ \\ -3\,\text{dB}, & \Theta_{em} > 37^\circ \end{cases} \tag{8.3}$$

$$\Delta Dir_{w/\ vortex\ lift-off} = \begin{cases} -35.475 + 1.075\Theta_{em}\,\text{dB}, & \Theta_{em} < 33^\circ \\ 16.5 - 0.5\Theta_{em}\,\text{dB}, & 33^\circ \leq \Theta_{em} \leq 37^\circ \\ -2\,\text{dB}, & \Theta_{em} > 37^\circ \end{cases} \tag{8.4}$$

The change in spectrum is adapted from the blue line in Figure 7-34. In Figure 8-2, the same change in spectrum is given but the frequency axis is normalized by the blade-passing frequency. The result is:

$$\Delta Spectrum = \begin{cases} +17\,\text{dB}, & \frac{f}{BPF} < 0.15 \\ -7\,\text{dB}, & 0.15 \leq \frac{f}{BPF} \leq 0.5 \\ -\infty\,\text{dB}, & \frac{f}{BPF} > 0.5 \end{cases} \tag{8.5}$$

The total change in the far-field noise relative to the levels for a conventional inlet is the sum of these three effects:

$$\Delta Far\text{-}field\ SPL = \Delta OASPL_{peak} + \Delta Dir + \Delta Spectrum \tag{8.6}$$

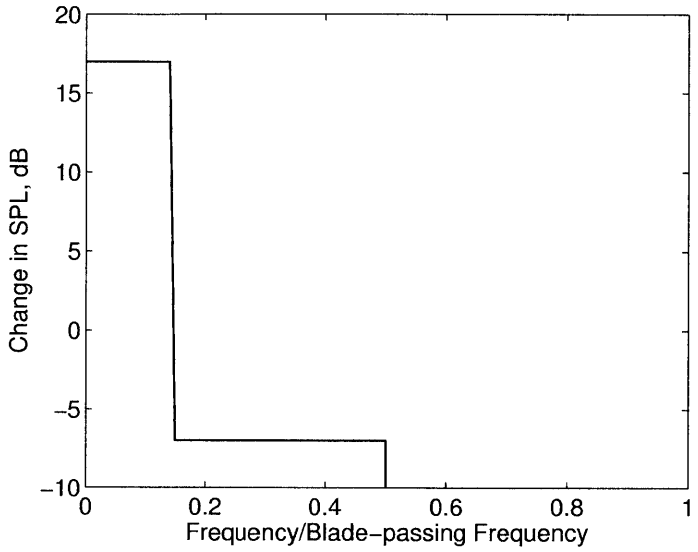

Figure 8-2: Simplified change in far-field spectrum as a result of swirl distortion.

8.2.2 Assessment of Approximations in the Response-Surface Correlation

The utility of the response-surface correlation is first assessed by quantifying the differences between the computed far-field noise and the levels predicted using the model for the four ducts comprising the parametric study. The correlation uses the computed spectra from the conventional inlet as the baseline from which the changes in level are determined. In Figure 8-3, the far-field spectra for each of the four inlets are shown along with the predicted spectra at $\Theta_{em} = 33°$, which is the emission angle at which the increase in overall level is maximum. The estimate only encompasses frequencies up to one-half of the BPF, since at higher frequencies the computed results are considered to be cut-off. The exact spectra differ somewhat, with some frequencies over-predicted by up to 20 dB and others under-predicted by up to 10 dB. However, the overall trends are captured, namely the enhanced noise levels below 0.15 BPF and the decreased levels between 0.15 BPF and cut-off at 0.5 BPF.

To investigate the ability of the response-surface correlation to estimate the directivity of the computed results, the OASPL is plotted against emission angle for all four ducts in Figure 8-4. At emission angles above 30°, the error in the predicted

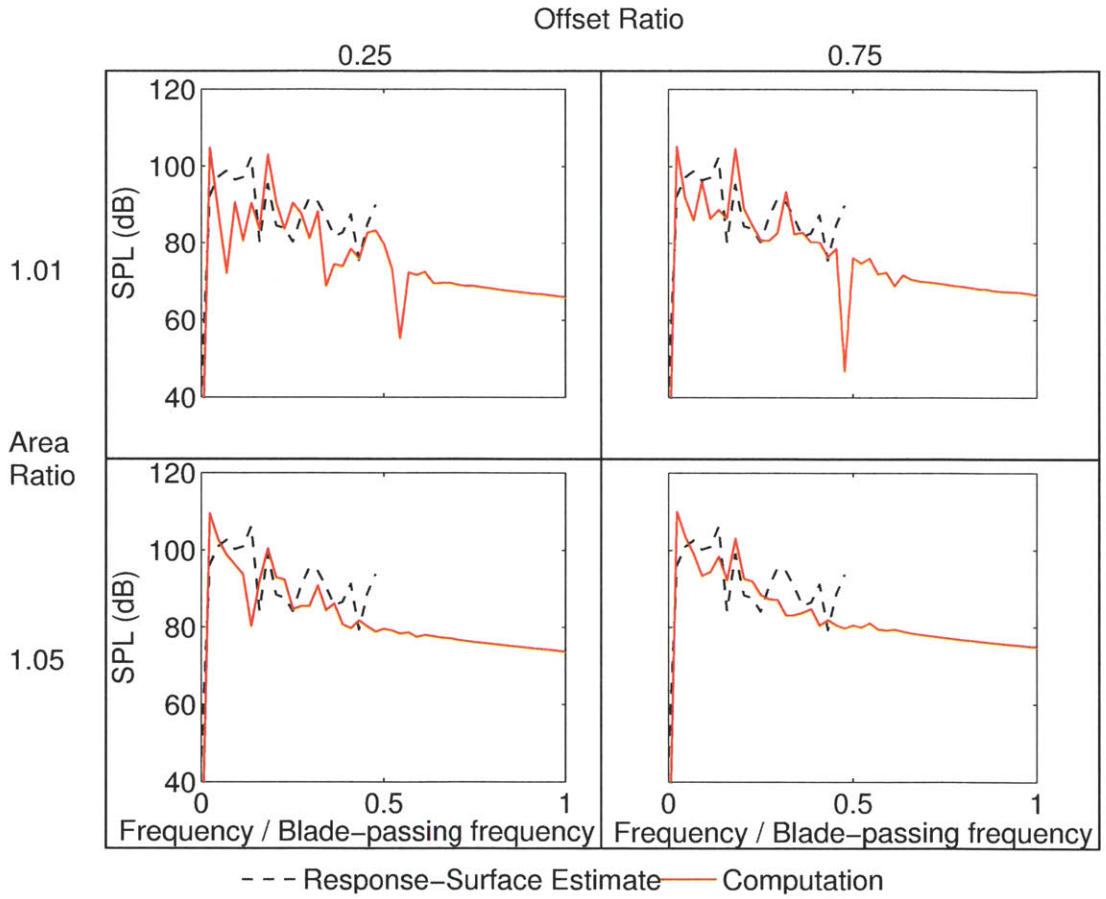

Figure 8-3: Far-field spectra at $\Theta_{em} = 33°$ computed from CFD and based on the response-surface correlation.

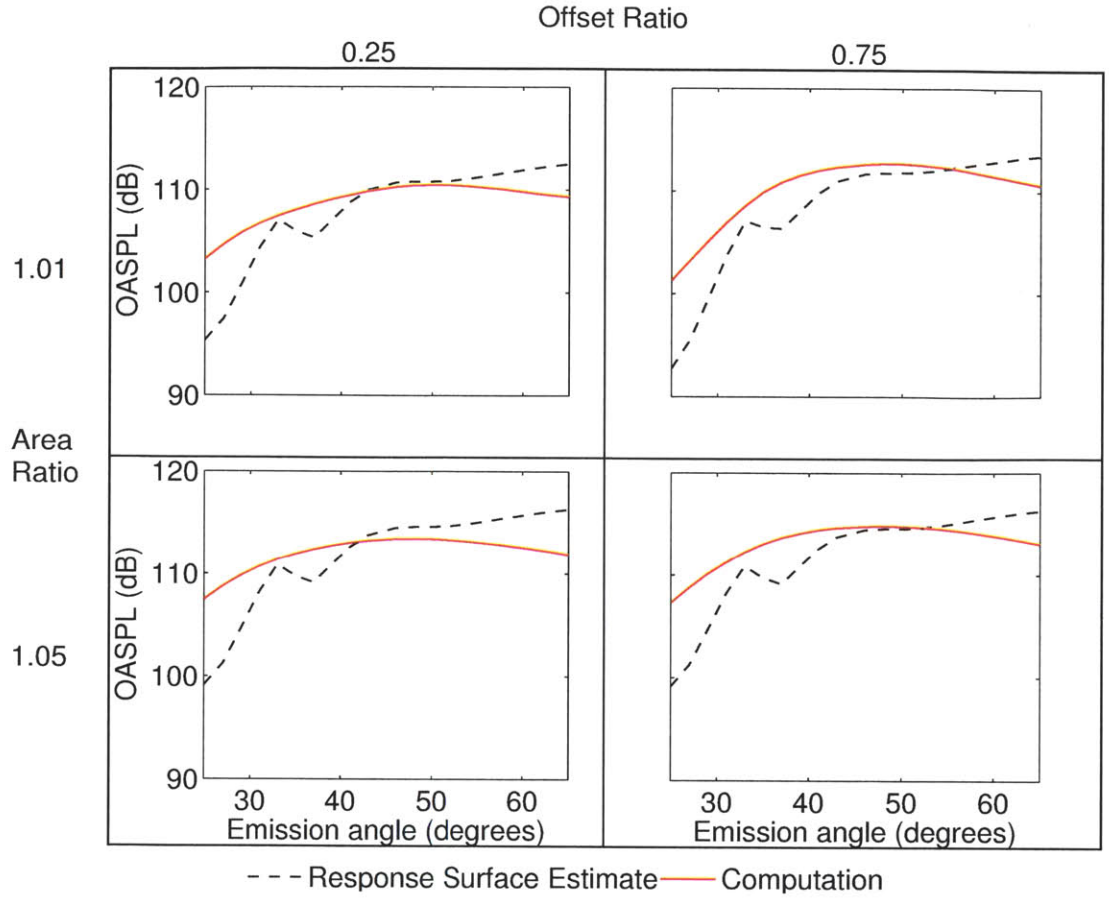

Figure 8-4: Directivity of overall sound pressure levels computed from CFD and based on the response-surface correlation.

OASPL is everywhere less than 5 dB, indicating fair agreement. At emission angles less than 30°, the error increases and can become as large as 8.5 dB.

To assess the quality of the fit obtained from the response-surface correlation, the results are compared to the predictions produced by ANOPP for MPT noise. The spectrum at 33 degrees emission angle is given in Figure 8-5. The changes in spectrum due to swirl distortion, namely the amplification of tones at frequencies below 0.15 BPF and the attenuation of tones at frequencies above 0.5 BPF, are not captured since the ANOPP noise prediction framework does not include inlet distortion effects on MPT noise. The directivity is less affected by the swirl distortion and so the prediction from ANOPP is qualitatively in agreement with the computational results. Quantitatively, however, the agreement is poor as the overall sound pressure levels

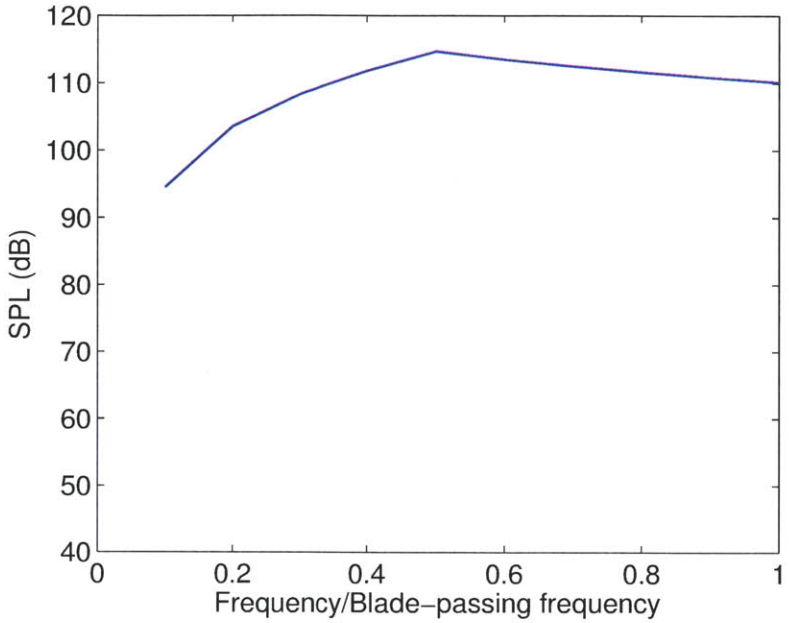

Figure 8-5: Spectrum for MPT noise from the R4 fan rotor at $\Theta_{em} = 33°$ produced by ANOPP.

are over-predicted by between 10 and 20 dB.

The response-surface correlation therefore provides an improved estimate of the far-field spectra by capturing the effects of swirl distortion and also quantitatively captures the directivity in the presence of swirl distortion.

To provide an overall quantitative assessment of the errors associated with the simplifying assumptions in the response-surface correlation, the RMS error in the spectrum (up to one-half of the blade-passing frequency), depicted in Figure 8-7, is analyzed for each of the four inlets from the parametric study; it is everywhere less than 12 dB. While 12 dB is a relatively large error, the distribution of the RMS error does not have a consistent bias. The average RMS errors for each duct over the emission angle range $25° \leq \Theta_{em} \leq 65°$ are given in Table 8.1. The minimum error is 7.3 dB for the $AR = 1.05$, $OR = 0.75$ duct while the maximum error is 8.7 dB for the $AR = 1.01$, $OR = 0.75$ duct. This difference of only 1.4 dB indicates that the response-surface correlation provides a consistent level of accuracy in the estimation of the far-field noise. The main source of the RMS error is disagreement

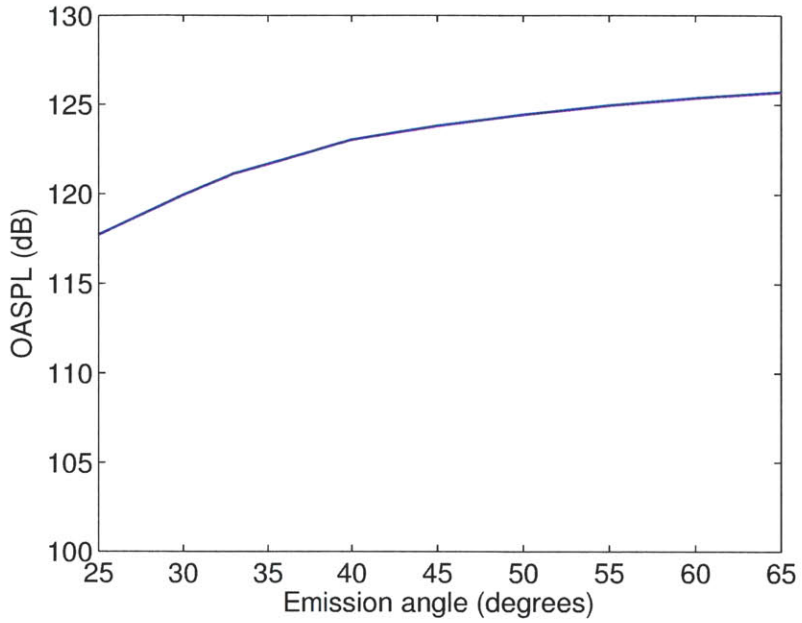

Figure 8-6: Directivity of overall sound pressure levels for the R4 fan rotor as produced by ANOPP.

Table 8.1: Average RMS error in far-field spectrum using response-surface correlation.

AR \ OR	0.25	0.75
1.01	8.6 dB	8.7 dB
1.05	8.1 dB	7.3 dB

of the frequencies at which MPTs occur. Yet a large RMS error does not necessarily result in an equally large error in OASPL, an integrated quantity.

The RMS error could be reduced by using a more accurate representation of the the change in spectrum than the simple curve shown in Figure 8-2. Capturing the shift in the frequencies at which MPTs appear as a result of swirl distortion, as opposed to only the capturing the change in level over a frequency range, may lead to reduced errors in the spectra. However, a larger set of simulation results than what is available here should be used to do this effectively,

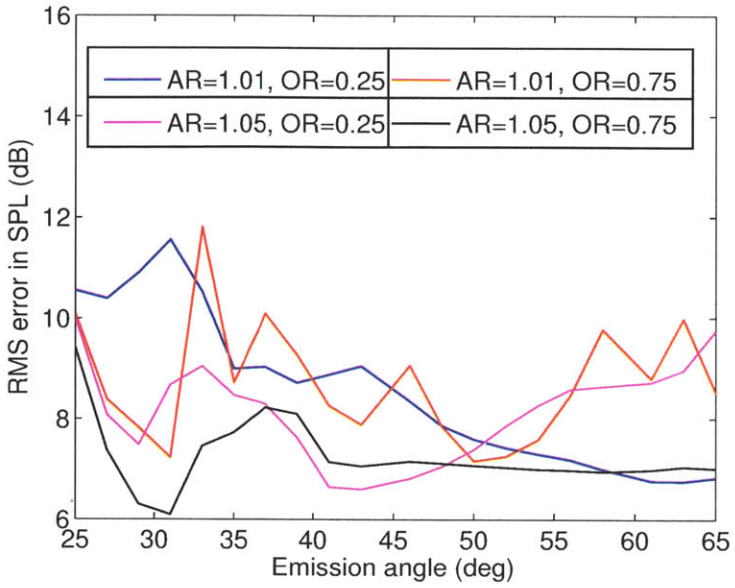

Figure 8-7: RMS error in noise levels determined using the response-surface correlation (for cut-on frequencies) vs. emission angle.

8.3 A Test Case

To assess the ability of the response-surface correlation to estimate MPT noise within its range of applicability, the correlation is applied to the SAX-40 inlet studied in Chapter 5 as a test case. This inlet has $OR = 0.52$ and $AR = 1.03$, putting it near the center of the parameter space spanned by the four inlets studied in Chapter 7. Vortex lift-off does not occur with this inlet.

In Figure 8-8, the computed and predicted spectra at $\Theta_{em} = 33°$ are depicted for the SAX-40 inlet. Good overall agreement is obtained, though at this emission angle the cut-off frequency for the computed far-field tones is nearer to 0.6 BPF than to the 0.5 BPF assumed in the response-surface correlation. The SPLs are over-predicted between 0.05 and 0.15 BPF by approximately 15 dB. To assess the accuracy with which the directivity is captured by the response-surface correlation for this test case, the OASPL as a function of emission angle is examined, shown in Figure 8-9. The agreement is within 5 dB for emission angles as low as 27°, which is a broader range than for the ducts assessed in the previous section. The maximum under-prediction, at $\Theta_{em} = 25°$, is 6.3 dB, compared to 8.5 dB for the parametric study inlets. To

assess the accuracy of the predicted spectra across all emission angles, the RMS error up to 0.5 BPF is determined, as depicted in Figure 8-10. The result is qualitatively similar to the parametric study cases, though the minimum RMS error is larger by approximately 2 dB. The maximum RMS error remains approximately 12 dB. The average RMS error over the emission angles considered is 9.2 dB, 1.0 dB more than the average of the parametric study cases.

An important difference between the ducts comprising the parametric study and the SAX-40 inlet duct is the cross-sectional geometry. While the parametric study included only circular ducts, the SAX-40 inlet has a cross-section which is semi-elliptical at the upstream end of the inlet but is circular at the AIP. This change in cross-section may contribute to differences in the far-field noise, since cross-sectional area effects are not included in the response-surface correlation. This test case indicates that a decrease in accuracy of the far-field noise estimate by approximately 1.0 dB may be caused by these changes in duct cross-section.

The evaluation of the test case reveals that a limitation of the response-surface correlation is its inability to account for changes in the duct cross-section. The response-surface correlation should thus primarily be used for ducts whose cross-sections are circular or close to circular.

8.4 Summary of Design Guidelines and Response-Surface Correlation

In this chapter, design guidelines for low-noise BLI propulsion systems were presented. The most important mechanism which alters MPT noise in a boundary-layer-ingesting inlet is swirl distortion resulting from the ingestion of streamwise vorticity. This swirl distortion increases far-field SPLs by at least 13 dB for the cases considered while the variations in serpentine inlet geometry studied further increase far-field noise by at most 5 dB.

Based on the parametric study of serpentine inlets, a response-surface correlation

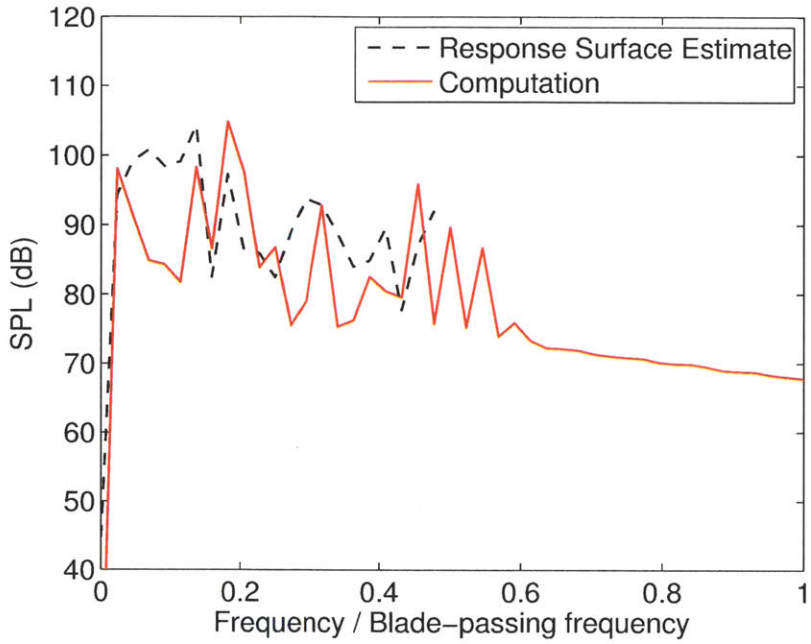

Figure 8-8: Far-field spectra for the SAX-40 inlet test case at $\Theta_{em} = 33°$ computed from CFD and based on the response-surface correlation.

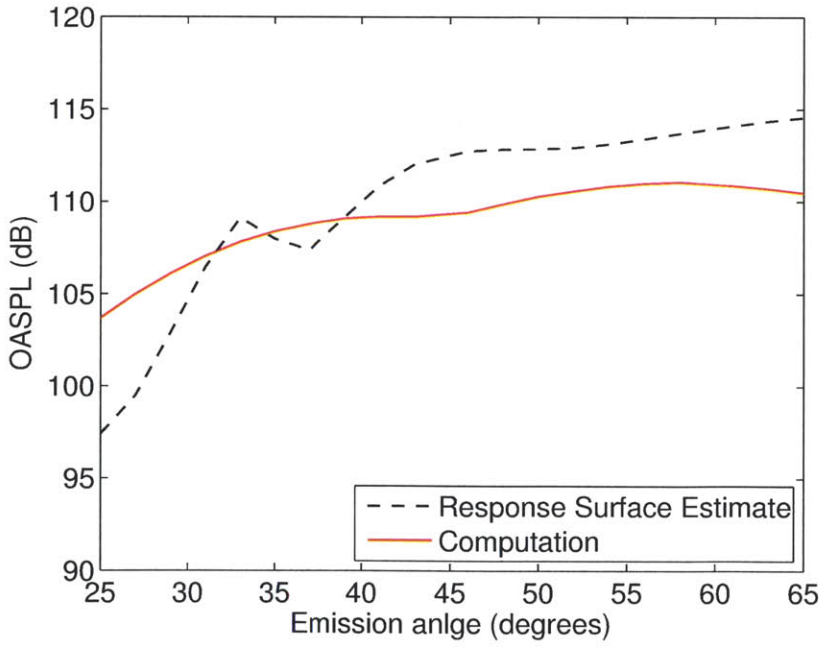

Figure 8-9: Directivity of overall sound pressure levels for SAX-40 inlet test case computed from CFD and based on the response-surface correlation model.

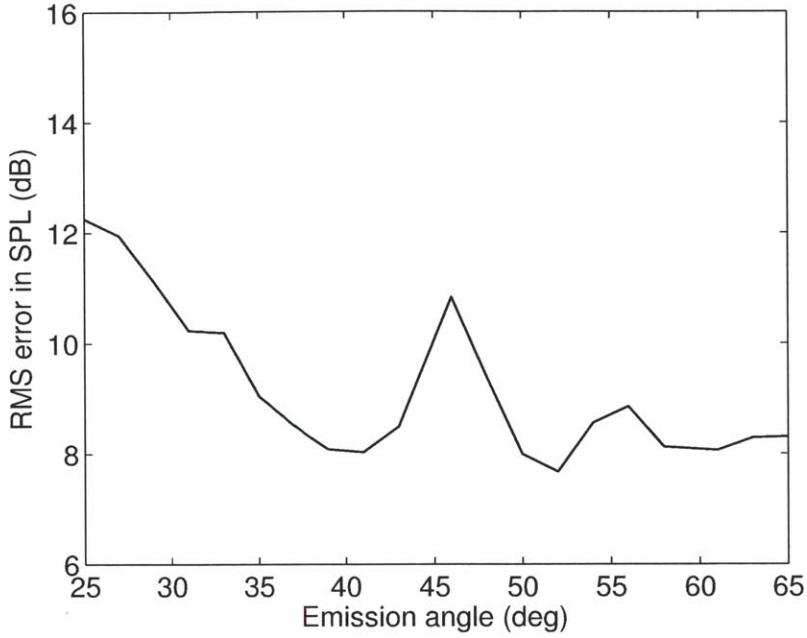

Figure 8-10: RMS error in noise levels determined using response-surface correlation (for cut-on frequencies) vs. emission angle for the SAX-40 inlet test case.

for the effects swirl distortion and serpentine inlet geometry on far-field noise was developed. The input is the far-field noise obtained for a conventional inlet and is therefore suggested for use along with the current MPT noise module in NASA's ANOPP aircraft noise prediction code to enable the noise assessment of aircraft with boundary-layer-ingesting propulsion systems. The response-surface correlation output depends on the area ratio of the inlet and on whether or not vortex lift-off occurs in the inlet duct. The accuracy of the estimates obtained for the far-field noise is acceptable within the parameter space in which it is intended to be used. The OASPLs are predicted to be within 5 dB of the computed values, and the mean RMS error in the spectra is approximately 8 dB. However, the test case also revealed that a limitation of the response-surface correlation is a lack of dependence on duct cross-section, which may contribute to the decreased accuracy of the far-field noise estimate for that case, which employed a semi-elliptical-to-circular serpentine inlet duct.

Chapter 9

Summary and Conclusions, and Future Work

The goal of this thesis was to quantify the effects of inlet distortion and boundary layer ingestion on upstream-propagating rotor shock noise (MPT noise). The enabling idea was the development of a body-force-based fan model as the noise source in a single, simultaneous aeroacoustic computation of the flow, noise source generation, and acoustic propagation through the internal and external flows. This model was assessed on a conventional inlet and was determined to provide an acceptable level of accuracy. It was then used to assess the impact of swirl-type distortion and serpentine duct geometry on MPT noise. The applicability and limitations of the body force approach are discussed. Conclusions deduced from the results are presented, as are recommendations for future work identified based on the findings of the thesis.

9.1 Summary

Computational modeling of MPT noise in non-uniform flow has been enabled by using a body force field to represent the fan and rotating force perturbations to generate the system of expansion fans and shocks which is the source of MPT noise. The approach was assessed using experimental data for the NASA/GE R4 conventional axisymmetric inlet, for which good agreement was obtained for the far-field noise

spectra between 25° and 65° emission angle.

The effects of boundary layer ingestion with swirl-type distortion were quantified for source noise generation, in-duct propagation, and far-field noise for several serpentine inlet duct designs.

The impact of assuming uniform flow for the purpose of determining propagating sound power within the inlet was assessed and determined to be as large as 11 dB for the SAX-40 inlet. This motivated the use of an alternative approach to the computation of sound power which does not make assumptions about the flow, instead determining the sound power by integrating the local sound intensity field.

Based on a parametric study of serpentine inlets and the insights gained from interrogation of the results, a response-surface correlation was developed to estimate the effects of serpentine inlets with BLI (for low-speed flow/swirl distortion) on the changes in far-field noise for a given fan relative to its installation in a conventional axisymmetric inlet.

In Chapter 3, a complete aeroacoustic approach for predicting fan noise in non-uniform flow was presented. The key new idea that enables the approach is the generation of the system of expansion fans and shocks associated with a transonic fan using a rotating perturbation to the body force field which provides the flow turning and pressure rise associated with the fan blade row. The model has the capability to include the effects of blade-to-blade variations in stagger angle due to manufacturing/installation imperfections. Techniques to enhance the accuracy of the computational aeroacoustic results were also presented.

The ability of the approach to model source and far-field noise was assessed Chapter 4 for a conventional inlet. It was shown that the shock system/source noise generation and far-field spectra are in good agreement with experimental data for emission angles from 25° to 65°. The approach can propagate MPT noise from the fan to the far-field with sufficient accuracy that the impact of serpentine inlets and BLI on far-field noise for the NASA/GE R4 fan can be assessed on a relative basis.

A back-to-back comparison of the conventional inlet results to those from a serpentine inlet was the focus of Chapter 5. The key differences are that the source

sound power is increased by up to 38 dB due to inlet distortion and that the far-field spectra are altered in the following ways: tones below 1/4 BPF are amplified while tones above 1/2 BPF appear to be cut-off (i.e. they are below the numerical noise floor) for the serpentine inlet case. The average overall sound pressure level in the far-field is only increased by 7 dB for the serpentine case. The additional in-duct attenuation this implies is due to regions of subsonic relative flow in the inlet due to co-swirling vorticity, which results in locally evanescent wave behavior. A simple model of the effect of non-uniform flow on noise generation does not capture the increase in source power, indicating that it is the propagation through non-uniform flow that results in the change in power rather than change in the pressure field at the fan leading edge.

The error inherent in computing sound power in non-uniform flow assuming that that the uniform-flow solution to the Helmholtz equation holds is assessed in Chapter 6. Compared to an alternative approach for determining sound power which does not assume uniform flow but instead involves integrating the local sound intensity, the uniform-flow assumption can result in an over-prediction of the sound power by up to 11 dB in the SAX-40 inlet. A technique to extract spectral information for sound power computed using local intensity is also presented.

With the capability to accurately assess sound power in non-uniform flows, a parametric study of serpentine inlet designs was undertaken in Chapter 7. The duct downstream-to-upstream area ratio was varied between 1.01 and 1.05 and the duct offset to downstream diameter ratio was varied between 0.25 and 0.75. The parametric study led to the following insights into the behavior of the flow and acoustics, and the relationships between them: (1) if the streamwise vortex cores are sufficiently accelerated through the upstream end of the serpentine duct and the duct normal pressure gradients are large enough, the vortex cores will not follow the contours of the duct but will instead "lift-off" and impact the fan near mid-span instead of at the outer span (this occurred for the $AR = 1.01$, $OR = 0.75$ duct); (2) the source noise is increased by 38 dB due to swirl distortion for the cases studied; (3) the peak overall far-field sound pressure level depends on the duct area ratio as this alters

the external flow through which the acoustic waves must propagate from the inlet; (4) vortex lift-off alters the far-field directivity; (5) the far-field spectra are weakly dependent on the duct parameters, and are similar to the results obtained for the SAX-40 inlet studied in Chapter 5 in that low-frequency tones are amplified while tones above 0.5 BPF appear to be cut-off. These findings suggest that the ingestion of streamwise vorticity may control the far-field apparent cut-off frequency and/or source noise since the duct parameters do not affect these aspects of the fan noise at the level of BLI used, which has a pressure recovery >99% and thus is predominantly a swirl-type distortion.

The findings from the parametric study were synthesized in Chapter 8. The takeaway is that swirl distortion is the main driver of changes in MPT noise with the duct offset and area ratios contributing secondary effects. This chapter also distilled the effects on far-field noise into a response-surface correlation that is compatible with NASA's ANOPP noise prediction tool and can enable the estimation of MPT noise to be made for aircraft with BLI. The accuracy of the estimates produced by the response-surface correlation is assessed by using it for a test case (the SAX-40 inlet studied in Chapter 5). Overall levels are generally in agreement within 5 dB.

9.2 Applicability and Limitations of the Body Force Approach

The body-force-based fan description used here is specific to the NASA/GE R4 fan rotor, but the modeling framework is applicable to other fan geometries.

The inputs to the body force model are the camber angle and solidity distributions. Single-passage RANS calculations at the operating point(s) of interest are used to determine the force coefficients K_n and K_p. A limitation of the force definition in its original formulation [14] is that only K_n varies within the blade row. This does not capture substantial increases in blade loss which occur in separated flow. Another limitation is that the blade passage approximation neglects forces in the radial di-

rection. For advanced fan designs with highly three-dimensional blade shapes, radial flow redistribution can be important and the model needs to be extended. Recent work [51] has addressed both of these limitations and the improved body force model could be used in the future within the fan modeling framework presented here.

The technique for obtaining perturbation force fields which model rotor shock noise is general and may be applied to any fan for which a time-mean body force model has been obtained. The specific forms and amplitudes of the perturbations would need to be determined using single-passage, 3D RANS flow field information and 2D cascade computations, similarly to what was done for the NASA/GE R4 fan rotor.

9.3 Key Outcomes and Conclusions

The following conclusions have been deduced from the results of this thesis. They can be divided into two categories: those which are generic and those which apply specifically to the fan, geometries and conditions tested in this thesis.

The generic conclusions are:

1. A body-force-based model of a fan using a rotating disturbance field can accurately generate the expansion fan/shock system associated with a transonic rotor. This modeling capability enables the aeroacoustic assessment of boundary-layer ingesting and/or embedded propulsion systems by generating the detached passage shocks in an Euler calculation which reduces numerical wave dissipation.

2. A technique for obtaining sound power spectra based on integrating the local sound intensity was presented, enabling accurate assessment of the frequency content of the propagating acoustic energy through an arbitrary surface and arbitrary background flow.

3. The dominant mechanism for change in far-field MPT noise due to boundary layer ingestion at low flight speeds is the swirl distortion resulting from the

ingestion of streamwise vorticity.

The specific conclusions are:

1. Boundary layer ingestion at low speed ($M_\infty = 0.1$) increases source sound power up to 38 dB for the NASA/GE R4 fan due to swirl distortion but only increases far-field overall sound pressure levels by at most 18 dB. The additional sound power attenuation in the inlet duct is due to locally evanescent wave behavior where co-swirling flow lowers the relative Mach number below the sonic point.

2. Assuming uniform flow in order to compute the sound power in a duct with non-uniform flow can lead to over-prediction of the power by up to 11 dB (for the SAX-40 inlet) compared to integrating the local sound intensity.

3. Lift-off of the streamwise vortices from the duct bottom occurs for the high offset ($OR = 0.75$), low area ratio ($AR = 1.01$) inlet duct. This results in streamwise vortices impacting the fan at mid-span, and also keeps the vortices more compact, increasing the distortion coefficient (DC60) by a factor of two.

4. The in-duct acoustic effect of the vortex lift-off is to increase the propagated sound power from the inlet by 9 dB, due to reduced decay rates in the cut-off region near mid-span caused by the increase in relative Mach number due to the counter-swirling vortex.

5. The far-field directivity is altered (levels are decreased at low emission angles and increased at high emission angles) due to in-duct vortex lift-off. The mechanism responsible for this change is not clear.

6. The far-field peak overall sound pressure level increases with duct area ratio. This is suggested to be due to the changes in the external flow which occur when the duct inlet plane is reduced in size but is required to pass the same corrected mass flow.

7. A response-surface correlation for the effects of duct geometry and swirl distortion on far-field noise enables the assessment of MPT noise in integrated

propulsion systems for codes like NASA's ANOPP noise prediction framework.

9.4 Recommendations for Future Work

While this work has focused on upstream-propagated tonal fan noise, this is only one of many engine noise sources. The following work would broaden the applicability of the present approach to other types of fan noise.

1. The current approach is limited in its ability to model rotor-stator interaction since the full Euler equations are used within the blade row. Using Gong's modified set of equations instead, which would require working with a solver for which the source code is accessible to the user, would enable the extension of the current approach to the study of both upstream- and downstream-propagated rotor-stator interaction noise. There are two challenges which must be overcome to enable this additional capability: (a) obtaining accurate blade wakes using the body force approach; and (b) modeling the blockage effect of the blade row on noise propagation. Addressing these challenges would significantly expand the utility of the body-force-based approach.

2. The other important aspect of fan acoustics is broadband noise, which occurs due to the presence of unsteady turbulent structures in the flow. To enable the prediction of this type of noise, viscous simulations must be used as opposed to the Euler solver employed in this thesis. This would increase the computation cost, however, and this challenge would need to be overcome to render broadband noise prediction practical for the propagation distances needed for this type of problem. Using viscous computations would also enable the prediction of flow separation in the inlet duct.

An important conclusion from this work was that the far-field and source noise are predominantly set by the ingested streamwise vorticity and the resultant swirl distortion. To more fully explore the scaling of MPT noise in the presence of swirl distortion, the following additional studies could be undertaken with the current approach.

1. The duct length to diameter ratio could be parametrically varied to determine the scaling of the in-duct attenuation due to swirl distortion with propagation distance.

2. The duct offset ratio could be varied down to zero (i.e no serpentine inlet) to establish the baseline change in MPT noise due to swirl distortion.

3. The amount of boundary layer ingestion could be altered through (a) varying the free-stream flow speed and/or (b) altering the length of airframe upstream of the inlet. This would change the ingested vorticity and potentially reveal the scaling for increase in source sound power.

4. The non-uniformities in the external flow could be varied by moving the stagnation point on the nacelle. This may reveal the scaling for the apparent far-field cut-off frequency.

5. Further parametric studies within the parameter space whose bounding box is formed by the four cases studied in this thesis should be undertaken to determine under precisely what conditions vortex lift-off occurs, and how this phenomenon's effect on the far-field directivity scales in hopes of finding the mechanism responsible for the directivity changes.

Finally, it was observed that for a given amount of BLI, the source noise is not altered, and that the acoustics within the serpentine portion of the inlet can be modeled as being linear due to the reduced wave amplitudes compared to the near-field of the fan. Therefore a split computational approach could be employed which might enable the use of adjoint methods to optimize the inlet duct for low noise subject to aerodynamic constraints. This would involve using a steady computation to resolve the flow field, an unsteady computational aeroacoustic simulation from the fan to the AIP, and a linear propagation code to propagate the noise upstream of the AIP. The adjoint solver would only need to run on the linear propagation domain, rendering the problem tractable.

Bibliography

[1] Smith, A. and Reberts, H. The jet airplane utilizing boundary layer air for propulsion. *Journal of the Aeronautical Sciences*, 14(2):97–109, 1947.

[2] Lynch, F. A theoretical investigation of the effect of ingesting airframe boundary layer air on turbofan engine fuel consumption. Technical Report SM-23981, Douglas Aircraft Company, May 1960.

[3] Betz, A. *Introduction to the Theory of Flow Machines.* Pergamon Press, 1966.

[4] Douglass, W. Propulsive efficiency with boundary layer ingestion. Technical Report MDC J0860, McDonnell Douglas, August 1970.

[5] Smith, L. Jr. Wake ingestion propulsion benefit. *Journal of Propulsion and Power*, 9(1):74–82, 1993.

[6] Sargeant, M. *Boundary Layer Ingestion for Advanced Airframes.* Ph.D. thesis, University of Cambridge, Department of Engineering, 2007.

[7] Drela, M. Power Balance in Aerodynamic Flows. *AIAA Journal*, 47(7):1761–1771, July 2009.

[8] Coupland, J., Wilson, A., Pollard, N., Uellenberg, S., Breard, C., and Diamond, J. Demonstration of a CFD-CAA Methodology to Predict Buzz-Saw Noise Propagation to the Aircraft. In *presented at the 13th AIAA/CEAS Aeroacoustics Conference*, Rome, Italy, May 21-23 2007. AIAA paper 2007-3517.

[9] Hawkings, D. Multiple Tone Generation By Transonic Compressors. *Journal of Sound and Vibration*, 17(2):241–250, 1971.

[10] Gliebe, P., Mani, R., Shin, H., Mitchell, B., Ashford, G., Salamah, S., and Connell, S. Aeroacoustic Prediction Codes. Technical Report CR-2000-210244, NASA, 2000.

[11] Alonso, J., Burdisso, R., and Anderson, J. Nonlinear modeling of shock wave trains in ducts with wall discontinuities. In *presented at the 12th AIAA/CEAS Aeroacoustics Conference*, Cambridge, Massachusetts, May 8-10 2006. AIAA paper 2006-2460.

[12] Fernando, R., Marchiano, R., Coulouvrat, F., and Druon, Y. Buzz-saw noise: propagation of shock waves in aero-engine inlet ducts. In Enflo, B., Hedberg, C., and Kari, L., editor, *Nonlinear Acoustics–Fundamentals and Applications (ISNA 18), 18th International Symposium*, pages 99–102, 2008.

[13] Marble, F. *Three-dimensional flow in turbomachines*, volume X of *High Speed Aerodynamics and Jet Propulsion, Hawthrone, W. R., ed.* Princeton University Press, Princeton, NJ, pp. 83-166 edition, 1964.

[14] Gong, Y. *A Computational Model for Rotating Stall and Inlet Distortions in Multistage Compressors.* Ph.D. thesis, MIT, Department of Aeronautics and Astronautics, March 1999.

[15] Hughes, C., Jeracki, R., Woodward, R., and Miller, C. Fan Noise Source Diagnostic Test - Rotor Alone Aerodynamic Performance Results. In *presented at the 8th AIAA/CEAS Aeroacoustics Conference and Exhibit*, Breckenridge, Colorado, June 17-19 2002. AIAA paper 2002-2426.

[16] Podboy, G., Krupar, M., Helland, S., and Hughes, C. Steady and Unsteady Flow Field Measurements Within a NASA 22 Inch Fan Model. In *presented at the 40th AIAA Aerospace Sciences Meeting and Exhibit*, Reno, Nevada, January 14-17 2002. AIAA paper 2002-1033.

[17] Woodward, R., Hughes, C., Jeracki, R., and Miller, C. Fan Noise Source Diagnostic Test - Far-field Acoustic Results. In *presented at the 8th AIAA/CEAS*

Aeroacoustics Conference and Exhibit, Breckenridge, Colorado, June 17-19 2002. AIAA paper 2002-2427.

[18] Heidelberg, L. Fan Noise Source Diagnostic Test - Tone Modal Structure Results. In *presented at the 8th AIAA/CEAS Aeroacoustics Conference and Exhibit*, Breckenridge, Colorado, June 17-19 2002. AIAA paper 2002-2428.

[19] Morfey, C., and Fisher, M. Shock-Wave Radiation from a Supersonic Ducted Rotor. *The Aeronautical Journal of the Royal Aeronautical Society*, 74:579–585, July 1970.

[20] Mathews, D., and Nagel, R. Inlet Geometry and Axial Mach Number Effects on Fan Noise Propagation. In *presented at the Aero-Acoustics Conference*, Seattle, Washington, October 15-19 1973. AIAA paper 1973-1022.

[21] Han, F., Shieh, C., Sharma, A., and Paliath, U. Multiple Pure Tone Noise Prediction and Comparison with Static Engine Test Measurements. In *presented at the 13th AIAA/CEAS Aeroacoustics Conference*, Rome, Italy, May 21-23 2007. AIAA paper 2007-3523.

[22] Prasad, D., and Feng, J. Propagation and Decay of Shock Waves in Turbofan Engine Inlets. *Journal of Turbomachinery*, 127(1):118–127, 2005.

[23] Plas, A., Sargeant, M., Madani, V., Chrichton, D., Greitzer, E., Hynes, T. and Hall, C. Performance of a Boundary Layer Ingesting (BLI) Propulsion System. In *presented at the 45th AIAA Aerospace Sciences Meeting and Exhibit*, Reno, Nevada, January 8-11 2007. AIAA paper 2007-450.

[24] Madani, V. and Hynes, T. Boundary Layer Ingesting Intakes: Design and Optimization. In *presented at the 19th ISABE Conference*, Montreal, Canada, September 13-18 2009. ISABE paper 2009-1346.

[25] Morfey, C. Acoustic Energy in Non-Uniform Flows. *Journal of Sound and Vibration*, 14(2):159–170, 1971.

[26] Guo, Q., Mandal, M., and Li, M. Efficient Hodge-Helmholtz decomposition of motion fields. *Pattern Recognition Letters*, 26:493–501, 2005.

[27] Myers, M. Transport of Energy by Disturbances in Arbitrary Steady Flows. *Journal of Fluid Mechanics*, 226:383–400, 1991.

[28] Brambley, E. and Peake, N. Sound in Curved Intakes. In *presented at the 13th AIAA/CEAS Aeroacoustics Conference*, Rome, Italy, May 21-23 2007. AIAA paper 2007-3552.

[29] Brambley, E. and Peake, N. Sound Transmission in Strongly Curved Slowly Varying Clylindrical Ducts with Flow. *Journal of Fluid*, 596:387–412, 2008.

[30] Lieblein, S. *Experimental Flow in Two-Dimensional Cascades.* Number SP-36. 1965.

[31] Ansys, Inc., Canonsburg, PA. *ANSYS FLUENT User's Guide*, 13.0 edition, November 2010.

[32] Kerner, J. An Assessment of Body Force Representations for Compresssor Stall Simulation. Master's thesis, MIT, Department of Aeronautics and Astronautics, February 2010.

[33] Ffowcs-Williams, J., and Hawkings, D. Sound Generation by Turbulence and Surfaces in Arbitrary Motion. *Proceedings of the Royal Society of London*, 264:321–342, 1969.

[34] Brentner, K., and Farassat, F. An Analytical Comparison of the Acoustic Analogy and Kirchhoff Formulations for Moving Surfaces. *AIAA Journal*, 36(8):1379–1386, 1998.

[35] Huttl, T., Kahl, G., Kennepohl, F., and Heinig, K. Resolution Requirements for the Numerical Computation of Tonal Noise in Compressors and Turbines of Aeroengines. In *presented at the RTO AVT Symposium on 'Ageing Mechanisms and*

Control: Part A - Developments in Computational Aero- and Hydro-Acoustics', Manchester, UK, October 8-11 2001.

[36] Hileman, J., Spakovszky, Z., and Drela, M. Airframe Design for Silent Fuel-Efficient Aircraft. *Journal of Aircraft*, 47(3):956–969, May-June 2010.

[37] Freund, J. Proposed Inflow/Outflow Boundary Condition for Direct Computation of Aerodynamic Sound. *AIAA Journal*, 35(4):740–742, April 1997.

[38] Defoe, J., Narkaj, A., and Spakovszky, Z. A Novel MPT Noise Methodology for Highly-Integrated Propulsion Systems with Inlet Flow Distortion. In *presented at the 15th AIAA/CEAS Aeroacoustics Conference*, Miami, Florida, May 11-13 2009. AIAA paper 2009-3366.

[39] Rumsey, C., Biedron, R., and Farassat, F. Ducted-Fan Engine Acoustic Predictions Usings a Navier-Stokes Code. *Journal of Sound and Vibration*, 213(4):643–664, 1998.

[40] Chen, X., Zhang, X., Morfey, C., and Nelson, P. A Numerical Method for Computation of Sound Radiation from an Unflanged Duct. *Journal of Sound and Vibration*, 270:573–586, 2004.

[41] Zhang, X., Chen, X., Morfey, C., and Nelson, P. Computation of Spinning Modal Radiation from an Unflanged Duct. *AIAA Journal*, 42(9):1795–1801, September 2004.

[42] Sutliff, D. Rotating Rake Turbofan Duct Mode Measurement System. Technical Report NASA/TM-2005-2138328, NASA, 2005.

[43] Ljung, L. *System Identification: Theory for the User.* Prentice-Hall, Inc., Englewood Cliffs, NJ, 1987.

[44] Freeman, C., and Cumpsty, N. A Method for the Prediction of Supersonic Compressor Blade Performance. *Journal of Propulsion and Power*, 8(1):199–208, 1992.

[45] Candel, S. and Poinsot, T. A Tutorial on Acoustics. Laboratoire d'EnergÃ©tique MolÃ©culaire et Macroscopique, Combustion, CNRS, Ecole Central des Art et Manufactures, Chatenay-Malabry, France, 1987.

[46] Heidmann, M. Interim Prediction Method for Fan and Compressor Source Noise. Technical Memorandum X-71763, NASA, June 1975.

[47] Kontos, K., Janardan, A., and Gliebe, P. Improved NASA-ANOPP Noise Prediction Computer Code for Advanced Subsonic Propulsion Systems, Volume 1: ANOPP Evaluation and Fan Noise Mode Improvement. Contractor Report 195480, NASA, August 1996.

[48] Okawa, A. *Vortex Flow.* CRC Press, Inc., Boca Raton, Florida, 1993.

[49] Greitzer, E., Tan, C., and Graf, M. *Internal Flow: Concepts and Applications.* Cambridge University Press, 2004.

[50] Colas, D. A Diffraction Integral Based Turbomachinery Noise Shielding Method. MS Thesis, MIT, Department of Aeronautics and Astronautics, June 2011.

[51] Peters, A. Personal communication, 2011.

Appendix A

The Euler Equations in Blade Rows with Body Forces

This appendix contains a derivation of the specialized form of the Euler equations used within blade rows in Gong [14] and a scaling analysis of the terms in the momentum equations in both the full and specialized versions of the equations. These are included to assist the reader in following the arguments in Section 3.1.3.

A.1 Derivation of the Euler Equations in Blade Rows with Body Forces

For convenience, the derivation of the modified Euler equations in Gong [14] is presented here as a reference for the reader.

The three-dimensional, unsteady, compressible Euler equations for conservation

of mass, momentum, and energy are (in the absolute frame of reference):

$$\frac{\partial}{\partial t}\begin{bmatrix} r\rho \\ r\rho u_x \\ r\rho u_\theta \\ r\rho u_r \\ r\rho e \end{bmatrix} + \frac{\partial}{\partial x}\begin{bmatrix} r\rho u_x \\ r\rho u_x^2 + rp \\ r\rho u_x u_\theta \\ r\rho u_x u_r \\ r u_x (\rho e + p) \end{bmatrix} + \frac{\partial}{\partial \theta}\begin{bmatrix} \rho u_\theta \\ \rho u_x u_\theta \\ \rho u_\theta^2 + p \\ \rho u_\theta u_r \\ u_\theta (\rho e + p) \end{bmatrix}$$
$$+\frac{\partial}{\partial r}\begin{bmatrix} r\rho u_r \\ r\rho u_x u_r \\ r\rho u_\theta u_r \\ r\rho u_r^2 + rp \\ r u_r (\rho e + p) \end{bmatrix} = \begin{bmatrix} 0 \\ r\rho F_x \\ -\rho u_\theta u_r + r\rho F_\theta \\ \rho u_{theta}^2 + p + r\rho F_r \\ r^2 \rho F_\theta \Omega \end{bmatrix} \tag{A.1}$$

where e is the total internal energy.

In a blade row, the assumption is made that there are an infinite number of blades such that the flow in each infinitesimal blade passage is axisymmetric in a reference frame moving with the blade row. Gong states that "due to the presence of the blades, the flow fields between any two blade passages can be different, therefore a three-dimensional flow field in a blade row can be composed of an infinite number of axisymmetric flow fields." [14]

To obtain the governing equations in the blade row subject to this assumption, the following manipulations are performed:

1. Perform a transformation of the reference frame to the blade-row-relative frame
2. Remove all circumferential gradients
3. Transform back to the absolute reference frame

Each of these steps will now be detailed.

The transformation to the relative frame is done using

$$\left.\frac{\partial}{\partial t}\right|_{absolute} = \left.\left(\frac{\partial}{\partial t} - \Omega\frac{\partial}{\partial \theta}\right)\right|_{blade\,row} \tag{A.2}$$

which gives

$$\left(\frac{\partial}{\partial t}-\Omega\frac{\partial}{\partial\theta}\right)\begin{bmatrix} r\rho \\ r\rho u_x \\ r\rho u_\theta \\ r\rho u_r \\ r\rho e \end{bmatrix}+\frac{\partial}{\partial x}\begin{bmatrix} r\rho u_x \\ r\rho u_x^2+rp \\ r\rho u_x u_\theta \\ r\rho u_x u_r \\ ru_x\left(\rho e+p\right) \end{bmatrix}+\frac{\partial}{\partial\theta}\begin{bmatrix} \rho u_\theta \\ \rho u_x u_\theta \\ \rho u_\theta^2+p \\ \rho u_\theta u_r \\ u_\theta\left(\rho e+p\right) \end{bmatrix}$$
$$+\frac{\partial}{\partial r}\begin{bmatrix} r\rho u_r \\ r\rho u_x u_r \\ r\rho u_\theta u_r \\ r\rho u_r^2+rp \\ ru_r\left(\rho e+p\right) \end{bmatrix}=\begin{bmatrix} 0 \\ r\rho F_x \\ -\rho u_\theta u_r+r\rho F_\theta \\ \rho u_{theta}^2+p+r\rho F_r \\ r^2\rho F_\theta\Omega \end{bmatrix} \quad \text{(A.3)}$$

The flow is assumed to be axisymmetric in this frame of reference. As a result, all circumferential gradients are dropped:

$$\left(\frac{\partial}{\partial t}\right)\begin{bmatrix} r\rho \\ r\rho u_x \\ r\rho u_\theta \\ r\rho u_r \\ r\rho e \end{bmatrix}+\frac{\partial}{\partial x}\begin{bmatrix} r\rho u_x \\ r\rho u_x^2+rp \\ r\rho u_x u_\theta \\ r\rho u_x u_r \\ ru_x\left(\rho e+p\right) \end{bmatrix}+\frac{\partial}{\partial r}\begin{bmatrix} r\rho u_r \\ r\rho u_x u_r \\ r\rho u_\theta u_r \\ r\rho u_r^2+rp \\ ru_r\left(\rho e+p\right) \end{bmatrix}=\begin{bmatrix} 0 \\ r\rho F_x \\ -\rho u_\theta u_r+r\rho F_\theta \\ \rho u_{theta}^2+p+r\rho F_r \\ r^2\rho F_\theta\Omega \end{bmatrix} \quad \text{(A.4)}$$

Upon transformation back to the absolute frame, the final form of the modified Euler

equations is obtained:

$$\left(\frac{\partial}{\partial t}+\Omega\frac{\partial}{\partial\theta}\right)\begin{bmatrix} r\rho \\ r\rho u_x \\ r\rho u_\theta \\ r\rho u_r \\ r\rho e \end{bmatrix} + \frac{\partial}{\partial x}\begin{bmatrix} r\rho u_x \\ r\rho u_x^2 + rp \\ r\rho u_x u_\theta \\ r\rho u_x u_r \\ r u_x\left(\rho e + p\right) \end{bmatrix}$$
$$+\frac{\partial}{\partial r}\begin{bmatrix} r\rho u_r \\ r\rho u_x u_r \\ r\rho u_\theta u_r \\ r\rho u_r^2 + rp \\ r u_r\left(\rho e + p\right) \end{bmatrix} = \begin{bmatrix} 0 \\ r\rho F_x \\ -\rho u_\theta u_r + r\rho F_\theta \\ \rho u_{theta}^2 + p + r\rho F_r \\ r^2\rho F_\theta \Omega \end{bmatrix} \tag{A.5}$$

A.2 Scaling Analysis

To understand how terms scale differently in the full and modified Euler equations, a scaling analysis is performed. The equation selected for the comparison is the axial momentum equation. Below each equation, the scaling of terms is presented. The quantities U, C, ω, R, and λ are representative velocity, length, and angular frequency scales.

Axial momentum in the ordinary Euler equations yields

$$\begin{array}{lccccc} \dfrac{\partial u_x}{\partial t} + u_x\dfrac{\partial u_x}{\partial x} + \dfrac{u_\theta}{r}\dfrac{\partial u_x}{\partial\theta} & = & -\dfrac{1}{\rho}\dfrac{\partial p}{\partial x} + \dfrac{F_x}{\rho} \\ U_x\omega \quad \dfrac{U_x^2}{C} \quad \dfrac{U_x^2}{C} & & \dfrac{U_x^2}{C} \quad \dfrac{F_x C}{\rho U_x^2} \end{array} \tag{A.6}$$

while for the modified axial momentum Euler equation, we have

$$\begin{array}{lccccc} \dfrac{\partial u_x}{\partial t} + u_x\dfrac{\partial u_x}{\partial x} + \Omega\dfrac{\partial u_x}{\partial\theta} & = & -\dfrac{1}{\rho}\dfrac{\partial p}{\partial x} + \dfrac{F_x}{\rho} \\ U_x\omega \quad \dfrac{U_x^2}{C} \quad \dfrac{2\pi\Omega U_x R}{\lambda} & & \dfrac{U_x^2}{C} \quad \dfrac{F_x C}{\rho U_x^2} \end{array} \tag{A.7}$$

The terms containing circumferential gradients scale differently; taking the ratio of the scaling rules gives the reduced frequency:

$$\beta = \frac{2\pi\Omega RC}{\lambda U_x} \tag{A.8}$$

The interpretation is that if the reduced frequency is of order unity, then the two terms have similar magnitudes and there is no qualitative change in behavior between the two versions of the Euler equations.